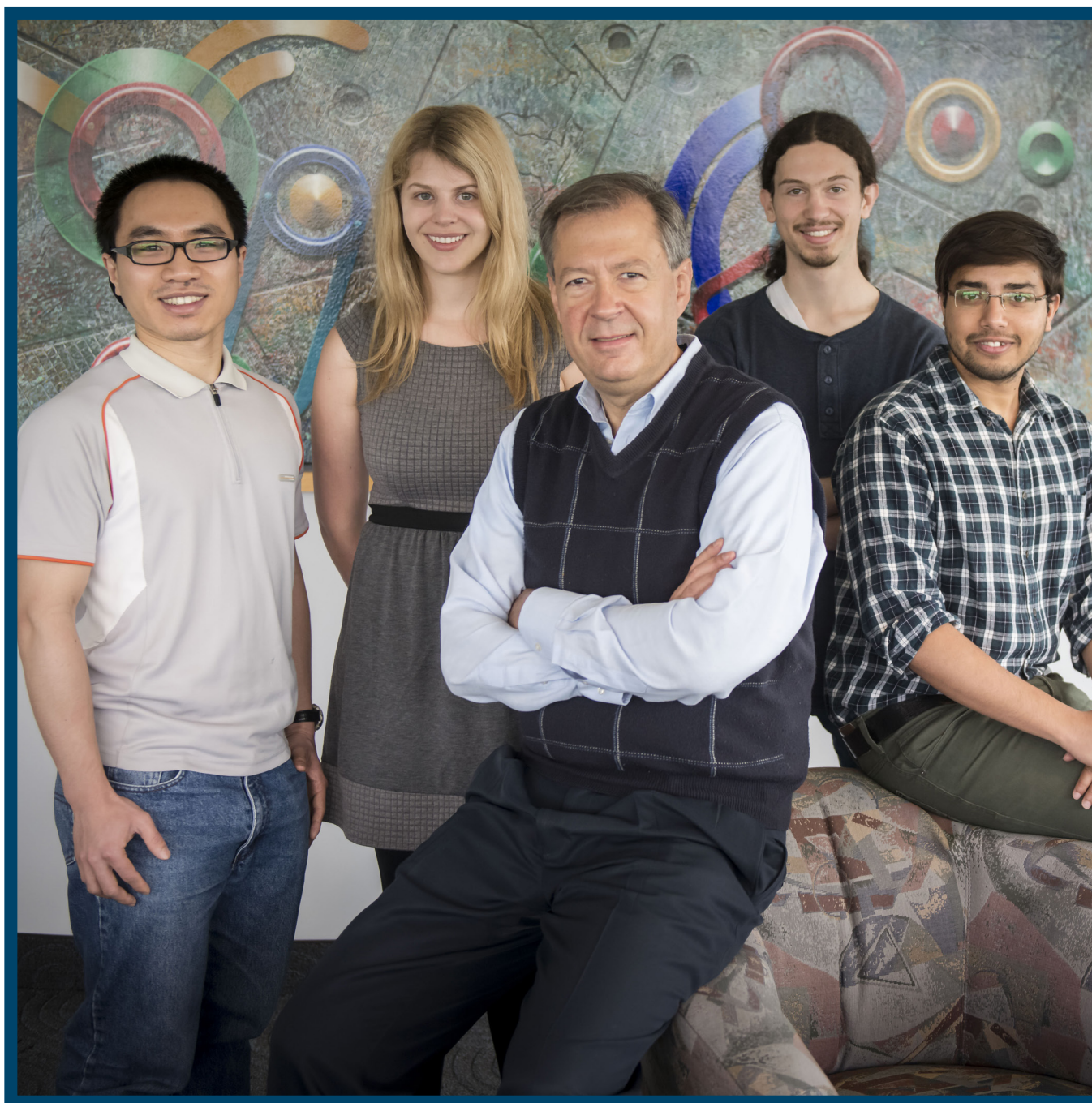


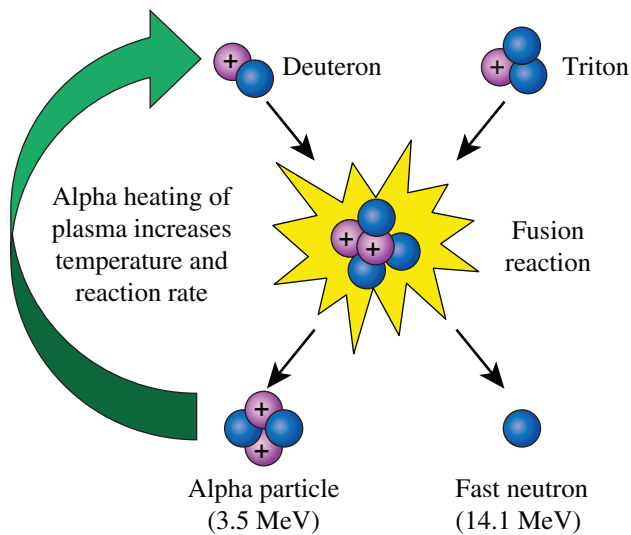
# LLE Review

## Quarterly Report



## About the Cover:

The photo on the cover shows Prof. Riccardo Betti (front) with University of Rochester students Jack Woo, Alison Christopherson, Joel Howard, and Arijit Bose (left to right). The University of Rochester team, together with collaborators at Lawrence Livermore National Laboratory and the University of Madrid, have developed a technique to measure the level of alpha-particle heating and to assess the onset of the burning-plasma regime in inertial fusion implosion experiments. Fusion alphas are produced in the fusion reactions of the thermonuclear fuel deuterium and tritium (DT) with an energy of 3.5 MeV and slow down through collisions with plasma electrons. The alpha-heated electrons transfer part of their energy to the D and T ions, thereby increasing the fusion reaction rate. The burning-plasma state is achieved when the alpha heating exceeds the external input energy to the thermonuclear fuel. Assessing the degree to which fusion alpha particles contribute to the plasma heating is essential to understanding the onset of the thermal runaway process called “ignition.” Thermonuclear ignition is the most fundamental process at the heart of controlled nuclear fusion.



E24206JR

This report was prepared as an account of work conducted by the Laboratory for Laser Energetics and sponsored by New York State Energy Research and Development Authority, the University of Rochester, the U.S. Department of Energy, and other agencies. Neither the above-named sponsors nor any of their employees makes any warranty, expressed or implied, or assumes any legal liability or responsibility for the accuracy, completeness, or usefulness of any information, apparatus, product, or process disclosed, or represents that its use would not infringe privately owned rights. Reference herein to any specific commercial product, process, or service by trade name, mark, manufacturer, or otherwise, does not necessarily constitute or imply its endorsement, recommendation, or favoring

Printed in the United States of America

Available from

National Technical Information Services  
U.S. Department of Commerce  
5285 Port Royal Road  
Springfield, VA 22161  
[www.ntis.gov](http://www.ntis.gov)

The image at the left shows a diagram of the thermal feedback process called alpha heating. If a thermonuclear plasma with deuterium (D) and tritium (T) is sufficiently hot and dense, then the D and T fuse to create one alpha particle and one neutron. The fast neutron escapes while the alpha particle deposits its energy back into the plasma, heating it more. As the reaction rate increases, the alpha-heating rate increases, which in turn increases the reaction rate. This thermal instability is the mechanism leading to high-energy gains in thermonuclear fusion schemes.

by the United States Government or any agency thereof or any other sponsor. Results reported in the LLE Review should not be taken as necessarily final results as they represent active research. The views and opinions of authors expressed herein do not necessarily state or reflect those of any of the above sponsoring entities.

The work described in this volume includes current research at the Laboratory for Laser Energetics, which is supported by New York State Energy Research and Development Authority, the University of Rochester, the U.S. Department of Energy Office of Inertial Confinement Fusion under Cooperative Agreement No. DE-NA0001944, and other agencies.

For questions or comments, contact Dustin Froula, Editor, Laboratory for Laser Energetics, 250 East River Road, Rochester, NY 14623-1299, (585) 273-3686.

Worldwide-Web Home Page: <http://www.lle.rochester.edu/>  
(Color online)

# LLE Review

## Quarterly Report



### Contents

In Brief .....	iii
Alpha Heating and Burning Plasmas in Inertial Confinement Fusion .....	77
Measurements of the Ablation-Front Trajectory and Low-Mode Nonuniformity in Direct-Drive Implosions Using X-Ray Self-Emission Shadowgraphy .....	83
Nanomechanical Properties of Single-Layer Optical Oxide Thin Films Used for High- Laser-Damage-Threshold Applications .....	91
Thermal Fluctuations in Superconductor/ Ferromagnet Nanostripes .....	97
Spectral Changes Induced by a Phase Modulator Acting as a Time Lens .....	104
Surface-Texture Evolution of Different Chemical-Vapor-Deposited Zinc Sulfide Flats Polished with Various Magnetorheological Fluids .....	110
Publications and Conference Presentations	



## In Brief

This volume of the LLE Review, covering January–March 2015, features “Alpha Heating and Burning Plasmas in Inertial Confinement Fusion” by R. Betti, A. R. Christopherson, A. Bose, J. Howard, and K. M. Woo (LLE and the Fusion Science Center); B. K. Spears, R. Nora, and M. J. Edwards (LLNL); and J. Sanz (Universidad Politécnica de Madrid). This article (p. 77) estimates the level of alpha heating and determines the onset of the burning-plasma regime, which are essential to finding the path toward thermonuclear ignition. Using a simple model of the implosion, it is shown that a general relation can be derived connecting the burning-plasma regime to the yield enhancement caused by alpha heating and experimentally measurable parameters such as the fractional alpha energy or, equivalently, the Lawson ignition parameter. A general alpha-heating curve is found, independent of the target and suitable to assess the performance of all laser-fusion experiments whether direct or indirect drive. The onset of the burning-plasma regime inside the hot spot of current implosions at the National Ignition Facility requires a fusion yield of  $\sim 50$  kJ.

Additional research highlights presented in this issue include the following:

- D. T. Michel, A. K. Davis, W. R. Armstrong, R. E. Bahr, R. Epstein, V. N. Goncharov, M. Hohenberger, I. V. Igumenshchev, R. Q. Jungquist, D. D. Meyerhofer, P. B. Radha, T. C. Sangster, C. Sorce, and D. H. Froula (LLE) present measurements of the ablation-front trajectory and low-mode nonuniformity in direct-drive implosions using x-ray self-emission shadowgraphy (p. 83). The shadowgraphy technique uses time-resolved images of soft x rays ( $>1$  keV) emitted from the coronal plasma of the target imaged onto an x-ray framing camera to determine the position of the ablation front. Methods used to accurately measure the ablation-front radius ( $\delta R = \pm 1.15 \mu\text{m}$ ), image-to-image timing [ $\delta(\Delta t) = \pm 2.5$  ps], and absolute timing ( $\delta t = \pm 10$  ps) are presented. Angularly averaging the images provides an average radius measurement of  $\delta(R_{\text{av}}) = \pm 0.15 \mu\text{m}$  and an error in velocity of  $\delta V/V = \pm 3\%$ . This technique was applied at the Omega Laser Facility and the National Ignition Facility.
- K. Mehrotra and J. C. Lambropoulos (LLE and Dept. of Mechanical Engineering) and J. B. Oliver (LLE) present the mechanical characterization of optical oxide thin films that is performed using nano-indentation (p. 91). The results are explained based on the deposition conditions used. These oxide films are generally deposited to have a porous microstructure that optimizes laser-induced damage thresholds, but changes in deposition conditions lead to varying degrees of porosity, density, and possibly the microstructure of the thin film. This can directly explain the difference in the mechanical properties of the film studied here and those reported in literature. Of the four single-layer thin films tested, alumina was observed to demonstrate the highest values of nano-indentation hardness and elastic modulus.
- U. Nasti (Università degli Studi di Napoli Federico II); L. Parlato and G. Pepe (Università degli Studi di Napoli Federico II and CNR-SPIN Institute of Superconductors); M. Ejrnaes and R. Cristiano (CNR-SPIN Institute of Superconductors); T. Taino and H. Myoren (Saitama University); and R. Sobolewski (LLE and Depts. of Electrical and Computer Engineering and Physics and Astronomy, University

of Rochester) investigate the thermal fluctuations in hybrid superconductor/ferromagnetic NbN/NiCu bilayers, as well as in pure superconducting NbN 2-D nanostripes to understand the origin of dark counts in superconducting nanostripes when operated as single-photon detectors (p. 97). In 2-D superconductors, the dynamics of vortex motion plays a significant role in the formation of a transient normal state, leading to dark-count events in current-biased nanostripes. By introducing a weak ferromagnetic overlayer on top of pure NbN, the vortex dynamics were controlled, which subsequently made it possible to discriminate between several proposed theoretical models.

- B. W. Plansinis and G. P. Agrawal (LLE and Institute of Optics) and W. R. Donaldson (LLE) show both numerically and experimentally that a phase modulator, acting as a time lens in the Fourier-lens configuration, can induce spectral broadening, narrowing, or shifts depending on the phase of the modulator cycle (p. 104). These spectral effects depend on the maximum phase shift that can be imposed by the modulator. Numerical simulations show that the pulse spectrum could be compressed by a factor of 8 for a 30-rad phase shift. Experimentally, spectral shifts over a 1.35-nm range and spectral narrowing and broadening by a factor of 2 were demonstrated using a lithium niobate phase modulator with a maximum phase shift of 16 rad at a 10-GHz modulation frequency. All spectral changes were accomplished without employing optical nonlinear effects such as self- or cross-phase modulation.
- S. Salzman (LLE and Materials Science Program); H. J. Romanofsky (LLE); S. D. Jacobs (LLE, Materials Science Program, Institute of Optics, and Dept. of Chemical Engineering, University of Rochester); and J. C. Lambropoulos (LLE, Materials Science Program, Institute of Optics, and Dept. of Mechanical Engineering, University of Rochester) show that the macrostructure of chemical-vapor-deposited (CVD) zinc sulfide (ZnS) substrates is characterized by cone-like structures that start growing at the early stages of deposition (p. 110). As deposition progresses, these cones grow larger and reach centimeter size in height and millimeter size in width. This article describes the magnetorheological finishing (MRF) process of polishing four CVD ZnS substrates, manufactured by four different vendors, with conventional magnetorheological (MR) fluid at pH 10 and zirconia-coated-CI (carbonyl iron) MR fluids at pH 4, 5, and 6. The surface-texture evolution of the substrates as they were MRF polished with the different fluids is reported. The performances of the zirconia-coated-CI MR fluid at pH 4 are shown to be significantly higher than that of the same fluid at pH levels of 5 and 6 and moderately higher than that of a conventional MR fluid at pH 10.

Dustin H. Froula  
*Editor*

---

## Alpha Heating and Burning Plasmas in Inertial Confinement Fusion

In inertial confinement fusion<sup>1</sup> (ICF), a shell of cryogenic deuterium (D) and tritium (T) ice is imploded at high velocities (300 to 400 km/s) and low entropy to achieve high central temperatures and high areal densities.<sup>2</sup> The final fuel assembly consists of a relatively low-density (30- to 100-g/cm<sup>3</sup>), high-temperature (5- to 10-keV) core—the hot spot—surrounded by a dense (300- to 1000-g/cm<sup>3</sup>), cold (200- to 500-eV) fuel layer—the compressed shell. Alpha particles are produced from the D + T fusion reactions with an energy  $\varepsilon_\alpha = 3.5$  MeV and slow down primarily through collisions with the plasma electrons. The alpha-heated electrons transfer part of their energy to the D and T ions, thereby increasing the fusion-reaction rate. The process of depositing alpha energy inside the hot spot of a compressed ICF capsule is called *alpha heating*. Ignition is a direct consequence of both alpha heating and its feedback on the thermal energy and fusion-reaction rate. When this feedback process becomes unstable, it leads to a thermal runaway within the central hot spot.<sup>2</sup> A robustly ignited hot spot drives a burn wave in the surrounding dense shell, leading to fusion energy outputs in a megajoule range that greatly exceeds the thermal and kinetic energy supplied to the DT fuel by the implosion alone (~tens of kilojoules).

Recent experiments at the National Ignition Facility (NIF) (high-foot targets<sup>3</sup>) have demonstrated significant alpha heating using indirect drive (ID). To make progress toward ignition on the NIF,<sup>4</sup> it is crucial to be able to measure the level of alpha heating and to identify intermediate plasma states where the alpha heating is the leading source of input energy (alpha-dominated or burning plasmas). In magnetic confinement fusion (MCF),<sup>5</sup> the burning-plasma regime is identified through the thermonuclear  $Q = \text{fusion power output} / \text{external power input}$ . Since the alpha energy is about 1/5 of the total fusion energy, a  $Q = 5$  denotes the state where the alpha power equals the input power. For convenience, in this article we use  $Q_\alpha = \text{alpha power} / \text{input power} = Q/5$  and define the onset of a burning plasma at  $Q_\alpha = 1$  ( $Q = 5$ ).

While determining  $Q_\alpha$  for a steady-state MCF device is straightforward, the definition for ICF is greatly complicated

by the transient nature of an ICF implosion and by the fact that the vast majority of the input energy does not reach the DT plasma. Since this article is concerned only with the physics of burning plasmas and not with the prospects for fusion energy, the relevant input energy is the one reaching the DT plasma, where the fusion reactions occur. Therefore, the parameters  $Q$ ,  $Q_\alpha$  used here refer to the DT fuel and should not be confused with the engineering  $Q$  used for fusion reactors.<sup>5</sup>

Heating by the fusion alphas enhances the fusion yield to varying degrees, depending on the fraction of deposited alpha-particle energy to the total hot-spot energy. Here we consider yield amplifications  $\leq 10$ , which are of most interest for current implosions on the NIF and characteristic of a sub-ignited burning plasma. Using a simple model of the hot spot and shell dynamics (*alpha-heating model*), we find the burning-plasma conditions for ICF and show that the fusion-yield enhancement resulting from alpha heating depends only on the fractional alpha energy or the Lawson parameter<sup>6,7</sup> through a universal curve valid for direct- and indirect-drive ICF. It is shown that the alpha-heating model results are in good agreement with those from radiation-hydrodynamics simulations.

The alpha-heating model describes both the hot-spot formation and the piston action of the shell providing the external input energy. To correctly capture the  $PdV$  work to the hot spot and to the shell, the incompressible shell model<sup>7</sup> is not suitable; instead a compressible model similar to the one in Ref. 8 is used. In the final stage of the implosion, the shell is described as a compressible gas separated into two regions (shocked and free fall) by the return shock driven by the hot-spot pressure into the shell. The temporal evolution of the hydrodynamic quantities is determined from the beginning of the shell's deceleration phase up to the shell's rebound, and both the heat conduction and radiation losses are included. A fraction of the alpha particles escapes through the hot-spot boundary, depositing their energy into the cold shell and ablating shell mass into the hot spot. It is assumed that all of the radiation escapes from the hot spot, reducing the pressure and temperature. The fusion rate is approximated with  $\langle \sigma v \rangle \approx c_\alpha T^3$  ( $c_\alpha =$

const), which is sufficiently accurate in the interesting 4- to 8-keV range characteristic of a yield amplification  $\leq 10$ . The conservation equations for mass, momentum, and energy can be written in the dimensionless form:

$$\left(\hat{P}\hat{R}_h^3/\hat{T}\right)' = \hat{R}_h\hat{T}^{5/2} + 3/5(1-\theta_\alpha)\gamma\hat{P}^2\hat{R}_h^3, \quad (1)$$

$$\left(\hat{M}_{ss}\hat{U}_{ss}\right)' - \hat{M}_{ss}\hat{U}_{ff}(\hat{R}_k) = \hat{P}\hat{R}_h^2 + 2\int_{\hat{R}_h}^{\hat{R}_k}\hat{r}\hat{P}_{ss}d\hat{r}, \quad (2)$$

$$\hat{M}_{ss} = \hat{R}_k^2\hat{\rho}_{ff}(\hat{R}_k - \hat{U}_{ff}), \quad (3)$$

$$\hat{R}_k = 4/3\hat{U}_{ss}(\hat{R}_k) - 1/3\hat{U}_{ff}(\hat{R}_k), \quad (4)$$

$$\left(\hat{P}\hat{R}_h^5\right)' = \hat{P}^2\hat{R}_h^5(\gamma\hat{T} - \beta\hat{T}^{-3/2}). \quad (5)$$

Equation (1) is the hot-spot mass conservation used to infer the hot-spot temperature  $T$  with the right-hand side representing the mass ablation off the inner shell surface driven by the heat conduction<sup>7</sup> and alpha-particle losses.<sup>9</sup> Here  $\hat{R}_h$  represents the hot-spot radius. Equation (2) represents Newton's law for the shocked portion of the shell slowed down by the hot-spot pressure  $P$ . The return shock  $R_k$  separates the free-fall (ff) and the shocked (ss) regions of the shell. The shocked-shell pressure  $P_{ss}$  approximately varies linearly from the hot-spot pressure to the post-shock pressure given by the Rankine–Hugoniot (RH) relations. Equation (3) governs the shocked-shell mass and includes the flow of mass across the return shock. Equation (4) describes the evolution of the return-shock position  $R_k$  through the RH relations. The velocity within the shocked shell is determined through a Taylor expansion about the hot-spot radius using the isentropic relation of the shocked shell, leading to

$$\hat{U}_{ss}(\hat{r}) \approx \hat{R}_h + \left[\hat{R}_h/\hat{R}_h - (3/5)\hat{\phi}/\hat{\phi}\right](\hat{r} - \hat{R}_h), \quad (6)$$

where  $\hat{\phi} \equiv \hat{P}\hat{R}_h^5$ . Equation (5) is the hot-spot energy conservation where the two terms on the right-hand side represent the alpha-heating contribution and the radiation losses. The level of alpha heating and radiation losses are determined by the parameters  $\gamma$  and  $\beta$ , respectively. Some three-dimensional (3-D) effects resulting from the reduction of the hot-spot volume<sup>10</sup> from the deceleration-phase Rayleigh–Taylor spikes can be included through a clean volume analysis, as described in Ref. 7, but are omitted for simplicity in this article. Pressure, radius, and temperature are normalized with their stagnation

values  $T_s$ ,  $P_s$ , and  $R_s$  in the absence of alpha heating and radiation losses and for an incompressible shell with equal mass:

$$M_{sh}V_{imp}^2 = 4\pi P_s R_s^3, \quad (7)$$

$$\kappa_0 T_s^{7/2} = P_s R_s V_{imp}, \quad (8)$$

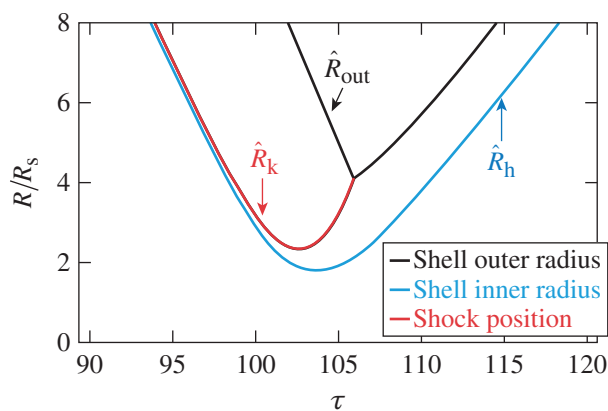
where  $V_{imp}$  is the implosion velocity,  $M_{sh}$  is the shell mass, and  $\kappa_0$  is the Spitzer thermal conductivity coefficient<sup>11</sup> in  $\kappa_{Sp} = \kappa_0 T^{5/2}$ . The dimensionless time is  $\tau = tV_{imp}/R_s$ . The dimensionless velocity is normalized with the peak implosion velocity  $V_{imp}$ . For simplicity we assume an initially uniform velocity profile so that  $\hat{U}_{ff} = -1$ . The dimensionless shocked-shell mass is defined as  $\hat{M}_{ss} = M_{ss}/M_{sh}$ . The dimensionless shell density is defined as  $\hat{\rho} = \rho/(M_{sh}/4\pi R_s^3)$  and its profile during the coasting phase (or free fall) is assumed to be approximately parabolic. The constant  $\gamma = c_\alpha \epsilon_\alpha P_s T_s R_s / (24 V_{imp})$  determines the level of alpha heating. The parameter  $\beta = c_b P_s R_s / (6T_s^{3/2} V_{imp})$  determines the radiation losses ( $c_b$  is the bremsstrahlung constant for the radiated power density  $\dot{P}_{rad} \approx c_b n^2 \sqrt{T}$ ). The fraction of escaping alphas is determined by analyzing Ref. 12:

$$\theta_\alpha(\xi_\alpha > 1/2) = 1 - 1/(4\xi_\alpha) + 1/(160\xi_\alpha^3), \quad (9)$$

$$\theta_\alpha(\xi_\alpha < 1/2) = 3/2\xi_\alpha - 4/5\xi_\alpha^2, \quad (10)$$

where  $\xi_\alpha = \xi_0 \hat{P}\hat{R}_h/\hat{T}^{5/2}$ . We use  $\xi_0 = 0.6$ , leading to a fraction of absorbed alphas at a bang time of about 0.7 to 0.8 in agreement with numerical simulations including alpha-transport physics. Equations (1)–(5) are solved from the beginning of the deceleration phase ( $t = 0$ ) with a radius much greater than the stagnation radius  $\hat{R}_h(0) = \hat{R}_0 \gg 1$ , a velocity equal to the implosion velocity  $\hat{R}_h'(0) = -1$ , and a very low initial pressure and temperature  $\hat{P}(0) = \hat{R}(0)^{-5/2}$ ,  $\hat{T}(0) = \hat{R}(0)^{-1/2}$ , respectively. At  $t = 0$ , the return shock is approaching the imploding shell [ $\hat{R}_k(0) = \hat{R}_0$ ] and the shocked-shell mass is zero [ $\hat{M}_{ss}(0) = 0$ ]. The initial aspect ratio is set to  $A_0 \approx 0.1\hat{R}_h(0)$ , leading to a stagnating mass of about 50% of the DT unablated mass as indicated by the hydrodynamic simulations of ignition targets.<sup>7</sup> Figure 142.1 shows the trajectories of the inner shell surface (or hot-spot radius), return shock, and outer shell surfaces. After the return shock reaches the outer surface, the entire shell mass is shocked and the shell behaves like a rigid piston.

The solution of Eqs. (1)–(5) exhibits a singularity (ignition) for a critical value of  $\gamma$  that depends on  $\beta$ . A numerical



TC12070JR

Figure 142.1

Trajectories from the model [Eqs. (1)–(5)] using  $\beta = 0$ ,  $\gamma = 0$ . The figure shows the time evolution of the hot-spot radius, the return shock inside the shell, and the shell's outer surface.

solution leads to the critical  $\gamma(\beta) \approx 28 + 4.3\beta + 2\beta^2$  for  $\beta \leq 2$ . The ignition parameter can be written as  $\chi_{no\alpha} = \gamma/\gamma(\beta)$  with  $\chi_{no\alpha} = 1$  being the ignition condition. From full hydrodynamic simulations with radiation on/off, we determine that radiation losses cause a reduction of  $\sim 15\%$  to  $20\%$  in hot-spot pressure and temperature, corresponding to a value of  $\beta \approx 1.5$  in the model [Eqs. (1)–(5)]. The subscript “no  $\alpha$ ” indicates that all the hydrodynamic quantities are evaluated without alpha-particle energy deposition ( $\gamma = 0$ ). Using Eqs. (7) and (8), both  $\gamma$  and  $\beta$  can be rewritten in terms of the shell's areal density and hot-spot temperature without alpha deposition. In one dimension (1-D), since both  $\gamma$  and  $\beta$  depend on areal density and temperature, the ignition parameter  $\chi_{no\alpha}$  also depends on areal density and temperature. Note that with respect to the incompressible thin-shell model of Ref. 7, the scaling of the ignition parameter is unchanged. A convenient form of  $\chi$  is written in terms of areal density and neutron yield:

$$\chi_{no\alpha} \simeq (\rho R_{no\alpha})^{0.61} \left( \frac{0.24 Y_{no\alpha}^{16}}{M_{DT}^{unab}} \right)^{0.34}, \quad (11)$$

where  $\rho R$  is in  $\text{g}/\text{cm}^2$ , yield is in  $10^{16}$ , and the unablated DT mass is in mg. Another form of  $\chi_{no\alpha}$  is given in Ref. 7:

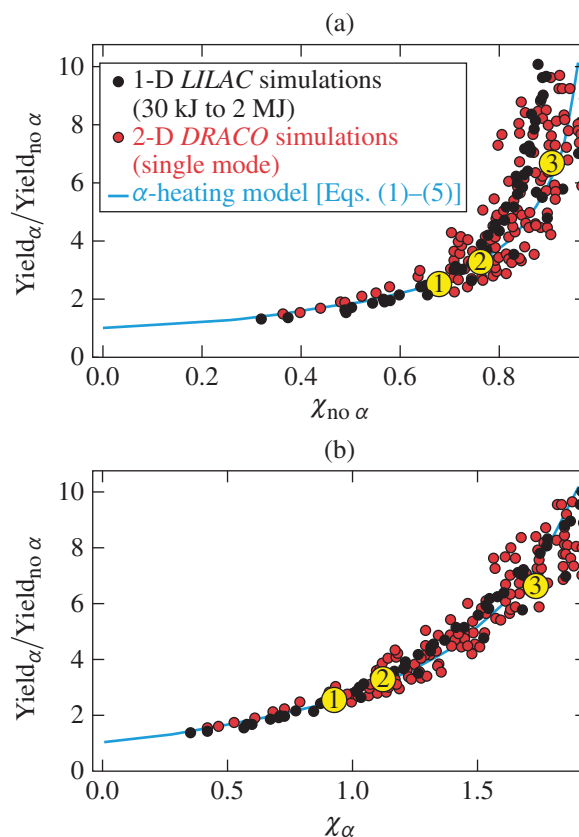
$$\chi_{no\alpha} \simeq (\rho R_{no\alpha})^{0.8} (T_{no\alpha}/4.7)^{1.6} \text{YOC}_{no\alpha}^{0.4}, \quad (12)$$

where the temperature is in keV and the yield over clean (YOC)  $\equiv \text{yield}(3\text{-D})/\text{yield}(1\text{-D})$  is a measure of the level of nonuniformities in the implosion. The model [Eqs. (1)–(5)] is 1-D but the same clean-volume analysis of Ref. 7 can be applied to capture 3-D effects by redefining  $\chi$  as in Eq. (12), using the YOC, or

by using the measured yield in Eq. (11). Note that Eq. (11) can be derived from Eq. (12) by using the approximate formula for the 1-D yield  $Y_{16}(1\text{-D}) = \rho R^{0.56} (T/4.7)^{4.7} M_{DT}/0.24$  (Ref. 7) into the YOC. The yield amplification caused by alpha heating is computed by solving Eqs. (1)–(5) with  $\gamma = 0$  (no alphas) and with a finite  $\gamma < \gamma(\beta)$  (i.e.,  $\chi_{no\alpha} < 1$ ). The ratio of the resulting fusion yields,

$$Y = \int_0^\infty \hat{P}^2 \hat{T} \hat{R}_h^3 d\tau,$$

represents the yield amplification. Figure 142.2(a) compares the yield amplification as a function of the ignition parameter obtained from hydrodynamic simulations with the curve from the alpha-heating model. The simulations were performed with the hydrocodes *LILAC* (1-D)<sup>13</sup> and *DRACO* (2-D).<sup>14</sup> The results can be approximated with the fitting formula



TC12071JR

Figure 142.2

Yield enhancement from alpha heating as a function of the alpha and no-alpha Lawson parameters using the model [Eqs. (1)–(5)] (solid curve) and hydrodynamic simulations (circles). The measurable parameter  $\chi_\alpha$  can be used to determine the yield amplification from (b). From this, (a) can be used to infer the no-alpha parameter  $\chi_{no\alpha}$ , which is useful to assess progress toward ignition. Points 1–3 represent simulations with mass and velocity similar to NIF indirect-drive (ID) targets (see Fig. 142.4).

$\hat{Y}_{\text{amp}} \approx (1 - \chi_{\text{no}\alpha}/0.96)^{-0.75}$ . As stated in Ref. 7, the  $\chi$ 's from Eqs. (11) and (12) are valid in 3-D for relatively fast targets with  $V_{\text{imp}} \sim 300$  to 400 km/s. Note that for a mass of DT of 0.18 mg,  $\chi_{\text{no}\alpha}^{2.9}$  is approximately equal to the experimental ignition threshold factor parameter<sup>15</sup> (ITFx) for the Livermore indirect-drive-ignition target,<sup>16</sup> indicating that the validity of Eq. (11) as an ignition parameter is also confirmed by a large database of indirect-drive ignition-target simulations. In experiments with significant alpha heating, the no- $\alpha$  quantities entering in the definition of  $\chi_{\text{no}\alpha}$  cannot be directly measured. The measured yield and areal density can still be used, however, in Eq. (11) to determine a value of  $\chi$  with alphas ( $\chi_{\alpha}$ ):

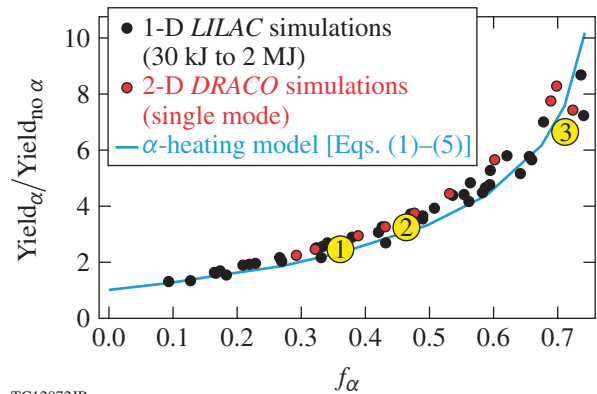
$$\chi_{\alpha} \approx (\rho R_{\alpha})^{0.61} \left( \frac{0.24 Y_{\alpha}^{16}}{M_{\text{DT}}^{\text{unab}}} \right)^{0.34}. \quad (13)$$

From Eqs. (1)–(5), a yield amplification curve using the measurable parameter  $\chi_{\alpha}$  has been generated [Fig. 142.2(b)]. The yield amplification is approximately a unique function of  $\chi_{\alpha}$ , indicating that inferring  $\chi_{\alpha}$  from the experimental observables ( $\rho R$  and yield) is sufficient to determine the yield amplification caused by alpha heating in an experiment. Figure 142.2(b) compares the yield amplification versus  $\chi_{\alpha}$  from simulations with the alpha-heating model [Eqs. (1)–(5)]. The model result can be approximated for amplifications  $\leq 10$  with the simple formula  $\hat{Y}_{\text{amp}} \approx \exp(\chi_{\alpha}^{1.2})$ . When compared to the results of Spears and Lindl<sup>17</sup> for the NIF indirect-drive-ignition target ( $M_{\text{DT}} \approx 0.18$  mg), the yield-amplification curves are in good agreement with the data points from the simulation database of that specific target. In Ref. 17, the Lawson parameter is computed from  $P\tau/(P\tau)_{\text{ign}}$  (related to  $\chi$  as in Ref. 7) with alpha deposition. In this article, the analysis is carried out in dimensionless form, and the results are applicable to all targets, large or small, direct drive or indirect drive, as long as the ignition parameter  $\chi_{\alpha}$  is calculated using Eq. (13). For the high-foot shot N140120 (Ref. 18), which achieved a yield of  $\sim 9.3 \times 10^{15}$  neutrons, an areal density of  $\approx 0.78$  g/cm<sup>2</sup>, and an ion temperature of 4.9 keV, with  $M_{\text{DT}} \approx 0.18$  mg, we find that  $\chi_{\alpha} \approx 0.92$  and the yield amplification is  $\sim 2.5$  (point 1 in Fig. 142.2), close to the simulation result.<sup>18</sup> The corresponding  $\chi_{\text{no}\alpha} \approx 0.66$  is inferred from Fig. 142.2.

A more-indicative measurable parameter for alpha heating is the fractional alpha energy ( $f_{\alpha}$ ) given by the ratio of the alpha energy deposited inside the hot spot up to bang time (peak of the neutron rate) and the neutron-averaged hot-spot energy

$$f_{\alpha} \equiv \frac{(1/2)\theta_{\alpha}E_{\alpha}}{(3/2)\langle P \rangle V_{\text{hs}}}. \quad (14)$$

This parameter is a direct measure of the importance of alpha heating to the hot-spot energy. The fractional alpha energy can be inferred directly from experimental observables, including hot-spot radius, ion temperature, neutron yield, and burnwidth. The alpha energy directly deposited up to bang time is about 1/2 of the total alpha energy times the absorbed fraction  $\theta_{\alpha}$ . The latter can be inferred using Eqs. (9) and (10) and  $\xi_{\alpha}$  from Ref. 12 (where  $\xi_{\alpha}$  is denoted with  $\tau$ ). The hot-spot energy can be inferred from its pressure  $\langle P \rangle$  and volume  $V_{\text{hs}}$  using the method in Ref. 19. Once the pressure is determined, the hot-spot density follows from the equation of state ( $\rho \sim P/T$ ); therefore, the absorbed alpha fraction is inferred from Ref. 12 using the hot-spot areal density and temperature. From the model [Eqs. (1)–(5)], one can reproduce the same quantities used in experiments to infer  $f_{\alpha}$ . Figure 142.3 shows the yield amplification from Eqs. (1)–(5) versus  $f_{\alpha}$  and compares it to the results of simulations using the same procedure to determine  $f_{\alpha}$  (as in an experiment). The two-dimensional (2-D) simulation results (red circles) require a lengthy post-processing analysis with the code *Spect3D*<sup>20</sup> to determine the x-ray-emitting volume measured in experiments.<sup>19</sup> Only a subset of the 2-D simulations in Fig. 142.2 has been post-processed. Figure 142.3 shows that the yield amplification is approximately a unique function of  $f_{\alpha}$ , which can also be used to infer the level of alpha heating. The yield amplification in Fig. 142.3 can be approximated by the simple formula  $\hat{Y}_{\text{amp}} \approx \exp[(f_{\alpha}/0.4)^{1.1}]$ . For the



TC12072JR  
Figure 142.3  
Yield enhancement caused by alphas versus the fractional alpha energy  $f_{\alpha}$ . Points 1–3 represent simulations with mass and velocity similar to current NIF ID targets (see Fig. 142.4).

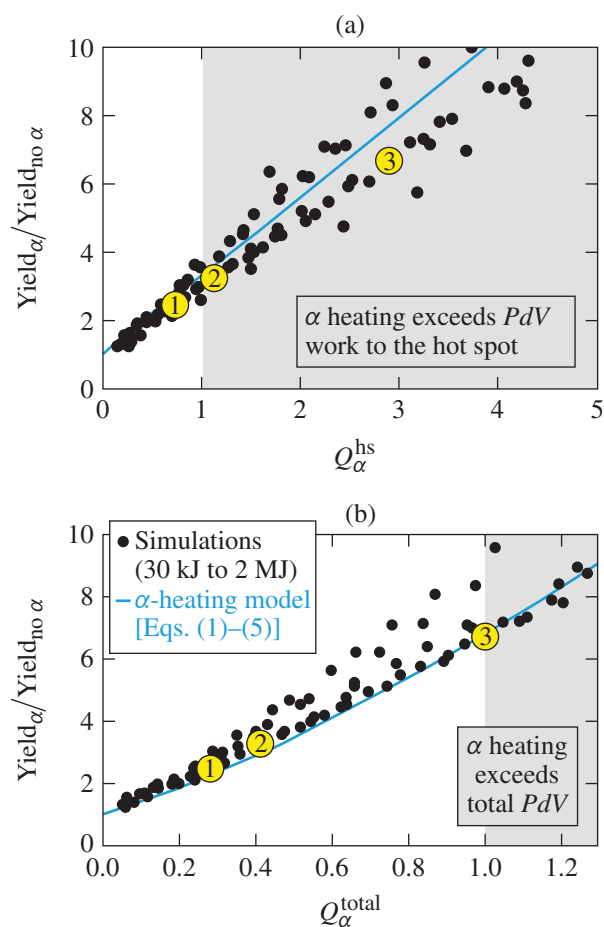
high-foot target N140120 (Ref. 18) (point 1 in Fig. 142.3), the fractional alpha energy is about 0.36 and the corresponding yield amplification of  $\approx 2.5$  is in agreement with the value obtained earlier through the  $\chi_\alpha$  method. The good agreement of the results from the alpha-heating model and the hydrodynamic simulations (Fig. 142.3) indicate that the model can be used to determine the input energy to the fusing plasma and, therefore, the onset of the burning-plasma regime. Energy is supplied to the DT plasma starting from the DT fuel's kinetic energy  $E_k(0) = 1/2 M_{DT} V_{imp}^2$ , where 0 is the beginning of the deceleration phase. Only a fraction of the kinetic energy is transformed into DT internal energy through the  $PdV$  work. At bang time, the kinetic energy converted to internal energy is  $E_{PdV}^{tot} = E_k(0) - E_k(t_{bang})$ . Of that fraction, a portion is transferred to the dense shocked shell ( $E_{PdV}^{ss}$ ) and the remainder to the hot spot ( $E_{PdV}^{hs}$ ). It is convenient to define two  $Q_\alpha$  parameters, one for the hot spot and one for the entire compressed core:

$$Q_\alpha^{hs} \equiv \frac{0.5E_\alpha}{E_{PdV}^{hs}}, \quad Q_\alpha^{tot} \equiv \frac{0.5E_\alpha}{E_{PdV}^{tot}}. \quad (15)$$

In these definitions, we retain the contribution of all the alpha particles up to bang time, including those that escape. The ablative flow carries the escaping alpha energy back into the hot spot and such energy is counted as input to the hot spot. The value  $Q_\alpha^{hs} > 1$  implies that the alpha heating exceeds the compression work to the hot spot and the hot-spot plasma enters the burning-plasma regime, where the alpha heating is the dominant heating mechanism. Additional  $PdV$  work is done on the shell itself as the return shock propagates outward and more shell material is slowed down and compressed. While few fusion reactions occur in the dense shell at yield amplifications below 10, the compressed shell provides the inertial confinement to the hot-spot pressure. The  $PdV$  work to the shell is not a direct input to the fusing plasma, but a highly compressed shell increases the confinement time and, therefore, the fusion yield of the hot spot. In the second definition of  $Q_\alpha$ , the total  $PdV$  work is included in the denominator and the condition  $Q_\alpha^{tot} > 1$  represents the regime where the alpha heating exceeds the total compression work. The  $PdV$  work to the hot spot can be calculated in 1-D from the integral

$$4\pi \int_{R(0)}^{R_{stag}} PR^2 dR,$$

where  $R_{stag}$  is the hot-spot stagnation radius. Both quantities can be computed from the model [Eqs. (1)–(5)] as well as from 1-D hydro simulations of the implosions. In 2-D and 3-D, extracting the  $PdV$  work is more complicated and will be addressed in a forthcoming article. Figure 142.4 shows the yield amplifications versus  $Q_\alpha^{hs}$  and  $Q_\alpha^{tot}$  and compares the result of the model [Eqs. (1)–(5)] with hydro simulations. From Fig. 142.4(a), the onset of the hot-spot burning-plasma regime occurs at yield amplifications of about 3.5. For current NIF ID implosions with  $M_{DT} \approx 0.18$  mg and fuel kinetic energies  $\sim 12$  to 15 kJ, this corresponds to a neutron yield of  $\sim 1.8 \times 10^{16}$



TC12073JR

Figure 142.4  
Plots of the yield amplification versus the hot-spot  $Q_\alpha$  and the total  $Q_\alpha$  from the model [Eqs. (1)–(5)] (solid curve) and from 1-D simulations (circles). The shaded areas identify the burning-plasma regimes. The three yellow circles (1–3) with yield amplification  $\sim 2.5\times$  [like shot N140120 (Ref. 19)],  $3.3\times$ , and  $6.7\times$  have a fuel kinetic energy of 12 to 15 kJ, and a DT mass  $\approx 0.18$  mg like current NIF ID experiments. Point 2 is located at the onset of hot-spot burning plasma. Point 3 is in the full burning-plasma regime.

(or  $\sim 50$  kJ) as indicated by point 2 in Fig. 142.4(a). The regime where the alpha heating exceeds the total  $PdV$  work occurs for yield amplifications  $\sim 7$ , corresponding to a yield  $\sim 4.5 \times 10^{16}$  (or  $\sim 120$  kJ) represented by point 3 in Fig. 142.4(b). The two measurable parameters  $f_\alpha$  and  $\chi_\alpha$  can be used to determine the onset of the burning-plasma regimes. Using Figs. 142.2 and 142.3, the hot-spot burning-plasma regime is achieved for  $f_\alpha \approx 0.45$  and  $\chi_\alpha \approx 1.2$ , while the full burning-plasma regime is achieved for  $f_\alpha \approx 0.7$  and  $\chi_\alpha \approx 1.8$ . The curves in Figs. 142.2–142.4 are used to assess the onset of the burning-plasma regime in ICF and the requirements on the implosion hydrodynamics to achieve ignition. For instance, the value  $\chi_{\text{no}\alpha} \approx 0.66$  for N140120 indicates that the no- $\alpha$  hydrodynamics must improve to raise the value of  $\chi_{\text{no}\alpha}$  by  $\geq 50\%$  to achieve ignition on the NIF.

## ACKNOWLEDGMENT

The authors thank Dr. J. Lindl, Dr. P. Patel, and Prof. D. Shvarts for many useful discussions. This work has been supported by the U.S. Department of Energy under Cooperative Agreement No. DE-FC02-04ER54789 (Fusion Science Center supported by the Office of Fusion Energy Sciences) and DE-NA0001944 (National Nuclear Security Administration), the New York State Energy Research Development Authority, and the University of Rochester. The support of DOE does not constitute an endorsement by DOE of the views expressed in this article.

## REFERENCES

1. J. Nuckolls *et al.*, *Nature* **239**, 139 (1972).
2. S. Atzeni and J. Meyer-ter-Vehn, *The Physics of Inertial Fusion: Beam Plasma Interaction, Hydrodynamics, Hot Dense Matter*, International Series of Monographs on Physics (Clarendon Press, Oxford, 2004); J. D. Lindl, *Inertial Confinement Fusion: The Quest for Ignition and Energy Gain Using Indirect Drive* (Springer-Verlag, New York, 1998).
3. O. A. Hurricane *et al.*, *Nature* **506**, 343 (2014).
4. M. J. Edwards, P. K. Patel, J. D. Lindl, L. J. Atherton, S. H. Glenzer, S. W. Haan, J. D. Kilkenny, O. L. Landen, E. I. Moses, A. Nikroo, R. Petrasso, T. C. Sangster, P. T. Springer, S. Batha, R. Benedetti, L. Bernstein, R. Betti, D. L. Bleuel, T. R. Boehly, D. K. Bradley, J. A. Caggiano, D. A. Callahan, P. M. Celliers, C. J. Cerjan, K. C. Chen, D. S. Clark, G. W. Collins, E. L. Dewald, L. Divol, S. Dixit, T. Doepfner, D. H. Edgell, J. E. Fair, M. Farrell, R. J. Fortner, J. Frenje, M. G. Gatu Johnson, E. Giraldez, V. Yu. Glebov, G. Grim, B. A. Hammel, A. V. Hamza, D. R. Harding, S. P. Hatchett, N. Hein, H. W. Herrmann, D. Hicks, D. E. Hinkel, M. Hoppe, W. W. Hsing, N. Izumi, B. Jacoby, O. S. Jones, D. Kalantar, R. Kauffman, J. L. Kline, J. P. Knauer, J. A. Koch, B. J. Koziolowski, G. Kyrala, K. N. LaFortune, S. Le Pape, R. J. Leeper, R. Lerche, T. Ma, B. J. MacGowan, A. J. MacKinnon, A. MacPhee, E. R. Mapoles, M. M. Marinak, M. Mauldin, P. W. McKenty, M. Meezan, P. A. Michel, J. Milovich, J. D. Moody, M. Moran, D. H. Munro, C. L. Olson, K. Opachich, A. E. Pak, T. Parham, H.-S. Park, J. E. Ralph, S. P. Regan, B. Remington, H. Rinderknecht, H. F. Robey, M. Rosen, S. Ross, J. D. Salmonson, J. Sater, D. H. Schneider, F. H. Séguin, S. M. Sepke, D. A. Shaughnessy, V. A. Smalyuk, B. K. Spears, C. Stoeckl, W. Stoeffl, L. Suter, C. A. Thomas, R. Tommasini, R. P. Town, S. V. Weber, P. J. Wegner, K. Widman, M. Wilke, D. C. Wilson, C. B. Yeamans and A. Zylstra, *Phys. Plasmas* **20**, 070501 (2013).
5. J. P. Freidberg, *Plasma Physics and Fusion Energy* (Cambridge University Press, Cambridge, England, 2007).
6. J. D. Lawson, *Proc. Phys. Soc. Lond. B* **70**, 6 (1957).
7. P. Y. Chang, R. Betti, B. K. Spears, K. S. Anderson, J. Edwards, M. Fatenejad, J. D. Lindl, R. L. McCrory, R. Nora, and D. Shvarts, *Phys. Rev. Lett.* **104**, 135002 (2010); R. Betti, P. Y. Chang, B. K. Spears, K. S. Anderson, J. Edwards, M. Fatenejad, J. D. Lindl, R. L. McCrory, R. Nora, and D. Shvarts, *Phys. Plasmas* **17**, 058102 (2010).
8. R. Betti, K. Anderson, V. N. Goncharov, R. L. McCrory, D. D. Meyerhofer, S. Skupsky, and R. P. J. Town, *Phys. Plasmas* **9**, 2277 (2002).
9. A. Schiavi and S. Atzeni, *Phys. Plasmas* **14**, 070701 (2007).
10. R. Kishony and D. Shvarts, *Phys. Plasmas* **8**, 4925 (2001).
11. L. Spitzer, *Physics of Fully Ionized Gases* (Interscience Publishers, New York, 1956).
12. O. N. Krokhin and V. B. Rozanov, *Sov. J. Quantum Electron.* **2**, 393 (1973).
13. J. Delettrez, R. Epstein, M. C. Richardson, P. A. Jaanimagi, and B. L. Henke, *Phys. Rev. A* **36**, 3926 (1987).
14. P. B. Radha, T. J. B. Collins, J. A. Delettrez, Y. Elbaz, R. Epstein, V. Yu. Glebov, V. N. Goncharov, R. L. Keck, J. P. Knauer, J. A. Marozas, F. J. Marshall, R. L. McCrory, P. W. McKenty, D. D. Meyerhofer, S. P. Regan, T. C. Sangster, W. Seka, D. Shvarts, S. Skupsky, Y. Srebro, and C. Stoeckl, *Phys. Plasmas* **12**, 056307 (2005).
15. B. K. Spears *et al.*, *Phys. Plasmas* **19**, 056316 (2012).
16. S. W. Haan, J. D. Lindl, D. A. Callahan, D. S. Clark, J. D. Salmonson, B. A. Hammel, L. J. Atherton, R. C. Cook, M. J. Edwards, S. Glenzer, A. V. Hamza, S. P. Hatchett, M. C. Herrmann, D. E. Hinkel, D. D. Ho, H. Huang, O. S. Jones, J. Kline, G. Kyrala, O. L. Landen, B. J. MacGowan, M. M. Marinak, D. D. Meyerhofer, J. L. Milovich, K. A. Moreno, E. I. Moses, D. H. Munro, A. Nikroo, R. E. Olson, K. Peterson, S. M. Pollaine, J. E. Ralph, H. F. Robey, B. K. Spears, P. T. Springer, L. J. Suter, C. A. Thomas, R. P. Town, R. Vesey, S. V. Weber, H. L. Wilkens, and D. C. Wilson, *Phys. Plasmas* **18**, 051001 (2011).
17. B. K. Spears and J. D. Lindl, "Ignition Metrics and Their Role in Setting Specifications and Evaluating Progress Toward Ignition on the NIF," Lawrence Livermore National Laboratory, Livermore, CA (internal report, unpublished).
18. O. A. Hurricane, D. A. Callahan, D. T. Casey, E. L. Dewald, T. R. Dittrich, T. Döppner, M. A. Barrios Garcia, D. E. Hinkel, L. F. Berzak Hopkins, P. Kervin, J. L. Kline, S. Le Pape, T. Ma, A. G. MacPhee, J. L. Milovich, J. Moody, A. E. Pak, P. K. Patel, H.-S. Park, B. A. Remington, H. F. Robey, J. D. Salmonson, P. T. Springer, R. Tommasini, L. R. Benedetti, J. A. Caggiano, P. Celliers, C. Cerjan, R. Dylla-Spears, D. Edgell, M. J. Edwards, D. Fittinghoff, G. P. Grim, N. Guler, N. Izumi, J. A. Frenje, M. Gatu Johnson, S. Haan, R. Hatarik, H. Herrmann, S. Khan, J. Knauer, B. J. Koziolowski, A. L. Kritcher, G. Kyrala, S. A. Maclaren, F. E. Merrill, P. Michel, J. Ralph, J. S. Ross, J. R. Rygg, M. B. Schneider, B. K. Spears, K. Widmann, and C. B. Yeamans, *Phys. Plasmas* **21**, 056314 (2014).
19. C. Cerjan, P. T. Springer, and S. M. Sepke, *Phys. Plasmas* **20**, 056319 (2013).
20. J. J. MacFarlane *et al.*, *High Energy Density Phys.* **3**, 181 (2007).

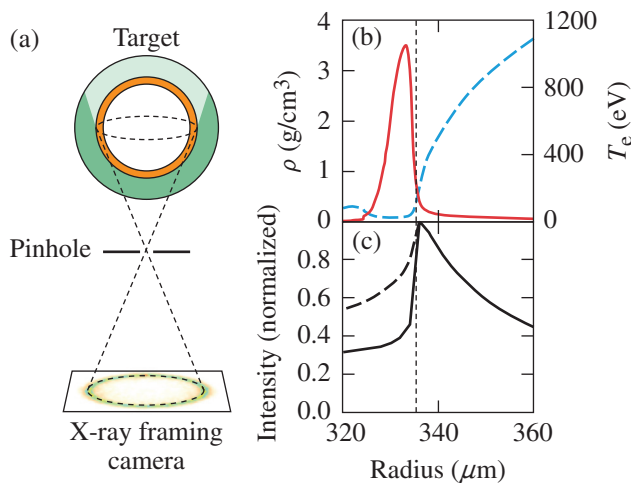
# Measurements of the Ablation-Front Trajectory and Low-Mode Nonuniformity in Direct-Drive Implosions Using X-Ray Self-Emission Shadowgraphy

## Introduction

In direct-drive inertial confinement fusion (ICF), laser beams are focused onto the surface of a fusion capsule that is imploded to reach thermonuclear ignition.<sup>1</sup> The beams ablate the target surface and drive the shell to high velocities. At maximum compression, a fraction of the kinetic energy is transferred into the internal energy of the hot spot, where fusion reactions are initiated. The minimum laser energy required for ignition is a strong function of the shell's maximum implosion velocity ( $E_{\min} \propto V_{\text{imp}}^{-6}$ ) (Ref. 2), which highlights the importance of accurately measuring it. During the compression, low-mode

nonuniformities that grow at the ablation surface result in distortion of the hot spot and a reduction in implosion performance.

A self-emission x-ray shadowgraphy (SES) technique<sup>4</sup> [Fig. 142.5(a)] has been applied to ICF experiments to measure the ablation-front trajectory, velocity,<sup>5</sup> and low-mode nonuniformity<sup>6–8</sup> of targets imploded on the OMEGA Laser System<sup>9</sup> and at the National Ignition Facility (NIF).<sup>10</sup> A pinhole array is used to image the soft x rays (>1 keV, spectrally filtered using 25.4  $\mu\text{m}$  of Be) emitted in the coronal plasma of an imploding target onto a four-strip x-ray framing camera (XRFC) to obtain 12 (three per strip) time-resolved images of an imploding target. The steep inner edge observed in the intensity profile of the image is used to determine the position of the ablation surface [Figs. 142.5(b) and 142.5(c)]. This edge is created by the combination of the limb effect of soft x rays emitted in the coronal plasma and the absorption in the cold dense shell of the x rays, emitted at the back side of the target. The absorption steepens the gradient by reducing the emission by a factor of 2 over a few microns in its direction [Fig. 142.5(c)]. Because this gradient is steep and governed by the absorption where the plasma temperature goes to zero, the position of the mid-intensity point in this edge is an excellent measure of the position of the ablation front (the position is defined by where the electron temperature is 100 eV).



E23816JR

Figure 142.5

(a) Schematic of the self-emission x-ray shadowgraphy technique: x rays emitted by the coronal plasma (dark green area) are imaged by a pinhole onto an x-ray framing camera. The shell (orange area) prevents the x rays emitted at the back of the shell (light green area) from reaching the detector. (b) The simulated shell density (red curve, left axis) and electron temperature (dashed blue curve, right axis) profiles were post-processed with *Spect3D* (Ref. 3) to calculate the (c) intensity profile. The mid-intensity point in the inner gradient corresponds to the position of the ablation front (vertical dashed black line). The intensity lineout calculated without absorption of the shell is plotted in (c) (dashed curve). The difference between the two intensity lineouts emphasizes the effect of the absorption of the x rays emitted at the back of the target in the shell, which significantly steepens the inner gradient.

This article describes different methods used to characterize the diagnostic, showing that the accuracy of the measurement of the ablation front's position is  $\delta R = \pm 1.15 \mu\text{m}$ . Two techniques were used to measure the image-to-image timing to within  $\delta(\Delta t) = \pm 2.5 \text{ ps}$ . The method used to time the images to the laser pulse (absolute timing) was demonstrated to have an accuracy of  $\delta t = \pm 10 \text{ ps}$ .

The SES technique is applied to symmetric implosions on the OMEGA Laser System and to polar-direct-drive experiments on the NIF. The OMEGA laser is configured for symmetric irradiation, while the beam geometry on the NIF is currently optimized for x-ray geometry with no beams located around the equator. Initial polar-direct-drive experiments

repoint the beams toward the equator to generate a uniform ablation.<sup>11</sup> In these experiments, the angularly averaged radius provides a measure of the ablation-front trajectory to within  $\delta(R_{av}) = \pm 0.15 \mu\text{m}$  and velocity to within  $\delta V/V = \pm 3\%$ . In the symmetrically driven implosions, where the nonuniformity has a random phase, the amplitude and the phase of the modes are determined using a Fourier decomposition. In this case, the amplitude of mode 2 is measured to within  $\delta(\text{Fou}_2) = \pm 0.25\%$ . In the polar-direct-drive implosions, the dominant low-mode nonuniformities are axisymmetric around the polar axis, and the mode amplitudes are determined using a Legendre polynomial decomposition. With this method, the amplitudes of modes 2, 4, and 6 are determined to within  $\delta(\text{Leg}_n) = \pm 0.5\%$ .

### Characterization of the Framing Camera

The accuracy in the time-resolved measurements of the ablation-front trajectory, velocity, and low-mode nonuniformity using the SES technique is determined by the precision of the measurement of the ablation-front position ( $R \pm \delta R$ ), the accuracy of the image-to-image timing [ $\Delta t \pm \delta(\Delta t)$ ], and the absolute timing between the images and the laser pulse ( $t \pm \delta t$ ) (Refs. 12 and 13).

#### 1. Radial Accuracy (Pinhole Imaging)

To optimize the resolution of the steep gradient generated by self-emission x-ray imaging, the optimal pinhole diameter  $d_{\text{opt}} = \sqrt{244 \lambda L_{\text{tp}} [M / (M + 1)]}$  was determined by setting the diameter of the geometric image of a point [ $d_G = (M + 1)d$ , where  $d$  is the diameter of the pinhole] equal to the diameter of the diffraction image of a point [ $d_D = (2.44 \lambda / d)L_{\text{tp}}M$ , where

$M$  is the magnification of the pinhole imaging system,  $\lambda$  is the x-ray wavelength, and  $L_{\text{tp}}$  is the distance between the target and the pinhole]. On OMEGA, this corresponds to  $d_{\text{opt}} = 10 \mu\text{m}$  when using  $M = 6$ ,  $\lambda = 1.24 \text{ nm}$ , and  $L_{\text{tp}} = 40 \text{ mm}$ . This configuration results in the point-spread function (PSF) shown in Fig. 142.6(a) calculated using the coherent ray-tracing program *FRED*.<sup>14</sup> The calculation takes into account the pinhole imaging (geometry and diffraction) and the modulation transfer function of the microchannel plate of the XRFC.<sup>15</sup> From this PSF calculation, the minimum distance between two points in the object space that can be distinguished in the image plane is given by the full width at half maximum (FWHM) of the PSF ( $12 \mu\text{m}$ ).

Figure 142.6(b) compares intensity profiles from measured self-emission images with profiles calculated by post-processing hydrodynamic simulations with *Spect3D*. The synthetic x-ray images were convolved with the PSF of the diagnostic [Fig. 142.6(a)]. Excellent agreement was obtained, which shows that both the simulation of the soft x rays emitted by the imploding target and the modeling of the response of the imaging system are well reproduced.

The center of the measured images was determined iteratively. Intensity profiles were taken along chords through the center of the image. The positions of the mid-intensity point on each profile were determined and a new center was calculated fitting the points with a circle using a  $\chi^2$  analysis. This process was repeated until the center position changed by no more than  $0.1 \mu\text{m}$ .

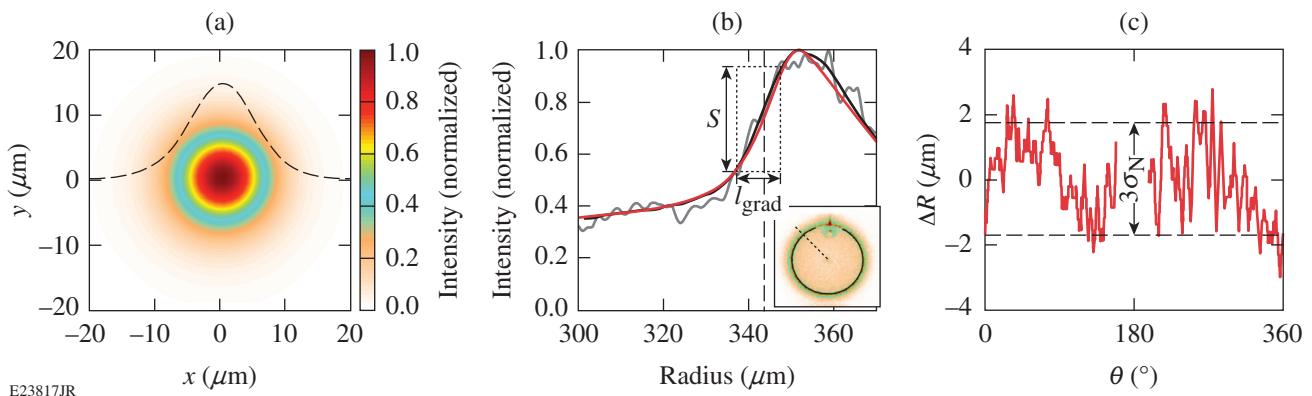


Figure 142.6

(a) Point-spread function for the x-ray imaging diagnostics calculated for the setup used on the OMEGA Laser System. A lineout of the point-spread function is plotted (dashed curve). (b) Comparison of an intensity profile (gray curve) measured along the dotted black lines displayed on the self-emission images (insets) with the calculated profiles (red curve). The position of the ablation front is indicated (vertical dashed line). The profile azimuthally averaged over the entire image is plotted (solid black curve). (c) Variation of the position of the mid-intensity point in the inner gradient relative to the best-fit circle is shown for all angles (red curve).

The accuracy in the position of the mid-intensity point in the inner gradient of the measured profile can be determined using the intercept theorem  $N/(2\delta R) = S/l_{\text{grad}}$ , where  $\delta R$  is the variation in the measured radius,  $N = 3\sigma_N$ , and  $\sigma_N$  is the standard deviation of the noise. The signal ( $S = 0.4$ ) is defined as the difference in x-ray intensities over the length of the inner gradient  $l_{\text{grad}}$  [Fig. 142.6(b)]. Applying this to the example shown in Fig. 142.6(b),  $\delta R = 0.5 l_{\text{grad}}/(S/N) \sim 1.4 \mu\text{m}$ , where  $l_{\text{grad}} = 9 \mu\text{m}$  and  $S/N = 10$ .

In spherical experiments, the position of the ablation front was determined by averaging the position of the mid-intensity point in the inner gradient over all angles. This improved the accuracy of the measured ablation front's position by a factor of  $\sqrt{N_p}$ , where  $N_p = 2\pi R/d_{\text{PSF}}$  is the number of independent measurements,  $R$  is the averaged radius, and  $d_{\text{PSF}}$  is the FWHM of the PSF. On OMEGA, this resulted in an accuracy in the  $360^\circ$  angularly averaged radius of  $\delta R_{\text{av}} < 0.15 \mu\text{m}$ , where  $d_{\text{PSF}} \approx 12 \mu\text{m}$  and  $\sqrt{N_p} \approx 10$  for  $R = 200 \mu\text{m}$ .

Figure 142.6(c) shows that the  $3\sigma$  variation in the measured radius around the image relative to the  $360^\circ$  angularly averaged radius is  $(3\sigma_R)_{360^\circ} \approx 3.5 \mu\text{m}$ . This is consistent with the peak-to-valley variation in the measured radius calculated from the intercept theorem  $[(2\delta R)_{\text{intercept}} \approx (3\sigma_R)_{360^\circ}]$ .

## 2. Image-to-Image Timing (Interstrip Timing)

The XRFC uses four microchannel plates to time resolve the pinhole images. The microchannel plates are activated by independently timed high-voltage pulses, and the accuracy in the timing between images on subsequent plates (interstrip timing) is given by the accuracy of the high-voltage pulsers [Fig. 142.7(a)]. Each electrical pulse is created by a pulser and travels through a delay box that generates a different delay for each strip. The jitter in the interstrip timing corresponds primarily to the jitter between two pulsers.

The interstrip timing was determined by using an 8-GHz oscilloscope to measure the time difference between the electrical pulses that come from different delay lines. The timing error between two channels was calibrated by splitting an electrical pulse and sending each pulse to two different inputs of the oscilloscope through two cables of the same length. The jitter between two pulsers was determined by repeating the measurements several times. For the XRFC setup used on the OMEGA Laser System, the interstrip timing was measured [Fig. 142.7(b)]. An error of  $\pm 4$  ps in the interstrip timing was inferred from the 8 ps of drift in the oscilloscope determined before and after the measurements. A standard deviation of

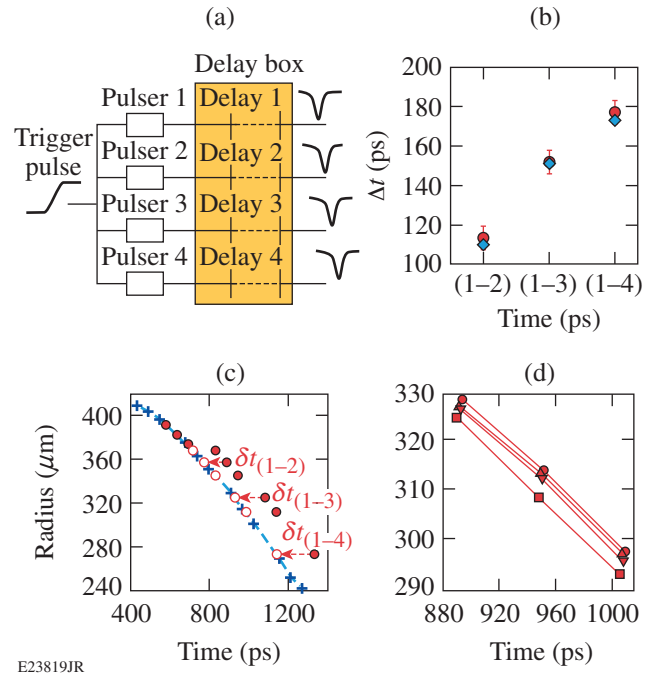


Figure 142.7

(a) Schematic of the x-ray framing camera high-voltage lines: Four pulsers are launched by a trigger pulse and generate four pulses that are delayed independently by a delay box and sent to the four strips of the microchannel plate. (b) Comparison of the interstrip timing measured off-line (method 1, red points) and on real shot (method 2, blue points) (c) Comparison of the trajectory measured by the reference camera (blue curve) with the trajectory measured by the uncalibrated camera (red circles). Differences of  $\delta t_{(1-2)} = 115$  ps,  $\delta t_{(1-3)} = 152$  ps, and  $\delta t_{(1-4)} = 190$  ps were measured between the requested and the real interstrip timings between the strips (1–2), (1–3), and (1–4) (dashed arrows). (d) Comparison of the trajectories measured on strip 1 (squares), strip 2 (triangles), strip 3 (inverse triangles), and strip 4 (circles) when the delay box was set to get zero interstrip timing: a residual delay of 10 ps, 7 ps, and 18 ps was measured between strips (1–2), (1–3), and (1–4), respectively.

the jitter between two pulsers of  $\sigma_p = 1.5$  ps was determined by repeating each measurement five times. This resulted in a jitter of the interstrip timing of  $\delta(\Delta t) = \pm 3\sigma_p/2 = \pm 2.5$  ps.

To verify the interstrip timing, the ablation-front trajectory was simultaneously measured using two XRFC's [Fig. 142.7(c)]. First, the residual interstrip timings of the reference XRFC with the synchronized delay box were determined by measuring the ablation-front trajectory of an imploding target. Small differences in the radii of the ablation front between each strip were used to quantify the residual time difference between each strip [Fig. 142.7(d)]. To set the interstrip timing to calibrated values, precalibrated delay cables were connected to the output of the synchronized delay box. The reference XRFC was used to measure the reference trajectory, and the interstrip timing of the second XRFC was measured by comparing the difference between

the requested interstrip timing and the measured interstrip timing [Fig. 142.7(c)]. The measurements were repeated three times to determine the interstrip timings to within a few ps. The interstrip timings are presented in Fig. 142.7(b). An error in the interstrip measurement of  $\delta(\Delta t) = \pm 3\sigma_s/2 = \pm 2.5$  ps was determined, where  $\sigma_s = 1.7$  ps is the standard deviation of the measurement of the interstrip timing over multiple repeated shots. Excellent agreement was obtained between the two methods [Fig. 142.7(b)].

### 3. Absolute Timing

The variation of the absolute timing is determined on each shot by measuring the time difference between the electrical monitor pulse from the XRFC and the optical fiducial, which is a time reference for the laser pulse. To calibrate the absolute timing, the time difference between the laser and the XRFC was measured on a timing reference shot.

The timing reference shot used a 4-mm-diam gold target with multiple laser pulses that rose over 100 ps to a 1-ns-long flat-top intensity. The time-resolved x-ray intensities emitted by the gold plasmas were measured on the XRFC (see images in Fig. 142.8) and used to determine the rise of the laser intensity after adjusting for the conversion of the x-ray intensity to laser intensity  $I_{\text{laser}} \propto I_{\text{x ray}}^{-3.4}$  (Ref. 16), where  $I_{\text{x ray}}$  and  $I_{\text{laser}}$  are the x-ray and laser intensities, respectively. The pulse shape measured by the XRFC was compared with the optical pulse shape [Fig. 142.8(b)]

to determine the absolute timing. To compare the x-ray signals measured between different beams, all measurements were normalized to the measured laser beam energy  $I_{\text{norm}} = I_{\text{laser}}/E_{\text{laser}}$ . To account for the variation in the sensitivity of the camera, a few beams are advanced in time by 400 ps to generate a constant x-ray flux (top images in Fig. 142.8) and each x-ray intensity was normalized to the x-ray intensity measured on the closest flat-field (FF) spot ( $I_{\text{FF}} = I_{\text{norm}}/E_{\text{norm,FF}}$ ). Figure 142.8(c) shows the variation of the absolute timing over multiple shots. An accuracy in the absolute timing of  $\delta t = \pm 3\sigma_{\Delta t}/2 = \pm 10$  ps was determined, where  $\sigma_{\Delta t}$  is the standard deviation of the variation of the absolute-timing calibration number.

### Application

The SES technique was applied to measure the ablation-front trajectory, velocity, and nonuniformity of an imploding target in direct-drive implosions at the Omega Laser Facility and low-mode nonuniformities on the NIF.

#### 1. Ablation-Front Trajectory and Velocity on the OMEGA Laser System

The experiment employed 60 ultraviolet ( $\lambda_0 = 351$  nm) laser beams on the OMEGA laser. The laser beams uniformly illuminated the target and were smoothed by polarization smoothing,<sup>17</sup> smoothing by spectral dispersion,<sup>18</sup> and distributed phase plates<sup>19</sup> (fourth-order super-Gaussian with 95% of

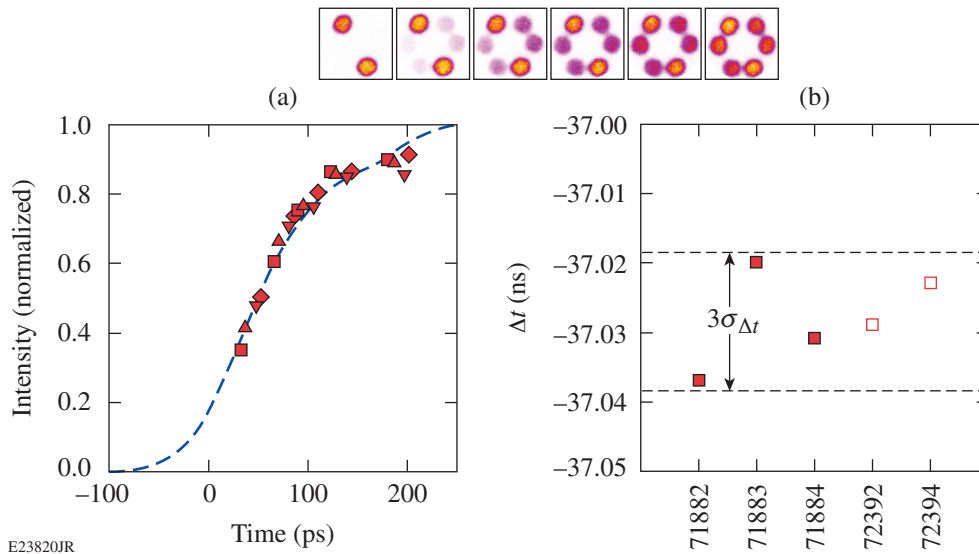


Figure 142.8

(a) Comparison of the rise of the normalized laser intensity (red points) calculated from the rise of the x-ray intensity generated by a gold sphere irradiated by six laser pulses measured on an XRFC with the optical laser pulse (dashed blue curve). Two beams were advanced 400 ps to measure the flat field of the framing camera. The series of images recorded on the framing camera during the rise of the x-ray emission is shown at the top of the figure. (b) Comparison of the absolute timing calibration measured over two campaigns (open and solid squares correspond to two different campaigns). The standard deviation of the variation of this number is shown on the figure.

the energy contained within the initial target diameter). One 100-ps-long picket was used to set the target implosion onto a low adiabat<sup>20</sup> followed by a 2-ns step pulse that drove the target to its final velocity [Fig. 142.9(a)]. The total laser energy on the target was 19.6 kJ, which resulted in a maximum laser power of 11 TW. The target had an 867.8- $\mu\text{m}$  outer diameter with a 26.8- $\mu\text{m}$ -thick CH ablator covered by 0.1  $\mu\text{m}$  of Al and filled with deuterium at 10.5 atm.

The images displayed at the top of Fig. 142.9 correspond to self-emission images that were recorded using the setting of the SES diagnostic described in the **Introduction** (p. 83). Images were time integrated over  $\sim 40$  ps (Ref. 13) and interstrip timings of 250 ps were used. Three framing cameras were used to determine the trajectory of the ablation front over the entire length of the main drive.

Figure 142.9 compares the measured ablation-front trajectory and in-flight shell velocity with hydrodynamic simulations. The accuracy in the measurement of the ablation-front velocity calculated between two images of two consecutive strips (averaged over  $\Delta t \approx 250$  ps) is given by

$$\delta V / V = \delta(\Delta t) / \Delta t + \sqrt{2} \delta R_{\text{av}} / \Delta R_{\text{av}} \approx 3\%,$$

where  $\delta(\Delta t) \approx 4$  ps is the error in the interstrip timing [dominated by the error in the measurement of  $\Delta t$  (see previous section)] and, for a velocity of 200 km/s,  $\Delta R_{\text{av}} = 50 \mu\text{m}$ . Simulations were

performed with the one-dimensional (1-D) hydrodynamic code *LILAC*<sup>21</sup> that include nonlocal electron transport<sup>22</sup> and cross-beam energy transfer (CBET).<sup>23</sup> Synthetic x-ray self-emission images were calculated using *Spect3D*. The images were convolved with the PSF of the diagnostic. The simulated trajectory and velocities were obtained by post-processing the synthetic images following the same method used on the experimental images. Excellent agreement between the position of the mid-intensity point and the position of the ablation front was obtained, showing that the hydrodynamic coupling is well modeled.

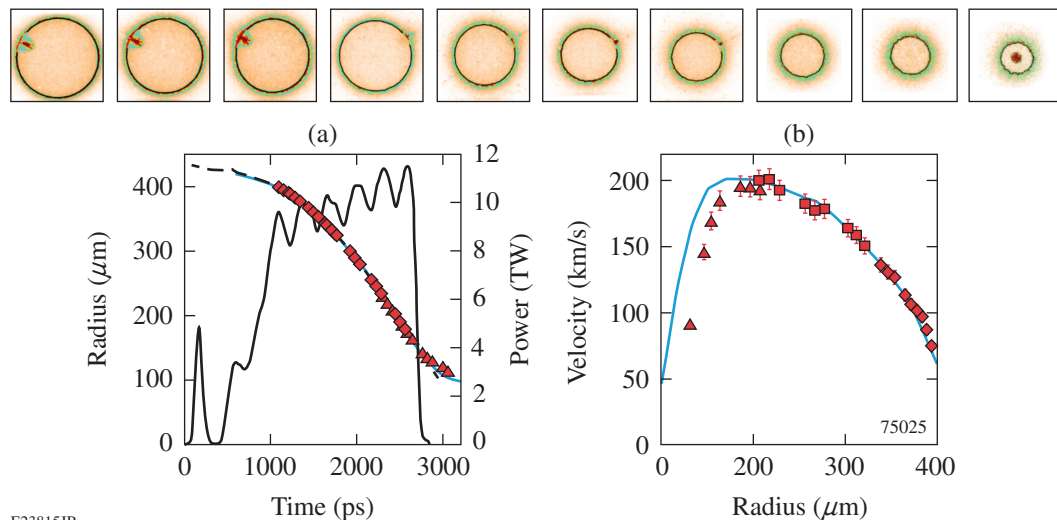
## 2. Ablation-Front Nonuniformity on OMEGA

To investigate the uniformity of the drive, the angular variation in the ablation surface was decomposed using a Fourier series. Figure 142.10(a) shows that mode 2 dominates the low-mode nonuniformity. Figure 142.10(b) shows that the amplitude of the low-mode nonuniformity grows linearly with radius and that the phase is nearly constant ( $\phi_2 = 89 \pm 14^\circ$ ).

For each radius, the amplitude of the mode 2 is defined by  $\text{Fou}_2 = 2 | \text{Fou}_2 | / N_{\text{DFT}}$ , where

$$\text{Fou}_2 = \sum_{j=0}^{N_{\text{DFT}}-1} \left[ \Delta R(\theta_j) / R_{\text{av}} \right] e^{-4i\pi j / N_{\text{DFT}}}$$

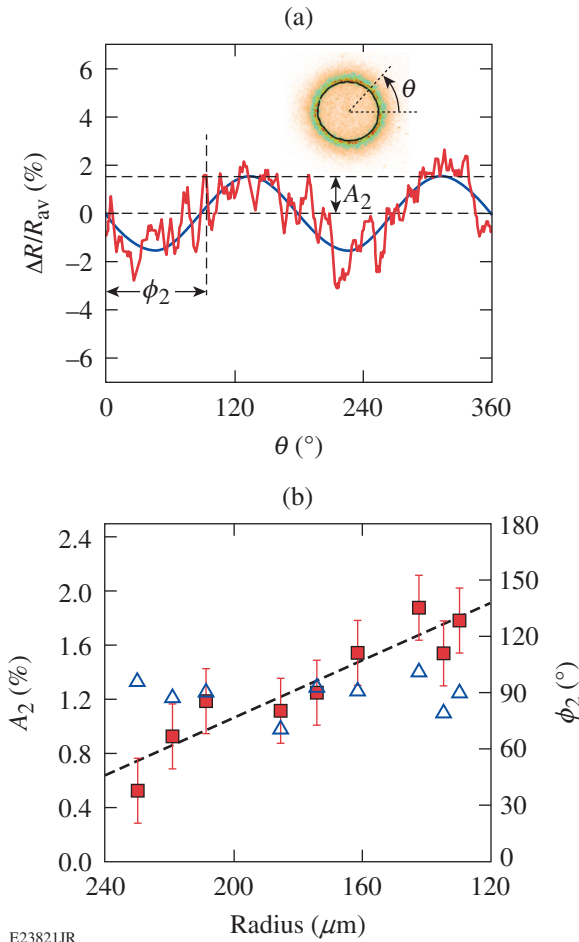
is the second coefficient of the Fourier transform of  $\Delta R(\theta) / R_{\text{av}}$  discretized over  $N_{\text{DFT}}$  points equally spaced in an angle around



E23815JR

Figure 142.9

A series of x-ray self-emission images (top) shows the implosion dynamics. Comparison of the measured (red symbols, each of which corresponds to a different camera) mid-intensity points in the (a) inner gradient trajectory and (b) velocity with the simulation (blue curve). In (a), the laser pulse is plotted as the solid black curve and the trajectory of the ablation front from the simulation as the dashed black curve.



E23821JR

Figure 142.10

(a) Comparison of the variation of  $\Delta R/R_{av}$  (red curve) with the mode 2, calculated using a discrete Fourier transform of the contour defined by  $f_2(\theta) = A_2 \cos(\theta + \phi_2)$  (blue curve). (b) Evolution of the amplitude (red points) and the phase (open blue triangles) of mode 2 during the implosion. The line best fit to the growth of the mode amplitude is plotted (dashed black line).

the contour,  $\Delta R(\theta_j) = R(\theta_j) - R_{av}$ , and  $\theta_j$  is the angle of the point  $j$ . When the contour is not defined over all angles, an algorithm is used to determine the discrete Fourier transform.<sup>24</sup>

An accuracy of  $\pm 0.25\%$  in the mode-2 measurement was determined and corresponds to three times the standard deviation of the distance between the points and the best-fit line [Fig. 142.10(b)]. This corresponds to an error in the mode amplitude of better than  $\pm 0.5 \mu\text{m}$ , which is slightly larger than the accuracy in the measurement of the averaged shell radius. The fact that the phase of the nonuniformity does not change significantly over the nine measurements and a variation of this constant phase was observed among different shots show that the mode is not an artifact of the diagnostic [Fig. 142.10(b)].

### 3. Ablation-Front Nonuniformity on the NIF

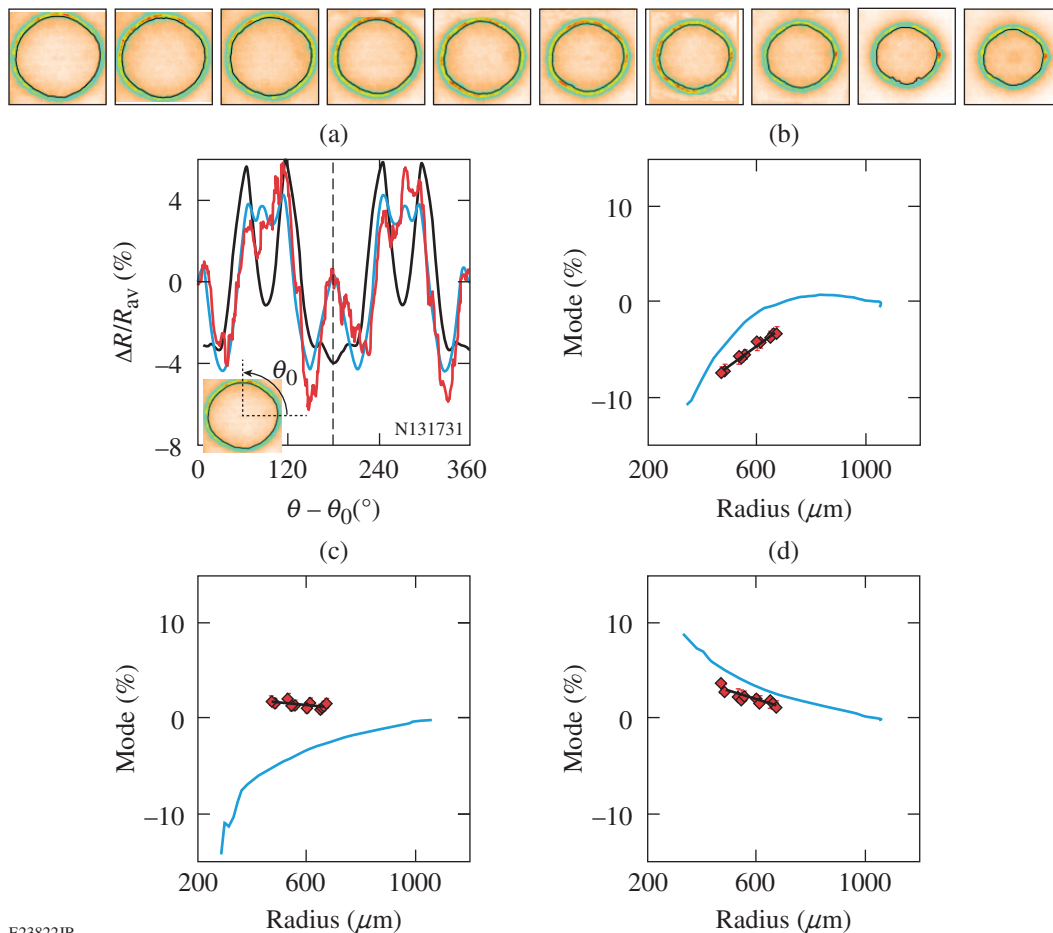
The SES technique was implemented on the NIF to measure shell trajectory, velocity, and low-mode nonuniformities in polar-direct-drive experiments (the experimental setup is detailed in Ref. 8). A series of images are presented at the top of Fig. 142.11. To increase the signal-to-noise ratio on the NIF experiments, the pinholes are larger than the optimum diameter ( $d_{\text{NIF}} = 60 \mu\text{m} > d_{\text{opt}} = 25 \mu\text{m}$ ), resulting in a  $32.5\text{-}\mu\text{m}$  FWHM of the PSF. In the polar-direct-drive configuration, the illumination is symmetric around the polar axis, so  $\Delta R/R_{av}$  is decomposed using Legendre polynomials with their axes of symmetry adjusted to be the polar axes. Figure 142.11(a) compares the contour with the curve that corresponds to the addition of the ten first Legendre polynomials of the contour decomposition. The good agreement between the two curves shows that the contour is nearly symmetric around the polar axis.

Figures 142.11(b)–142.11(d) compare the growth of modes 2, 4, and 6 of the ablation front with hydrodynamic simulations. In each case, the accuracy in the amplitude of the modes is better than  $\pm 0.5\%$ , which corresponds to three times the standard deviation of the distance between the points and the best-fit curves. Simulations were conducted using the two-dimensional (2-D) hydrodynamic code *DRACO*<sup>25</sup> with nonlocal electron transport and CBET models and the axis of symmetry along the polar axis. The simulated modes were obtained by post-processing simulations with *Spect3D*, convolving it with the PSF of the diagnostic, and determining the position of the inner gradient in the synthetic images. The differences observed between the calculated and the simulated mode amplitudes are primarily the result of an overdriven pole (or underdriven equator) [Fig. 142.11(a)] probably caused by errors in the 2-D nonlocal electron transport and CBET models.

The decomposition over Legendre polynomials is defined by

$$\Delta R/R(\theta_j - \theta_0) = \sum_{n=1}^{\infty} \left\{ \text{Leg}_n P_n \left[ \cos(\theta_j - \theta_0) \right] \right\},$$

where  $P_n$  is the Legendre polynomial  $n$ ,  $\text{Leg}_n$  is the coefficient,  $n$  is the Legendre mode, and  $\theta_0 = 90^\circ$  corresponds to the angle of the axis of symmetry [Fig. 142.11(a)]. The mode amplitudes are normalized to the norm of the Legendre polynomials relative to the L2 inner product  $\text{Leg}_n = \text{Leg}_n / [2/(2n+1)]^{0.5}$ . With this normalization factor for a symmetric signal, the amplitude of the modes defined with the Legendre polynomial



E23822JR

Figure 142.11

(Top) Series of x-ray self-emission images recorded on the NIF. (a) Comparison of measured  $\Delta R/R_{av}$  (red curve) with the curve obtained by adding the first ten Legendre polynomials of the decomposition. These are compared with the synthetic contour at an equivalent radius (solid black curve). The vertical axis of symmetry is plotted (vertical dashed black line) and the angle  $\theta_0$  of this vertical axis is indicated in the inset. The measured growths (red points) of (b) mode 2, (c) mode 4, and (d) mode 6 using a Legendre polynomial decomposition are compared with simulations (blue curve). An accuracy better than  $\pm 0.5\%$  in the mode-amplitude measurement was determined and corresponded to three times the standard deviation of the distance between the measurements and the best-fit line (black line).

is similar to the amplitude of the modes calculated using the Fourier decomposition.

### Conclusion

In summary, different methods used to characterize the self-emission x-ray shadowgraphy (SES) technique in the configuration used on OMEGA have been presented. The precise calculation of the PSF made it possible to determine the position of the ablation front to within  $\pm 1.15 \mu\text{m}$ . Two methods—one off-line, one on a shot—were compared to measure the interstrip timing of the x-ray framing camera to within  $\pm 2.5$  ps; excellent agreement was obtained. A method to measure the timing between the images and the laser pulse to within  $\pm 10$  ps was presented.

The SES technique was applied to measure the ablation-front trajectory, velocity, and mode-2 nonuniformity on symmetric implosions on OMEGA to within  $\delta(R_{av}) = \pm 0.15 \mu\text{m}$ ,  $\delta V/V = \pm 3\%$ , and  $\delta(\text{Fou}_2) = \pm 0.25\%$ , respectively. Excellent agreement was obtained with 1-D hydrodynamic simulations conducted with the code *LILAC*. The technique was applied in polar-direct-drive experiments performed on the NIF. The ablation-front low-mode nonuniformities were characterized using Legendre polynomial decomposition. Amplitudes of modes 2, 4, and 6 were compared with 2-D simulation results conducted with the hydrodynamic code *DRACO*. The observed differences are probably caused by errors in the 2-D nonlocal electron transport and CBET models.

## ACKNOWLEDGMENT

This material is based upon work supported by the Department of Energy National Nuclear Security Administration under Award Number DE-NA0001944, the University of Rochester, and the New York State Energy Research and Development Authority. The support of DOE does not constitute an endorsement by DOE of the views expressed in this article.

## REFERENCES

1. J. Nuckolls *et al.*, *Nature* **239**, 139 (1972).
2. M. C. Herrmann, M. Tabak, and J. D. Lindl, *Nucl. Fusion* **41**, 99 (2001).
3. J. J. MacFarlane *et al.*, *High Energy Density Phys.* **3**, 181 (2007).
4. D. T. Michel, C. Sorce, R. Epstein, N. Whiting, I. V. Igumenshchev, R. Jungquist, and D. H. Froula, *Rev. Sci. Instrum.* **83**, 10E530 (2012).
5. D. T. Michel, V. N. Goncharov, I. V. Igumenshchev, R. Epstein, and D. H. Froula, *Phys. Rev. Lett.* **111**, 245005 (2013).
6. D. H. Froula, I. V. Igumenshchev, D. T. Michel, D. H. Edgell, R. Follett, V. Yu. Glebov, V. N. Goncharov, J. Kwiatkowski, F. J. Marshall, P. B. Radha, W. Seka, C. Sorce, S. Stagnitto, C. Stoeckl, and T. C. Sangster, *Phys. Rev. Lett.* **108**, 125003 (2012).
7. D. T. Michel, R. S. Craxton, A. K. Davis, R. Epstein, V. Yu. Glebov, V. N. Goncharov, S. X. Hu, I. V. Igumenshchev, D. D. Meyerhofer, P. B. Radha, T. C. Sangster, W. Seka, C. Stoeckl, and D. H. Froula, *Plasma Phys. Control. Fusion* **57**, 014023 (2015).
8. M. Hohenberger, P. B. Radha, J. F. Myatt, S. LePape, J. A. Marozas, F. J. Marshall, D. T. Michel, S. P. Regan, W. Seka, A. Shvydkiy, T. C. Sangster, J. W. Bates, R. Betti, T. R. Boehly, M. J. Bonino, D. T. Casey, T. J. B. Collins, R. S. Craxton, J. A. Delettrez, D. H. Edgell, R. Epstein, G. Fiksel, P. Fitzsimmons, J. A. Frenje, D. H. Froula, V. N. Goncharov, D. R. Harding, D. H. Kalantar, M. Karasik, T. J. Kessler, J. D. Kilkenny, J. P. Knauer, C. Kurz, M. Lafon, K. N. LaFortune, B. J. MacGowan, A. J. Mackinnon, A. G. MacPhee, R. L. McCrory, P. W. McKenty, J. F. Meeker, D. D. Meyerhofer, S. R. Nagel, A. Nikroo, S. Obenshain, R. D. Petrasso, J. E. Ralph, H. G. Rinderknecht, M. J. Rosenberg, A. J. Schmitt, R. J. Wallace, J. Weaver, C. Widmayer, S. Skupsky, A. A. Solodov, C. Stoeckl, B. Yaakobi, and J. D. Zuegel, *Phys. Plasmas* **22**, 056308 (2015).
9. T. R. Boehly, D. L. Brown, R. S. Craxton, R. L. Keck, J. P. Knauer, J. H. Kelly, T. J. Kessler, S. A. Kumpan, S. J. Loucks, S. A. Letzring, F. J. Marshall, R. L. McCrory, S. F. B. Morse, W. Seka, J. M. Soures, and C. P. Verdon, *Opt. Commun.* **133**, 495 (1997).
10. E. M. Campbell and W. J. Hogan, *Plasma Phys. Control. Fusion* **41**, B39 (1999).
11. S. Skupsky, J. A. Marozas, R. S. Craxton, R. Betti, T. J. B. Collins, J. A. Delettrez, V. N. Goncharov, P. W. McKenty, P. B. Radha, T. R. Boehly, J. P. Knauer, F. J. Marshall, D. R. Harding, J. D. Kilkenny, D. D. Meyerhofer, T. C. Sangster, and R. L. McCrory, *Phys. Plasmas* **11**, 2763 (2004).
12. D. K. Bradley, P. M. Bell, J. D. Kilkenny, R. Hanks, O. Landen, P. A. Jaanimagi, P. W. McKenty, and C. P. Verdon, *Rev. Sci. Instrum.* **63**, 4813 (1992).
13. D. K. Bradley *et al.*, *Rev. Sci. Instrum.* **66**, 716 (1995).
14. See <http://www.photonengr.com/> for information regarding the *FRED* program.
15. V. A. Smalyuk, T. R. Boehly, D. K. Bradley, J. P. Knauer, and D. D. Meyerhofer, *Rev. Sci. Instrum.* **70**, 647 (1999).
16. F. J. Marshall, J. A. Delettrez, R. Epstein, R. Forties, R. L. Keck, J. H. Kelly, P. W. McKenty, S. P. Regan, and L. J. Waxer, *Phys. Plasmas* **11**, 251 (2004).
17. T. R. Boehly, V. A. Smalyuk, D. D. Meyerhofer, J. P. Knauer, D. K. Bradley, R. S. Craxton, M. J. Guardalben, S. Skupsky, and T. J. Kessler, *J. Appl. Phys.* **85**, 3444 (1999).
18. S. Skupsky, R. W. Short, T. Kessler, R. S. Craxton, S. Letzring, and J. M. Soures, *J. Appl. Phys.* **66**, 3456 (1989).
19. T. J. Kessler, Y. Lin, J. J. Armstrong, and B. Velazquez, in *Laser Coherence Control: Technology and Applications*, edited by H. T. Powell and T. J. Kessler (SPIE, Bellingham, WA, 1993), Vol. 1870, pp. 95–104.
20. V. N. Goncharov, T. C. Sangster, T. R. Boehly, S. X. Hu, I. V. Igumenshchev, F. J. Marshall, R. L. McCrory, D. D. Meyerhofer, P. B. Radha, W. Seka, S. Skupsky, C. Stoeckl, D. T. Casey, J. A. Frenje, and R. D. Petrasso, *Phys. Rev. Lett.* **104**, 165001 (2010).
21. J. Delettrez, *Can. J. Phys.* **64**, 932 (1986).
22. V. N. Goncharov, T. C. Sangster, P. B. Radha, R. Betti, T. R. Boehly, T. J. B. Collins, R. S. Craxton, J. A. Delettrez, R. Epstein, V. Yu. Glebov, S. X. Hu, I. V. Igumenshchev, J. P. Knauer, S. J. Loucks, J. A. Marozas, F. J. Marshall, R. L. McCrory, P. W. McKenty, D. D. Meyerhofer, S. P. Regan, W. Seka, S. Skupsky, V. A. Smalyuk, J. M. Soures, C. Stoeckl, D. Shvarts, J. A. Frenje, R. D. Petrasso, C. K. Li, F. Séguin, W. Manheimer, and D. G. Colombant, *Phys. Plasmas* **15**, 056310 (2008).
23. I. V. Igumenshchev, W. Seka, D. H. Edgell, D. T. Michel, D. H. Froula, V. N. Goncharov, R. S. Craxton, L. Divol, R. Epstein, R. Follett, J. H. Kelly, T. Z. Kosc, A. V. Maximov, R. L. McCrory, D. D. Meyerhofer, P. Michel, J. F. Myatt, T. C. Sangster, A. Shvydkiy, S. Skupsky, and C. Stoeckl, *Phys. Plasmas* **19**, 056314 (2012).
24. V. Ya. Liepin'sh, *Autom. Control Comput. Sci.* **30**, 27 (1996).
25. P. B. Radha, V. N. Goncharov, T. J. B. Collins, J. A. Delettrez, Y. Elbaz, V. Yu. Glebov, R. L. Keck, D. E. Keller, J. P. Knauer, J. A. Marozas, F. J. Marshall, P. W. McKenty, D. D. Meyerhofer, S. P. Regan, T. C. Sangster, D. Shvarts, S. Skupsky, Y. Srebro, R. P. J. Town, and C. Stoeckl, *Phys. Plasmas* **12**, 032702 (2005).

# Nanomechanical Properties of Single-Layer Optical Oxide Thin Films Used for High-Laser-Damage-Threshold Applications

## Introduction

Oxide coatings for optical applications such as high-intensity laser systems must meet stringent specifications of long-lasting optical stability and high laser-damage resistance. Therefore, it is necessary to accurately estimate intrinsic and thermally induced stresses and mechanical properties of these coatings. Silica ( $\text{SiO}_2$ ), hafnia ( $\text{HfO}_2$ ), and alumina ( $\text{Al}_2\text{O}_3$ ) are among the most-important oxide thin-film materials for manufacturing coatings that have high laser-damage thresholds. Examples include high-reflectivity mirrors and polarizers<sup>1</sup> manufactured from multilayer dielectric (MLD) coatings consisting of  $\sim 200$ -nm-thick, alternating low- and high-refractive-index layers ( $\text{SiO}_2$  and  $\text{HfO}_2$ , respectively) coated on glass (fused silica, BK7, etc.) substrates, for a total physical thickness of  $\sim 5$  to  $8 \mu\text{m}$  (Ref. 2). The mechanical properties of the single layers of these oxide thin films with thicknesses equivalent to those used in multilayers are of specific interest to the authors. One important application of these measured values is to study the failure of thin films in a multilayer system composed of alternating layers of silica and hafnia; this application was used in an earlier published work<sup>3</sup> that focused on understanding the fracture mechanics of a defect in optical multilayer thin-film systems when exposed to cleaning procedures. Another application is in the correct measurement and design of mechanical properties (modulus and hardness) of thin-film multilayers. In this application, it is critical to know the accurate properties for individual films that comprise these multilayers.

It is known<sup>4–6</sup> that changing the parameters of the deposition process—namely, oxygen backfill pressure, temperature, and rate of deposition—causes a change in the structural integrity of the thin film, including its porosity and microstructure. This might lead to differences in measured mechanical properties, even under the same test conditions for the same material deposited on an identical substrate. Therefore, when reporting measured mechanical properties of thin films, they should ideally be accompanied by information on deposition parameters, and the reported values should be used only as a reference under those stated deposition conditions.

In this work, nano-indentation on thin, single-layer films are tested and the measured load-displacement curves are used to simultaneously extract the elastic modulus and hardness of these films. These results may be used for more-detailed modeling via effective media theories.

## Experimental Details

Three single-layer thin films— $\text{SiO}_2$ ,  $\text{HfO}_2$ , and  $\text{Al}_2\text{O}_3$ —were grown using electron-beam deposition (EBD), while  $\text{Nb}_2\text{O}_5$  was grown using plasma-ion-assisted electron-beam deposition (PIAD). All depositions were performed in vacuum using the 54-in. coating system shown in Fig. 142.12. Hafnium metal was evaporated from a six-pocket electron-beam gun and oxidized as it condensed at the substrate surface by back-filling the vacuum chamber with oxygen gas to a pressure of  $8.0 \times 10^{-5}$  Torr. Alumina was also deposited from the six-pocket electron-beam source, while silica was deposited from a continuously rotating pan-type electron-beam gun. Niobia was grown by evaporating niobium metal (99.99% pure) as the source material using a single plasma source to energetically assist the electron-beam-deposition process. Using a plasma

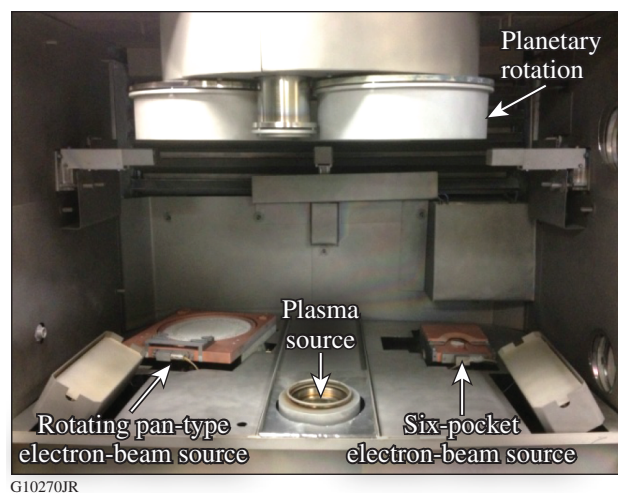


Figure 142.12  
The 54-in. vacuum chamber used to deposit the reported single-layer thin films.

source ensures the complete oxidation of the film, which is otherwise not possible with regular EBD and also allows for a more-energetic process, leading to increased densification of the thin film.<sup>7</sup> The substrate temperature was maintained at 140°C for depositing all films except niobia for which the substrate temperature was 130°C (the authors have established that these were the optimized growth parameters). Deposition was performed on five 25.4-mm-diam × 0.25-mm-thick fused-silica substrates placed in the planetary rotation system for each material deposition. Only one sample of each type of coating was used to perform the nano-indentation experiments. The thicknesses of the deposited single layers along with the process parameters are summarized in Table 142.I. Thicknesses of the films being deposited were monitored and controlled inside the coating chamber using a three-quartz-crystal monitoring setup.

All indentation experiments on these single-layer thin films were performed on the MTS Nano Instruments Nano-indenter XP. The system was fitted with a Berkovitch tip, which is a three-sided, pyramidal diamond tip (face angle ~65.03°), and the tip area's function was calibrated by performing nano-indentation on fused silica. This study focused on measuring the hardness and elastic modulus of the single-layer coatings via the Oliver–Pharr method.<sup>8</sup> Typical loads varied from 0.15 to 1.5 mN, and data were obtained for penetration depths amounting up to ~50% of individual film thicknesses. Eight to twelve indents were performed on one sample of each of the single-layer thin films.

The empirical observation,<sup>9</sup> which states that for the reliable measurement of mechanical properties it is necessary that the obtained nano-indentation data have minimal or, if possible, no “substrate effect,” was followed to report near-surface values of elastic modulus and hardness. This implies that the maximum depth of penetration of the indenter tip into the thin film, when making such measurements, should not be more than 10% to 15% of the total film thickness, especially when calculating

the hardness value. Given the significantly small thicknesses (<200 nm) of SiO<sub>2</sub>, HfO<sub>2</sub>, and Al<sub>2</sub>O<sub>3</sub>, various loads ranging from 0.15 to 15 mN were used to generate results for penetration depths varying from 10% to 50% of the total single-layer thickness. On the other hand, Nb<sub>2</sub>O<sub>5</sub> was a slightly thicker film (500 nm) and loads of 0.2 to 15 mN were required to probe 5% to 70% of the total film thickness. Indents were spaced ~100 to 150 μm apart to prevent any overlap.

## Results and Discussions

The cross sections of the films used for testing are shown using scanning electron microscopy (SEM) in Fig. 142.13. It is noteworthy that the interface of the silica film on the silica substrate cannot be seen because of the chemical homogeneity of the film and substrate.

Figure 142.14 shows the load-displacement curves for all measurements, which indicate that there were no anomalies such as “pop-in” events observed in the measurement of the

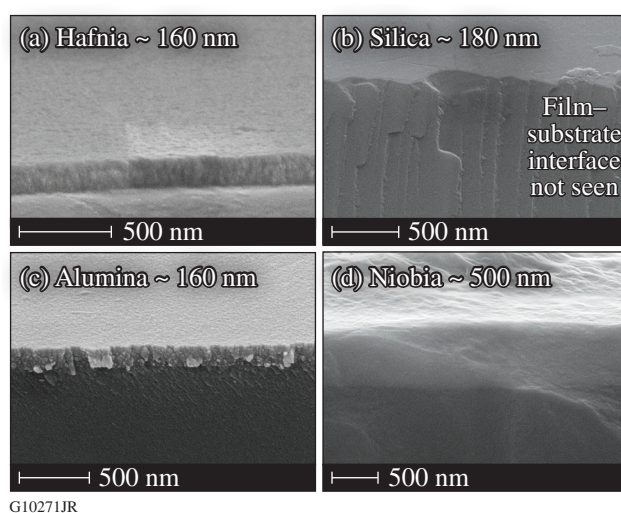
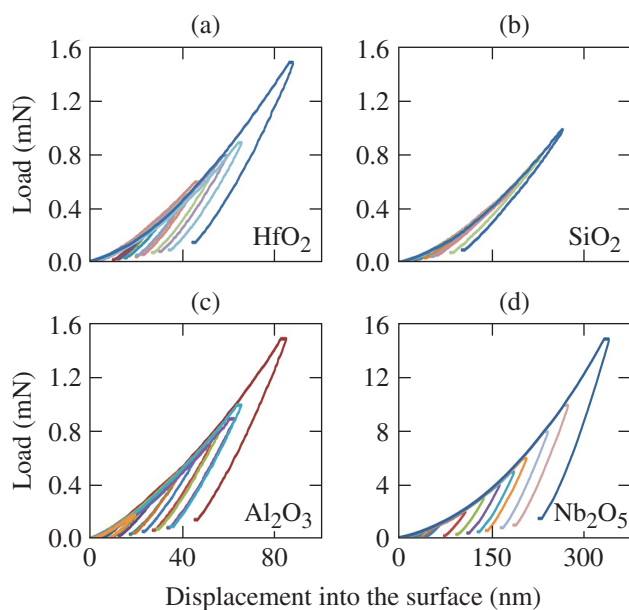


Figure 142.13  
Scanning electron microscope (SEM) images of the thin films used in this study.

Table 142.I: Process parameters for electron-beam deposition (including plasma-assist deposition) of single-layer coatings.

Material	Thickness (nm)	Deposition rate (nm/s); Temperature (°C)	Oxygen backfill pressure (Torr)	Electron-beam voltage (keV)
Hafnia	160	0.15; 140	$8 \times 10^{-5}$	7.5
Silica	180	0.46; 140	not used	6.0
Alumina	160	0.20; 140	$8 \times 10^{-5}$	7.5
Niobia*	500	0.12; 130	not used	6.0

\*55.0 standard cubic centimeters (sccm) of O<sub>2</sub> were used as a process gas for reactive deposition above the plasma chamber to increase both the reactivity of the plasma and the oxidation of the film.



G10273JR

Figure 142.14

Load-displacement curves for the four single-layer thin films tested show the different maximum loads and penetration. It should be noted that the abscissae for (a) and (b) are identical to that for (c).

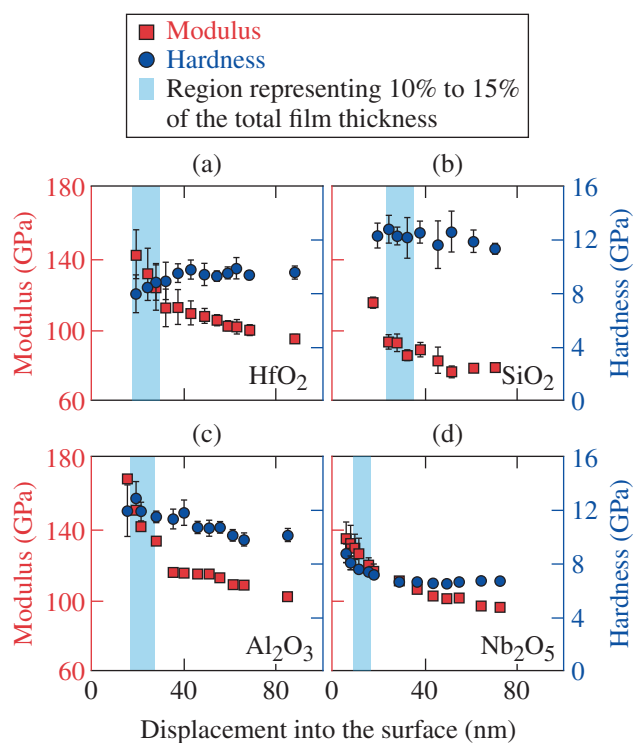
above-reported values and that the tests were, therefore, reliable for reporting the near-surface mechanical properties. Once these data are generated, the elastic modulus and hardness can be reported as a range over the  $\sim 10\%$  to  $15\%$  of the film thickness tested (shown in Fig. 142.15).

Based on the above results, elastic modulus and hardness corresponding to nano-indentation penetration depths of  $\sim 10\%$  to  $15\%$  are reported in Table 142.II. It is noted that these measured values are specifically for the deposition conditions mentioned earlier in the study.

To put these values in perspective and to see how they compare against each other, the extracted mechanical properties of each of the tested films were plotted as the elastic modulus

Table 142.II: Extracted near-surface mechanical properties corresponding to penetration depths of  $\sim 10\%$  to  $15\%$  of the total film thickness.

Single-layer thin film	Elastic modulus (GPa)	Hardness (GPa)
Hafnia	$128 \pm 12$	$8.7 \pm 0.4$
Silica	$93 \pm 5$	$12.3 \pm 0.3$
Alumina	$148 \pm 17$	$12.1 \pm 0.6$
Niobia	$130 \pm 4$	$8.1 \pm 0.5$



G10272JR

Figure 142.15

Measured near-surface values of elastic modulus and hardness for the four single-layer coatings. To generate these data, 8 to 12 indents were performed on one sample of each coating type. The blue band indicates the region of interest and encompasses the values measured for  $\sim 10\%$  to  $15\%$  of the total film thickness for each single layer, respectively. It should be noted that the abscissae for (a) and (b) are identical to those of (c) and (d).

[Fig. 142.16(a)] and hardness [Fig. 142.16(b)]. Alumina has the highest modulus and hardness, which can probably be attributed to the relatively dense film structure without the presence of micro-columnar pores indicated by the fact that these films exhibit tensile stresses while allowing for very slow water-diffusion rates.<sup>10,11</sup> Silica, which is also amorphous, has a high hardness (highest along with alumina) but the lowest modulus among the tested films. Hafnia, deposited using electron-beam technology, is slightly crystalline and has a porous, columnar microstructure<sup>4,12</sup> (shown in the SEM images in Fig. 142.13). It is seen that the measured nano-indentation modulus and hardness of hafnia are very similar to that of niobia. To determine the microstructure of niobia x-ray diffraction (XRD) phase scans, glancing angle scans and texture measurements were conducted on the single-layer thin film. Tests revealed that the film was mostly amorphous, but no conclusions were made about the porosity of the niobia single-layer coating.

Table 142.III compares the measured values and properties of thin films used in the present study to those of films (manu-

factured with the same materials) that are reported in literature, deposited by similar techniques, and used for similar applications such as in optical interference coatings. The measured Young's modulus of the four films used in this study, reported in Fig. 142.17 as "thin film (present study)," is compared to Young's modulus of the same four films from literature<sup>13,14</sup> and is shown as "thin film (literature)." The film values are also compared to bulk values (where data were available). The bulk value was significantly higher than that of any film of the same material (no bulk value of niobia is reported). For films deposited using conventional electron-beam deposition (hafnia, silica, and alumina), the values of modulus reported in the present study were different from the films reported in literature, even though the same growth technique was used, indicating the importance of particulars of the deposition conditions. For hafnia, this difference in modulus can be attributed to

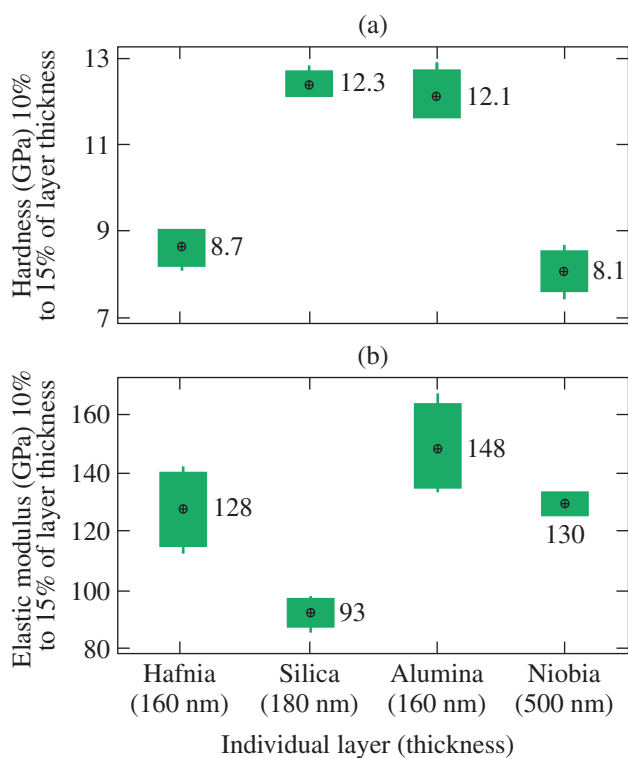
differences in the temperature to which the substrate is heated. Higher substrate temperatures used for hafnia, as reported in the literature,<sup>13</sup> are seen to be associated with films of higher stiffness and lower levels of porosity. Therefore, these films are expected to be much denser than films used in the present study, which have a more-porous microstructure from both the low kinetic energy of the atoms condensing on the substrate and the lower substrate temperatures. It is important to note that this study was not carried out to deposit films whose mechanical properties match with films reported in literature.

The films used in the present study were designed and deposited in a highly controlled way to maximize their laser-damage resistance.<sup>1</sup> The modulus reported in literature for thin-film silica is ~25% lower than what was measured in this study. This result is in contradiction to what one would expect based on the

Table 142.III: Comparison of thin films used in the present study to bulk and film properties reported in the literature.

Sample	Type	Thickness (nm)	Young's modulus (GPa)	Measurement method	Important deposition condition(s); known film properties
Hafnia <sup>13</sup>	Bulk	—	~300*	EMA/EFA-slope ( $d\sigma/dT$ )	—
Hafnia <sup>13</sup>	Thin film (e-beam)	86	~200*	EMA/EFA-slope ( $d\sigma/dT$ )	Substrate temperature 300°C; monoclinic; packing density 0.86 (porosity 0.14)
Hafnia	Thin film (e-beam)	160	128	Present study—nano-indentation	Substrate temperature 140°C; slightly monoclinic with crystallite size ~10 nm; suspected high porosity suggested from SEM images
Silica <sup>13</sup>	Bulk	—	72	EMA/EFA-slope ( $d\sigma/dT$ )	n/a
Silica <sup>13</sup>	Thin film (e-beam)	60	72	EMA/EFA-slope ( $d\sigma/dT$ )	Substrate temperature 300°C; amorphous
Silica	Thin film (e-beam)	180	93	Present study—nano-indentation	Substrate temperature 140°C; amorphous; porous
Alumina <sup>13</sup>	Bulk	—	~400*	EMA/EFA-slope ( $d\sigma/dT$ )	Polycrystalline
Alumina <sup>13</sup>	Thin film (e-beam)	55	~70*	EMA/EFA-slope ( $d\sigma/dT$ )	Amorphous
Alumina	Thin film (e-beam)	160	148	Present study—nano-indentation	Not determined
Niobia	Bulk	—	—	—	—
Niobia <sup>14</sup>	Thin film (PECVD)	550	130	Szymanowski <i>et al.</i> <sup>14</sup> —nano-indentation	100 to 200 sccm of O <sub>2</sub> ; amorphous; H ~ 10 GPa
Niobia	Thin film (PIAD)	500	130	Present study—nano-indentation	55 sccm of O <sub>2</sub> ; amorphous; H ~ 8 GPa; substrate temperature 130°C

\*Indicates that for these materials, biaxial modulus was converted to Young's modulus (using Poisson ratio values<sup>7</sup>) for the purpose of comparison for this study. PEVCD: plasma-enhanced chemical vapor deposition; PIAD: plasma-ion-assisted deposition; EMA/EFA: effective medium approximation/effective field approximation.



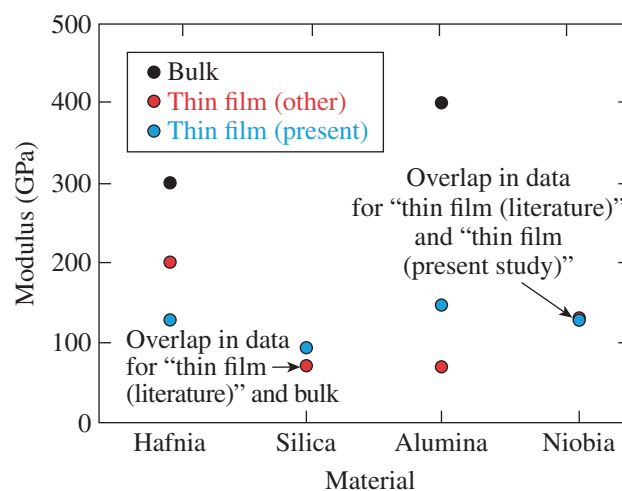
G10274JR

Figure 142.16

(a) Hardness corresponding to penetration depths approximately equal to 10% to 15% of the total film thickness. The data labels on the plots represent the mean of the measured values. (b) Elastic modulus corresponding to penetration depths approximately equal to ~10% to 15% of the total film thickness. The data labels on the plots represent the mean of the measured values.

higher substrate temperatures alone that were used in the study reported in the literature.<sup>13</sup> This clearly indicates that other factors such as deposition rates (shown in Table 142.I for the present study), geometry and size of the coating chamber (54-in. chamber for the present study),<sup>15</sup> and the angle of incidence of coating vapors on the substrate<sup>15</sup> (unknown currently) are also extremely important. It has been shown in literature<sup>16,17</sup> that the thin-film density has a linearly decreasing relationship with the tangent of the incident angle of the evaporant flux, thereby indicating that porosity or void content of the film is increasing. Therefore, the combined effect of these parameters and the way they are controlled will govern the film structure (density and porosity) and, consequently, its mechanical properties.

It is interesting to observe that, even for similar film thicknesses, our data via nano-indentation (present study) yield significantly different elastic modulus values compared to the approach via effective medium approximation. These differences are shown in Fig. 142.17. This suggests that the various coating parameters such as size of the vacuum chamber, depo-



G10275JR

Figure 142.17

Modulus values for the different materials reported in this study in bulk and thin-film forms. No bulk value of niobia is reported.

sition rates used, substrate temperature, as well as deposition angle, might be responsible for this difference. Interestingly, plasma-assist-deposited niobia films (literature and present study) have identical values of modulus (and similar hardness values), even though different amounts of process gas ( $O_2$ ) were used to deposit the respective films. In this case, we surmise that the deposition technique was the dominating factor and changing one of the process parameters had no significant impact on the measured mechanical properties of this thin film.

As an example of this approach, we demonstrate how the properties of single-layer thin film may be used to analyze multilayer dielectric (MLD) thin films used for high-laser-damage-threshold applications. We will select a hafnia-silica multilayer thin-film system, merely as an example, to show how individual thin-film properties (elastic modulus  $E$ ) can be used to predict the shear modulus  $\mu$  and bulk modulus  $B$  for the multilayer thin film using the relations  $\mu = E/2(1 + \nu)$  and  $B = E/3(1 - 2\nu)$ . In this case the volume fractions of hafnia and silica in the multilayer thin-film system are 0.39 and 0.61, respectively. The upper and lower limits on shear modulus and bulk modulus were calculated by the rule of mixtures:

$$(\mu_{\text{MLD}})^{\text{upper}} = \mu_{\text{hafnia}} V_{\text{hafnia}} + \mu_{\text{silica}} V_{\text{silica}},$$

$$(B_{\text{MLD}})^{\text{upper}} = B_{\text{hafnia}} V_{\text{hafnia}} + B_{\text{silica}} V_{\text{silica}},$$

and

$$1/(\mu_{\text{MLD}})^{\text{lower}} = (V_{\text{hafnia}}/\mu_{\text{hafnia}}) + (V_{\text{silica}}/\mu_{\text{silica}}),$$

$$1/(B_{\text{MLD}})^{\text{lower}} = (V_{\text{hafnia}}/B_{\text{hafnia}}) + (V_{\text{silica}}/B_{\text{silica}}),$$

where  $V_{\text{hafnia}}$  and  $V_{\text{silica}}$  are the volume fractions of hafnia and silica. The lower and upper limits on bulk modulus were calculated to be 58.4 GPa and 63.5 GPa, respectively, whereas the limits on shear modulus were found to be 44.5 GPa and 45.2 GPa, respectively. These bounds can now be averaged to estimate the bulk and shear moduli for the multilayer coating. Furthermore, Poisson ratio ( $\nu$ ) and Young's modulus ( $E$ ) for the multilayer coating can also be calculated using the relations  $\nu = (3B - 2\mu)/(6B + 2\mu)$ ,  $E = 2\mu(1 + \nu)$ . In this example, these values work out to be  $\nu_{\text{MLD}} = 0.20$  and  $E_{\text{MLD}} = 108$  GPa. Such material properties can then be used to interpret the underlying fracture mechanics of these multilayer thin-film systems.<sup>3</sup>

### Conclusions

A nano-indentation study was performed on four single-layer thin films used in high-power laser systems to understand their mechanical properties, specifically hardness and Young's modulus. Alumina and silica demonstrate the highest values of hardness and are approximately equal to 12 GPa. The highest value of elastic modulus was also shown by alumina approximately equal to 148 GPa. These measured values were compared to properties reported in the literature for films used in similar applications and grown by identical techniques, but under varying deposition conditions. It is shown that the properties of the film are directly related to not only the deposition techniques, but also the deposition factors, such as substrate temperature, deposition rates, and amount of oxygen used for back-fill and even the geometry and size of the coating chamber. These factors can be controlled to produce thin films for very specific applications such as coatings with high laser-damage thresholds, but changing these parameters can significantly change the film's density and porosity (or the microstructure of the film) and therefore directly affect the hardness and modulus measurements.

It has also been concluded that accurate and reliable measurements of single-layer films are important to understanding the fracture mechanics and failure mechanisms of multilayer thin-film systems manufactured from the same materials. Such properties could also be useful as guidelines in designing multilayers of specified hardness and modulus by controlling the thicknesses and properties of the single-layer thin films.

### ACKNOWLEDGMENT

The authors express their appreciation to the University of Rochester's Laboratory for Laser Energetics (LLE) for continuing support. K. Mehrotra is supported by an LLE Horton Fellowship. The authors also thank Dr. Stephen D. Jacobs for useful discussions and his valuable feedback. This material is

based upon work supported by the Department of Energy National Nuclear Security Administration under Award Number DE-NA0001944, the University of Rochester, and the New York State Energy Research and Development Authority. The support of DOE does not constitute an endorsement by DOE of the views expressed in this article.

### REFERENCES

1. J. B. Oliver, A. L. Rigatti, J. D. Howe, J. Keck, J. Szczepanski, A. W. Schmid, S. Papernov, A. Kozlov, and T. Z. Kosc, in *Laser-Induced Damage in Optical Materials: 2005*, edited by G. J. Exarhos *et al.* (SPIE, Bellingham, WA, 2005), Vol. 5991, Paper 599119.
2. K. Mehrotra, H. P. Howard, S. D. Jacobs, and J. C. Lambropoulos, in *Nanocomposites, Nanostructures and Heterostructures of Correlated Oxide Systems*, edited by T. Endo *et al.*, Mat. Res. Soc. Symp. Proc. Vol. 1454 (Cambridge University Press, Cambridge, England, 2012), pp. 215–220.
3. H. P. H. Liddell, K. Mehrotra, J. C. Lambropoulos, and S. D. Jacobs, *Appl. Opt.* **52**, 7689 (2013).
4. H. Leplan *et al.*, *J. Appl. Phys.* **78**, 962 (1995).
5. R. Thielsch, A. Gatto, and N. Kaiser, *Appl. Opt.* **41**, 3211 (2002).
6. J. E. Klemberg-Sapieha *et al.*, *Appl. Opt.* **43**, 2670 (2004).
7. J. B. Oliver, P. Kupinski, A. L. Rigatti, A. W. Schmid, J. C. Lambropoulos, S. Papernov, A. Kozlov, J. Spaulding, D. Sadowski, Z. R. Chrzan, R. D. Hand, D. R. Gibson, I. Brinkley, and F. Placido, *Appl. Opt.* **50**, C19 (2011).
8. W. C. Oliver and G. M. Pharr, *J. Mater. Res.* **7**, 1564 (1992).
9. J. L. Hay, M. E. O'Herna, and W. C. Olivera, in *Symposium T—Fundamentals of Nanoindentation & Nanotribology*, edited by N. R. Moody *et al.*, Mat. Res. Soc. Symp. Proc. Vol. 522 (Materials Research Society, Warrendale, PA, 1998), p. 27.
10. R. Thielsch *et al.*, *Thin Solid Films* **410**, 86 (2002).
11. J. B. Oliver, P. Kupinski, A. L. Rigatti, A. W. Schmid, J. C. Lambropoulos, S. Papernov, A. Kozlov, C. Smith, and R. D. Hand, *Opt. Express* **20**, 16,596 (2012).
12. J. B. Oliver, S. Papernov, A. W. Schmid, and J. C. Lambropoulos, in *Laser-Induced Damage in Optical Materials: 2008*, edited by G. J. Exarhos *et al.* (SPIE, Bellingham, WA, 2008), Vol. 7132, Paper 71320J.
13. R. Thielsch and N. Kaiser, in *Optical Interference Coatings*, OSA Technical Digest Series (Optical Society of America, Banff, Canada, 2001), Paper ThB6.
14. H. Szymanowski *et al.*, *J. Vac. Sci. Technol. A* **23**, 241 (2005).
15. J. B. Oliver, "Evaporated HfO<sub>2</sub>/SiO<sub>2</sub> Optical Coatings and Modifications for High-Power Laser Applications," Ph.D. thesis, University of Rochester, 2012.
16. Y. D. Fan *et al.*, *Phys. Status Solidi A* **134**, 157 (1992).
17. M. J. Brett, *J. Mater. Sci.* **24**, 623 (1989).

---

# Thermal Fluctuations in Superconductor/Ferromagnet Nanostripes

## Introduction

The problem of fluctuations in two-dimensional (2-D) superconducting stripes with a thickness  $d$  that is much smaller than the London penetration depth  $\lambda$  and a width  $w$  that is much smaller than the Pearl length  $\Lambda = 2\lambda^2/d \gg w$  has been extensively discussed in the context of the Berezinsky–Kosterlitz–Thouless (BKT) transition.<sup>1,2</sup> The interest in this topic was revived recently<sup>3,4</sup> to try to better understand the physics of the operation of superconducting single-photon detectors (SSPD's) consisting of nanostripes that are densely packed into a meander-type geometry. The first SSPD's introduced in 2001 (Ref. 5) have since received great attention because of their excellent performance as ultrafast, highly efficient counters for both infrared and visible light photons and are now regarded as the devices of choice in such high-performance applications such as quantum optics and quantum communications.<sup>6,7</sup> The SSPD basic model of operation principle is based on a supercurrent-to-resistive-state transition of a 2-D nanostripe maintained at a temperature far below the critical temperature  $T_c$  and biased sufficiently close to its critical current  $I_c$ . The energy of one or several optical photons absorbed in the nanostripe is sufficient to trigger the transition, producing a transient resistive state and resulting in a detection event.

Independent of the photon counts described above and even when completely isolated from any external light, the SSPD spontaneously generates (especially at higher operating temperatures and with the bias close to  $I_c$ ) transient voltage pulses. Fully understanding the nature of dark counts, i.e., the physical mechanism of these fluctuation events, is very relevant for optimizing the counting performance of SSPD's (minimization of their dark counts). In addition, the dark-count phenomenon has its own basic physics interest in relation to dissipation and thermal fluctuation effects occurring in superconducting 2-D nanostripes and 1-D (one-dimensional) nanowires.

The present literature on dark counts in SSPD's focuses exclusively on NbN-based devices<sup>3,4,8,9</sup> and most recently favors the explanation that assigns the most-relevant role to magnetic vortices moving across the width of a superconducting stripe, either as

vortex–antivortex pairs (VAP's) or as single vortices overcoming the barrier at opposite edges of the stripe—a mechanism called vortex hopping (VH). In other proposals, relevant mechanisms consider thermal fluctuations of the number of excitations<sup>8</sup> or spontaneous nucleation of normal-state regions across the stripe in analogy with  $2\pi$ -phase slip centers existing in 1-D wires,<sup>10,11</sup> but the latter process is typically discarded because its occurrence has a low probability in 2-D superconducting nanostripes, typically implemented in practical SSPD's.

Besides NbN, a number of superconducting materials have been proposed and successfully implemented for SSPD applications: for example, WSi and MoSi<sup>12,13</sup> or hybrid superconductor/ferromagnet (S/F) bilayers.<sup>14</sup> Therefore, it is important to note that the composition and morphology of different materials may lead to significant variations in fluctuation mechanisms. In this respect, the investigation of S/F bilayers is of particular interest because, as we have already demonstrated elsewhere,<sup>14–16</sup> the presence of a weak ferromagnetic overlayer significantly influences both the superconducting and optical properties of the S/F nanostripes. In fully proximitized, hybrid S/F nanostructures, such as NbN/NiCu, vortex pinning effects are certainly of relevance, leading, e.g., to the  $J_c$  enhancement.<sup>14</sup> At the same time, even an epitaxial-quality S/F interface leads to a significant change in the electron non-equilibrium relaxation dynamics observed in photoresponse experiments.<sup>15,16</sup> Consequently, the S/F systems constitute a great test bed for investigating the role of magnetic vortices in fluctuation phenomena in 2-D superconducting nanostripes and can provide a direct comparison between various models that have been proposed in the literature. The latter is greatly facilitated by the fact that all test structures, as well as the pure-S reference samples, can be processed in the same fabrication run and tested under exactly the same conditions. Finally, besides their unquestionable role in dark counts, vortices have also been implicated as a possible reason for the appearance of photon counts in SSPD's, at least as a supplementary detection mechanism.<sup>17,18</sup> They are, in fact, likely to play a key role in the nonequilibrium photoresponse mechanism of high-temperature superconducting photodetectors.<sup>19</sup>

In this work, the effects of thermal fluctuations in superconducting hybrid S/F nanostructures are investigated and compared with those observed in pure-S nanostructures. The hybrid S/F samples are 5- $\mu\text{m}$ -long, 175-nm-wide nanostructures that consist of an 8-nm-thick NbN film covered with a 6-nm-thick NiCu, weak ferromagnet overlayer, while the reference samples are 5- $\mu\text{m}$ -long, 100-nm-wide, 8-nm-thick NbN, pure-S nanostructures. The experimental dependences of the fluctuation rates as functions of bias current and temperature are presented and discussed in the framework of both the VAP and VH theoretical models. Arguments are provided for why other possible fluctuation mechanisms are excluded and, instead, focused only on the VAP and VH scenarios. Most importantly, the studies, as suggested by Bartlof *et al.*,<sup>3</sup> made it possible to differentiate between the VAP and VH models.

The following sections will (1) describe the sample fabrication and characterization and present time-resolved dark- and photon-count waveforms and measurements of the thermal fluctuation rates versus the bias current and temperature; (2) outline the main features of both the VAP and VH theoretical models, which were then used to interpret the experimental data; and (3) present conclusions and future outlook.

### Experimental Details and Results

The base of superconducting nanostructures tested in this work was 8-nm-thick NbN film grown on MgO substrates by reactive dc-magnetron sputtering in an Ar/N<sub>2</sub> gas mixture under general sputtering conditions reported elsewhere.<sup>14–16</sup> For S/F structures, a NiCu overlayer was deposited in the same system, without breaking vacuum, by a dc magnetron in pure Ar equipped with a Ni<sub>0.39</sub>Cu<sub>0.61</sub> target at a 155-W deposition power and a rate of 60 nm/min, respectively. Magnetic moment tests demonstrated that our NiCu overlayers were ferromagnetic with a Curie temperature of  $\sim 20$  K. All tested nanostructures were patterned by electron-beam lithography, followed by reactive-ion etching. Gold contacts were defined by conventional photolithography and the lift-off method. For thermal fluctuation measurements, 5- $\mu\text{m}$ -long straight nanostructures were used with a width of 175 nm and 100 nm for NbN/NiCu and NbN, respectively. The NbN stripes exhibited  $T_c = 12.1 \pm 0.2$  K, while the  $T_c$  values of the NbN/NiCu samples were suppressed by less than 0.5 K.

From current–voltage (I–V) characteristic measurements of the nanostructures, performed at different temperatures, critical-current-density dependences were obtained for  $J_c^{\text{NbN/NiCu}}(T)$  and  $J_c^{\text{NbN}}(T)$ , for NbN/NiCu and NbN nanostructures, respectively. In agreement with the authors' previously published

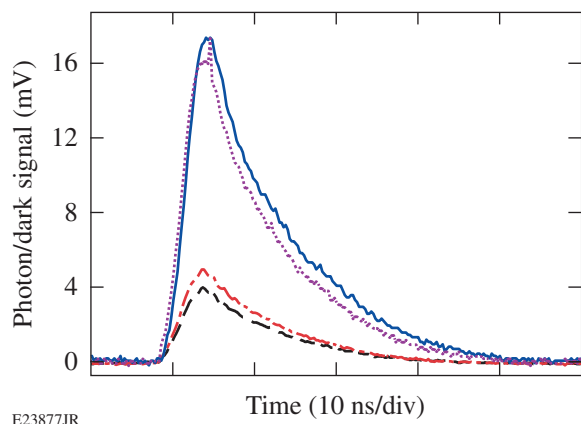
experiments,<sup>14</sup>  $J_c$ 's for NbN/NiCu nanostructures were significantly enhanced as compared to those of NbN and, for example, at 4.2 K,  $J_c^{\text{NbN/NiCu}} = 43.2$  MA/cm<sup>2</sup>, while  $J_c^{\text{NbN}} = 11.6$  MA/cm<sup>2</sup>. The  $J_c$  enhancement in the S/F bilayer was explained in Ref. 14 as the impact of scalar magnetic impurities<sup>20</sup> that generate extra flux pinning in fully proximitized S/F film.

To measure the dark-count rate, the samples were mounted on a cryogenic insert and placed them inside a liquid-helium transport Dewar. The sample holder was surrounded by a metallic enclosure that completely shielded the test structure from outside radiation. The sample temperature was controlled by varying the helium vapor pressure and position of the insert inside the Dewar and was measured with a calibrated germanium thermometer. The dark-count events were registered as voltage-fluctuation transients and readout using a cascade of two microwave amplifiers with an effective bandwidth of 0.1 to 100 MHz and a total gain of 20 dB. The amplified signals were fed by a 50- $\Omega$  coaxial cable into readout electronics, which consisted of either a digital oscilloscope with a 1-GHz bandwidth or a pulse counter with a 100-MHz bandwidth.

As a reference, the measured photon counts were obtained by illuminating the same nanostructures with 6.25-ns-wide, 1550-nm-wavelength laser pulses, generated by a laser diode with a repetition rate of 80 MHz. The laser-spot diameter was  $\sim 50$   $\mu\text{m}$ , much larger than the size of the nanostructure, ensuring a uniform optical illumination. The latter tests were done in a continuous-flow helium cryostat with an optical window.

Figure 142.18 presents examples of time-resolved waveforms of dark and photon counts, measured at  $T = 4.9$  K, for both NbN/NiCu and NbN nanostructures biased at the same value of a normalized bias current, namely  $I_b/I_c = 0.8$ . Note that for each nanostructure, the dark- and photon-count pulses practically overlap since in both cases the transient voltage signals reflect the resistive state of a nanostructure. Actually, all four waveforms in Fig. 142.18 have the identical shape with a detection-system–limited rise time and an  $\sim 20$ -ns-long fall time. The difference in the amplitude between the NbN/NiCu and NbN signals (the S/F sample exhibits a significantly larger amplitude) is a result of the earlier-mentioned difference in their respective  $J_c$ 's; in fact, the amplitude ratio is very close to the  $J_c^{\text{NbN/NiCu}}/J_c^{\text{NbN}}$  ratio.

Figure 142.19 presents thermal fluctuation or dark-count rates of NbN (black squares) and NbN/NiCu (red circles) nanostructures as functions of  $I_b/I_c$  at temperatures 4.5, 6.0, and 8.0 K, collected using a pulse counter. For both nanostructures, the fluctuation



E23877JR

Figure 142.18

Photon- and dark-count pulses of NbN (red and black lines, respectively) and NbN/NiCu (magenta and blue lines, respectively) nanostructures. All pulses were recorded under the same conditions, namely,  $I_b/I_c = 0.8$  and  $T = 4.9$  K. For photon illumination, we used pulsed laser illumination with a 1550-nm wavelength.

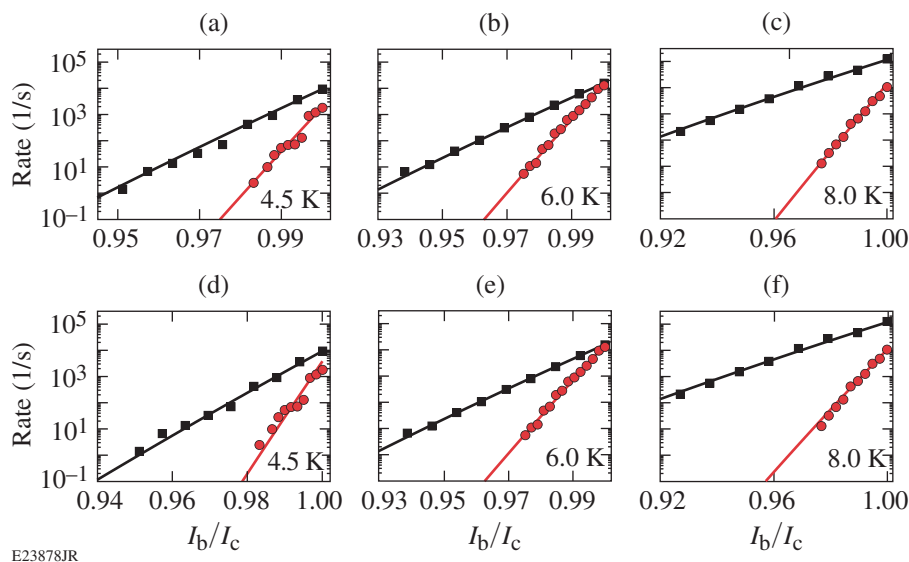
rates were observed to decrease exponentially over four orders of magnitude. The S/F sample is, however, much more stable against fluctuations, exhibiting significantly lower dark counts at each temperature. In all panels in Fig. 142.19, the  $I_b/I_c$  range of the measurements was limited by the 1-Hz accuracy of the counter. Finally, it is stressed that the experimental data (black squares and red circles) presented in Figs. 142.19(a)–142.19(c) are exactly the same as those in Figs. 142.19(d)–142.19(f). The

difference is that the former dataset was fitted (solid lines) using the VAP model, while the latter dataset was fitted using the VH model. The details of the fits and their physical significance are presented in the next section.

### Fluctuation Models and Discussion

In 2-D systems, both transverse dimensions ( $d$  and  $w$ ) of a superconducting stripe should be smaller than the shortest relevant scale, which in this case is given by the Ginzburg–Landau coherence length  $\xi$ . Literature<sup>3,9</sup> values of  $\xi_0$ , the coherence length at  $T = 0$ , for NbN are of the order of a few nanometers, and from superconducting fluctuation measurements,<sup>21</sup> it is expected that  $\xi_0$  for NbN/NiCu should be even slightly shorter. Therefore, it can be assumed that the nanostructures fall into the 2-D category. Moreover, the Likharev condition  $w \geq 4.4\xi$  is always satisfied, ensuring that the stripes are wide enough to nucleate their propagation of vortices. Finally,  $\Lambda \gg w$ ; therefore, the current-density distribution can be assumed to be homogeneous across the film widths.

Various mechanisms are able to produce dark counts and could be considered as responsible for the fluctuation rates measured in these experiments. They can be summarized as (1) thermal unbinding of VAP's; (2) thermal or quantum mechanism of VH; (3) fluctuations of the number of quasiparticles; and (4) thermal or quantum phase-slip center processes. Following the arguments given in Ref. 3, based on a comparison



E23878JR

Figure 142.19

Measured fluctuation rates versus normalized bias current of NbN (black squares) and NbN/NiCu (red circles) nanostructures, measured at 4.5, 6.0, and 8.0 K. The solid lines are the best fits obtained using the [(a)–(c)] VAP model and the [(d)–(f)] VH model.

of the amplitudes of the excitation energy barriers, it can be concluded that the probability of an occurrence of phase-slip centers is very low, so it can be ignored in this process. Next, following a theoretical approach presented in Ref. 8, the dark-count rate related to the fluctuation in the number of quasi-particles is calculated, but any attempt to fit the data with this model failed, in particular for the S/F sample. Finally, since the temperature interval investigated in this work is 4.5 to 8.0 K, fluctuation mechanisms caused by quantum tunneling of vortices through the edge barrier can be excluded because they become relevant only at sub-Kelvin temperatures.<sup>11</sup>

Based on the above, discussion is limited to the thermal regime and consider only the VAP and VH fluctuation scenarios:

- (1) VAP: unbinding of vortex–antivortex pairs and their movement across the nanostripe to its opposite edges resulting from the Lorentz force;
- (2) VH: thermal excitation of a single vortex near the edge of the stripe and a consecutive dissipative movement across it.

In both models, thermal fluctuations must overcome an excitation energy barrier  $U(I_b, T)$  and the corresponding fluctuation, or, equivalently, the dark-count rate may be expressed as

$$\Gamma(I_b, T) = \Omega \exp\left[-U(I_b, T)/k_B T\right], \quad (1)$$

where  $\Omega$  is the attempt frequency. The actual expressions for  $U(I_b, T)$ , as well as the fit values of  $\Omega$ , will, of course, be different in these two types of mechanisms.

### 1. Unbinding of Vortex–Antivortex Pairs

In 2-D systems, the collapse of a long-range order gives rise to so-called topological defects in the order parameter that, in thin superconducting films, excite pairs of vortices, according to the BKT model. At temperatures below the BKT transition, these pairs consist of single vortices with their respective supercurrents circulating in opposite directions and result in a bound VAP state. Under the  $w \geq 4.4\xi$  condition, a BKT phase transition can occur only if the energy of a bound VAP depends logarithmically on the separation distance of the vortex core centers  $r$  ( $r \ll \Lambda$ ). Under a transport current condition, however, a Lorentz force is exerted on VAP's and directed in opposite directions for the vortex and the antivortex, respectively. The resulting torque forces VAP's to align perpendicularly to the current flow. The binding energy changes with the angle and reaches its minimum at  $\pi/2$ . As was shown by Mooji,<sup>22</sup> the interplay between repulsion of vortices in a pair resulting

from the Lorentz force and their magnetic attraction defines the current-dependent  $r = 2.6\xi I_c / I_b$ , leading to the minimal binding energy of the pair,  $U_{\text{VAP}}$  (Ref. 3).

This binding energy may be overcome by thermal excitations with a probability equal to the Boltzmann's factor  $\exp(-U_{\text{VAP}}/k_B T)$ . In the absence of pinning, thermally unbound vortices will move freely toward opposite edges of the strip, where they leave the structure or rather annihilate with an oppositely orientated vortex. The moving vortices dissipate energy, initiating creation of a nonsuperconducting domain. In current-biased ( $I_b < I_c$ ) stripes, the appearance of such domains results in voltage transients that are then registered as dark-count events. According to the model in Refs. 3 and 8, the dark-count rate follows Eq. (1) with the  $U_{\text{VAP}}$  given by

$$U_{\text{VAP}} = \frac{A(T)}{\varepsilon} \left[ \ln\left(\frac{2.6I_c}{I_b}\right) - 1 + \frac{I_b}{2.6I_c(T)} \right], \quad (2)$$

where  $A(T)$  is the vortex interaction constant and  $\varepsilon$  is the averaged polarizability of a VAP within the entire VAP population.<sup>3,22</sup>

The solid lines in Figs. 142.19(a)–142.19(c) present the fits of the fluctuation rates for both NbN and NbN/NiCu samples based on Eqs. (1) and (2) at three different temperatures. The values of the fitting parameters,  $A(T)$  and  $\varepsilon$ , are reported in Table 142.IV (Ref. 23). We note that the fits are in agreement with the experimental data and the  $A(T)$  and  $\varepsilon$  values are reasonably close to those reported in the literature.<sup>3</sup> Interestingly, the  $A$  parameter for the NbN/NiCu sample has a value about three times greater than that for the NbN sample, indicating that the binding energy of the VAP in this case is significantly stronger than in the pure NbN. The latter explains the dramatically lower (over an order of magnitude) fluctuation rates for the NbN/NiCu nanostripe, as compared to NbN. The presence of a weak ferromagnetic NiCu layer also leads to an increase of  $\varepsilon$ , providing clear evidence that pinning is enhanced in the S/F sample.

### 2. Vortices Overcoming the Edge Barrier

The experimental data is analyzed in a framework of the motion of single unbounded vortices.<sup>3,4</sup> At bias currents close to the de-pairing  $I_c$ , the magnetic self-field at the stripe edges is much larger than the critical field for vortex entry. The entry of vortices at one edge of the stripe and antivortices at the opposite edge is prohibited by an edge barrier very similar to the Bean–Livingston surface barrier.<sup>3,24</sup> Consequently, the corresponding probability for thermally activated vortex hopping

Table 142.IV: Parameters used to fit the measured fluctuation rates within the VAP and VH models.

Samples	$T$ (K)	VAP model fitting parameters		VH model fitting parameters		Calculated parameters	
		$A$ (eV)	$\epsilon$	$\xi$ (nm)	$E_B$ (eV)	$\Lambda$ ( $\mu\text{m}$ )	$\lambda$ (nm)
NbN	4.5	0.20	1.9	4.5	0.10	34	368
	6.0	0.19	1.8	5.9	0.09	37	385
	8.0	0.16	1.8	6.9	0.08	44	420
NbN/NiCu	4.5	0.70	3.0	4.3	0.35	9.7	261
	6.0	0.66	2.5	5.0	0.34	10.3	269
	8.0	0.65	2.0	6.0	0.33	10.4	270

over this energy barrier is again proportional to the Boltzmann factor  $\exp(-U_{\text{VH}}/k_B T)$ . However,  $U_{\text{VH}}$  is now given by

$$U_{\text{VH}}(T, I_b) = E_B(T, I_b) \times \left\{ \ln \left[ \frac{2w}{\pi \xi(T)} \frac{1}{\sqrt{1 + [\Phi_0 I_b / \pi E_B(T, I_b)]}} \right] - \frac{\Phi_0 I_b}{\pi E_B(T, I_b)} \left[ \arctan \left[ \frac{\pi E_B(T, I_b)}{\Phi_0 I_b} \right] - \frac{\pi \xi(T)}{2w} \right] \right\}, \quad (3)$$

where  $E_B(I_b, T) = \Phi_0^2 / 2\pi\mu_0\Lambda(I_b, T)$  is the energy scale.<sup>3</sup>

Once a vortex jumps over the barrier, thanks to the Lorentz force, it will move across the stripe. Analogically to the VAP scenario, motion of these free vortices across the stripe creates a nonsuperconducting domain and results in a voltage transient. The resulting dark-count rate for the VH process is given by Eq. (1) with  $U_{\text{VH}}$  defined in Eq. (3).

In Figs. 142.19(d)–142.19(f), the solid lines are the fits of the experimental fluctuation rates (circles) for the NbN and NbN/NiCu samples, but this time using Eqs. (1) and (3). Note that beside the NbN/NiCu data at 4.5 K, the fits are as good as in the case of the VAP model. The  $E_B$  and  $\xi$  fitting parameters are reported in Table 142.IV (Ref. 23) next to the column representing the VAP model. First of all, a clear self-consistency of the thermal fluctuation approach is noticed, i.e.,  $E_B = A/2$ , as expected from the definition of  $E_B$ . The extracted value of  $E_B$  made it possible to calculate the parameter  $\Lambda$  and, consequently,  $\lambda$  for the samples at the three temperatures studied. The actual values are listed in a separate column in Table 142.IV; for NbN/NiCu, both  $\Lambda$  and  $\lambda$  are somewhat reduced as compared to NbN.

The  $\xi(T)$  values obtained with the fitting procedure of the VH model for both NbN and NbN/NiCu nanostripes are plotted in Figs. 142.20(a) and 142.20(b), respectively, as a function of normalized temperature  $T/T_c$ . As expected earlier, the presence of the NiCu overlayer enhances the S/F nanostripe 2-D character by reducing the  $\xi(T)$  values, as compared to the pure NbN sample. The solid lines are the best fits of these values obtained by using the following analytical expression [Eq. (3)]:

$$\xi^2(T/T_c) = \frac{\xi_0^2}{(1 - T/T_c)} \frac{1}{\sqrt{1 + T/T_c}}. \quad (4)$$

The  $\xi(T)$  values extracted from the fits carry rather large errors (especially at higher temperatures), but the agreement with Eq. (4) is still very good and makes it possible to estimate the  $\xi_0$  values as equal to 3.9 nm and 4.2 nm for the NbN/NiCu samples, respectively.

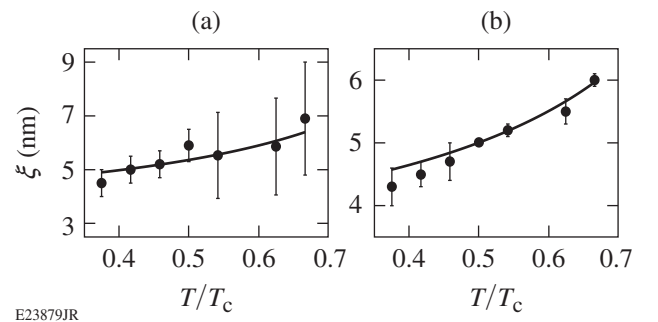


Figure 142.20

The coherence length's dependence on the normalized temperature for (a) NbN and (b) NbN/NiCu samples. The  $\xi(T)$  values (circles) were obtained by the best-fitting procedure [Eqs. (1) and (3)] to the VH model (see also Fig. 142.19). The solid lines are the best fits obtained by using Eq. (4). The extrapolated values of  $\xi_0$  are 4.2 nm and 3.9 nm for NbN and NbN/NiCu samples, respectively.

NiCu and NbN samples, respectively. The obtained  $\xi_0$  values reinforce the fact that the 2-D approximation is applicable for our nanostructures.

### 3. Discussion

A simple “visual” comparison between Figs. 142.19(a)–142.19(c) and 142.19(d)–142.19(f) does not enable the differentiation between which of the two vortex-based, thermal fluctuation scenarios best describes the physics of our experiments. Therefore, we have attempted a more-quantitative approach by plotting the values of the excitation energy in units of  $k_B$  at the fixed  $I_b/I_c = 0.99$  bias as functions of temperature. The results are plotted in Fig. 142.21. The points correspond to the  $U_{VAP}/k_B$  and  $U_{VH}/k_B$  values for both the NbN and NbN/NiCu samples (see Fig. 142.21 caption for details), and the solid lines are only guides for the eye.

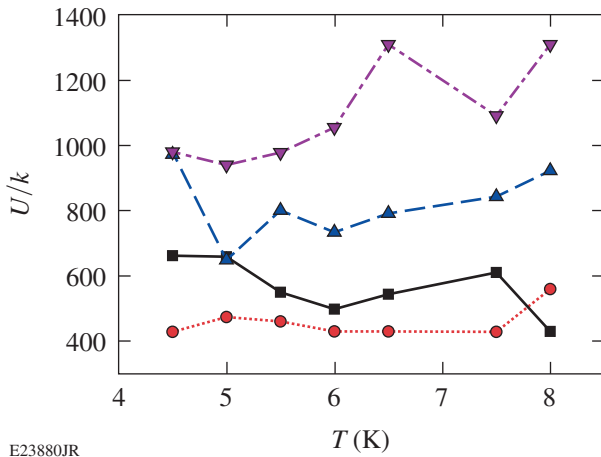


Figure 142.21

Excitation energy  $U$  in units of  $k_B$  at seven temperatures. The plotted points are the best-fit values from Fig. 142.19 at  $I_b/I_c = 0.99$ ; the corresponding symbols are magenta inverted triangles: VAP, NbN/NiCu; blue triangles: VH, NbN/NiCu; red circles: VAP, NbN; and black squares: VH, NbN. The lines are only guides for the eye.

Individual comparisons between the data corresponding to S/F and S samples within the same fluctuation model are made, as well as comparisons between the VAP and VH models for the same sample type. Within the VAP model, the data for NbN (red circles) and NbN/NiCu (magenta inverted triangles) show that the excitation energy of the pure NbN sample is always significantly smaller than that of the NbN/NiCu sample, i.e.,  $U_{VAP}^S < U_{VAP}^{S/F}$ . In addition, the same behavior (although not as dramatic) is also observed within the VH model for NbN (black squares) and NbN/NiCu (blue triangles) samples. The latter is a clear confirmation that the stronger pinning existing in the

S/F nanobilayer corresponds to the higher-energy excitation barrier and, as a consequence, leads to a significant decrease in the rate of thermal fluctuations (dark counts) observed in Fig. 142.19 for the NbN/NiCu nanostructure.

Next, the two models are compared for the same sample type, i.e., NbN/NiCu (blue triangles) with NbN/NiCu (magenta inverted triangles) and NbN (black squares) with NbN (red circles). From Fig. 142.21 it is noted that for the S/F sample, the excitation energy corresponding to the VH model (blue triangles) is always markedly lower than that of the VAP model (magenta inverted triangles), i.e.,  $U_{VH}^S < U_{VAP}^{S/F}$ . The only exception is the  $T = 4.5$ -K data point, but as previously mentioned, the VH fit in this case is uncharacteristically poor [see Fig. 142.19(d)], and can be disregarded at this point. Consequently, the presence of extra pinning in the S/F sample makes it possible to differentiate between the two mechanisms, and the VH scenario with the lower  $U_{VH}$  barrier is clearly favored for S/F samples. On the other hand, for the pure-S sample, the VH and VAP values are quite close and differentiation is difficult. However, Fig. 142.21 seems to indicate that the VAP mechanism is favored in the NbN sample, supporting earlier findings.<sup>9</sup>

### Conclusions

The fluctuation rate as a function of the applied bias current was measured at various temperatures in hybrid S/F and pure-S nanostructures and have performed the same NbN/NiCu and NbN sample measurements of the I–V characteristics and the time-resolved waveforms of both photon- and dark-count events. The NbN/NiCu samples exhibited an enhancement of  $I_c$ ; correspondingly, the amplitude increase of both the photon- and dark-count pulses were measured. The latter findings clearly indicate the role of pinning of magnetic vortices in S/F nanostructures and confirm the results obtained previously on similar samples.<sup>14</sup> The measured fluctuation rates have been analyzed in a framework of the VAP and VH theoretical models that are based on thermal activation and subsequent motion of magnetic vortices. In the fluctuation rate versus temperature experiments, the NbN/NiCu samples were significantly more stable against thermal fluctuation as compared to NbN, and for NbN/NiCu a mechanism based on thermal VH was clearly dominant. The model discrimination was less evident in the case of pure-S samples; nevertheless, the results point to the VAP mechanism as being responsible for the dark counts observed in NbN nanostructures, in agreement with earlier studies.<sup>9</sup>

For the practical application of nanostructures as SSPD’s, the detailed knowledge of the physical origin of thermal

fluctuations is important to improving the performance of superconducting detectors by controlling their dark counts. Hybridization of a pure superconducting nanostripe with a weak ferromagnetic material, as in the case of the NbN/NiCu sample, is very promising since it leads to a significant decrease in thermal fluctuations that corresponds to reduced dark counts, as well as in the increase in the photoresponse amplitude, resulting in an improved signal-to-noise ratio of the SSPD.

#### ACKNOWLEDGMENT

The authors acknowledge the European Union COST Action MP1201.

#### REFERENCES

1. Y. Liu *et al.*, Phys. Rev. Lett. **68**, 2224 (1992).
2. J. M. Repaci *et al.*, Phys. Rev. B **54**, R9674 (1996).
3. H. Bartolf *et al.*, Phys. Rev. B **81**, 024502 (2010).
4. L. N. Bulaevskii *et al.*, Phys. Rev. B **83**, 144526 (2011).
5. G. N. Gol'tsman, O. Okunev, G. Chulkova, A. Lipatov, A. Semenov, K. Smirnov, B. Voronov, A. Dzardanov, C. Williams, and R. Sobolewski, Appl. Phys. Lett. **79**, 705 (2001).
6. R. H. Hadfield, Nat. Photonics **3**, 696 (2009).
7. C. M. Natarajan, M. G. Tanner, and R. H. Hadfield, Supercond. Sci. Technol. **25**, 063001 (2012).
8. A. Engel *et al.*, Physica C **444**, 12 (2006).
9. J. Kitaygorsky, I. Komissarov, A. Jukna, D. Pan, O. Minaeva, N. Kaurova, A. Divochiy, A. Korneev, M. Tarkhov, B. Voronov, I. Milostnaya, G. Gol'tsman, and R. Sobolewski, IEEE Trans. Appl. Supercond. **17**, 275 (2007).
10. J. S. Langer and V. Ambegaokar, Phys. Rev. **164**, 498 (1967).
11. D. S. Golubev and A. D. Zaikin, Phys. Rev. B **64**, 014504 (2001).
12. F. Marsili *et al.*, Nature Photon. **7**, 210 (2013).
13. Yu. P. Korneeva *et al.*, Supercond. Sci. Technol. **27**, 095012 (2014).
14. N. Marrocco *et al.*, Appl. Phys. Lett. **97**, 092504 (2010).
15. D. Pan, G. P. Pepe, V. Pagliarulo, C. De Lisio, L. Parlato, M. Khafizov, I. Komissarov, and R. Sobolewski, Phys. Rev. B **78**, 174503 (2008).
16. T. Taneda, G. P. Pepe, L. Parlato, A. A. Golubov, and R. Sobolewski, Phys. Rev. B **75**, 174507 (2007).
17. J. J. Renema *et al.*, Phys. Rev. B **87**, 174526 (2013).
18. J. J. Renema *et al.*, Phys. Rev. Lett. **112**, 117604 (2014).
19. R. Arpaia, M. Ejrnaes, L. Parlato, F. Tafuri, R. Cristiano, D. Golubev, R. Sobolewski, T. Bauch, F. Lombardi, and G. P. Pepe, Physica C **509**, 16 (2015).
20. A. I. Buzdin, Rev. Mod. Phys. **77**, 935 (2005).
21. W. Lang, University of Vienna, private communication (2015).
22. J. E. Mooij, in *Percolation, Localization, and Superconductivity*, edited by A. M. Goldman and S. A. Wolf, NATO ASI, Series B, Vol. 109 (Plenum Press, New York, 1984), pp. 325–370.
23. The attempt frequency  $\Omega$  is the third fitting parameter in both models. Our fitted values are close to that of Ref. 3. They are not shown in Table 142.IV because of their irrelevance to the discussion.
24. C. P. Bean and J. D. Livingston, Phys. Rev. Lett. **12**, 14 (1964).

# Spectral Changes Induced by a Phase Modulator Acting as a Time Lens

## Introduction

First noted in the 1960s, a mathematical equivalence exists between paraxial-beam diffraction and dispersive pulse broadening.<sup>1,2</sup> This equivalence, known as space–time duality, has led to the development of temporal analogs of several spatial optical devices. An important component of such devices is the time lens,<sup>3,4</sup> which is designed to impose a time-dependent parabolic phase across an optical pulse passing through it, just as a traditional lens provides a parabolic phase in space. The development of such a time lens has led to applications such as temporal imaging,<sup>3–6</sup> spectral phase conjugation,<sup>6</sup> and temporal cloaking.<sup>6,7</sup>

Although modern time lenses typically produce the required parabolic phase using nonlinear effects such as four-wave mixing,<sup>6–9</sup> any device that provides a time-dependent parabolic phase can function as a time lens. By using an electro-optic effect to provide this phase, the pulse spectrum can be manipulated without the use of optical nonlinear effects such as self-phase modulation.

An electro-optic phase modulator driven by a sinusoidal signal approximates the parabolic phase of a time lens. This approximation holds for optical pulses aligned with a local maximum or minimum of the modulation cycle. Time lenses made with this arrangement have been well explored.<sup>6,10,11</sup> The behavior for nonstandard configurations, however, where a temporal offset exists between the modulator voltage and optical pulse, has attracted much less attention.

In this article it is shown that by changing this temporal offset, the spectrum of an optical pulse could be selectively broadened, narrowed, or frequency shifted without requiring optical nonlinearities. The following sections (1) present a relevant theory and show the results of numerical simulations; (2) verify theoretical predictions with an experiment performed using 4-ps pulses at 1053 nm and a lithium niobate phase modulator capable of providing a maximum phase shift of 16 rad at a 10-GHz modulation frequency; and (3) summarize the main results.

## Numeric Simulations and Theory

The Fourier-lens configuration, in which an input pulse first propagates inside a dispersive medium before passing through a time lens, is considered first. The length of dispersive medium in this configuration is chosen to be equal to the focal length of the lens. For a linear system, the electric field at the output of the dispersive medium can be related to the input electric field as

$$E_{\text{out}}(t) = \int_{-\infty}^{\infty} E_{\text{in}}(t')h(t-t')dt', \quad (1)$$

where  $h(t)$  is the impulse response of the linear dispersive medium of length  $L$  with the Fourier transform  $\exp[i\beta(\omega)L]$  and  $\beta(\omega)$  is the propagation constant inside the dispersive medium. If  $\phi_m(t)$  is the phase shift imposed by the modulator, the pulse spectrum is obtained by taking the Fourier transform as

$$\tilde{E}_{\text{out}}(\omega) = \int_{-\infty}^{\infty} E_{\text{out}}(t)\exp[i\phi_m(t)]e^{i\omega t} dt. \quad (2)$$

Using the convolution theorem in Eq. (1),  $E_{\text{out}}(t)$  is related to the Fourier transform of  $E_{\text{in}}(t)$  as

$$E_{\text{out}}(t) = \frac{1}{2\pi} \int_{-\infty}^{\infty} \tilde{E}_{\text{in}}(\omega)\exp[i\beta(\omega)L]d\omega. \quad (3)$$

In practice, the propagation constant  $\beta(\omega)$  is Taylor expanded around the central frequency  $\omega_0$  of the pulse spectrum as<sup>12</sup>

$$\beta(\omega)L = \beta_0L + \beta_1L(\omega - \omega_0) + \frac{1}{2}\beta_2L(\omega - \omega_0)^2 + \dots \quad (4)$$

Here,  $\beta_0L$  leads to a constant phase shift and  $\beta_1L$  is a constant temporal delay with no impact on the pulse shape or spectrum. In contrast,  $\beta_2L$  affects not only the width but also the chirp of the pulse.

When an electro-optic phase modulator driven by a sinusoidal clock signal is used as the time lens, the phase shift imposed by it has the form

$$\phi_m(t) = \phi_0 \cos(\omega_m t - \theta), \quad (5)$$

where  $\phi_0$  is the peak amplitude,  $\omega_m$  is the modulation frequency, and  $\theta = \omega_m t_0$  is the phase offset resulting from the time offset  $t_0$  between the peak of the sinusoidal voltage and the peak of the optical pulse. For  $\theta = 0$ , the peak of the sinusoid coincides with the peak of the optical pulse at  $t = 0$ .

In an analogy to the focal length of a traditional lens, the focal group-delay dispersion (GDD) is used to describe a time lens<sup>4</sup> through  $D_f = -1/(\phi_0 \omega_m^2)$ . In the Fourier-lens configuration, the length of the dispersive medium is chosen such that  $D_f = \beta_2 L$ .

To study the impact of finite values of  $\theta$ , the integral in Eq. (3) is calculated numerically and then obtained the spectrum of the output pulse as indicated in Eq. (2). The results presented in Fig. 142.22 show the pulse spectra as functions of  $\theta$  over one modulation cycle as a color-coded surface plot. The parameter values for numerical simulations were chosen to match the capabilities of a modern, commercially available LiNbO<sub>3</sub> phase modulator operating at  $\lambda_0 = 1053$  nm. More specifically,  $\omega_m/2\pi = 10$  GHz and  $\phi_0 = 30$  rad. These values

result in a time aperture of  $\Delta T = 1/\omega_m = 15.9$  ps and a temporal resolution of  $\delta t = 2.77/(\phi_0 \omega_m) = 1.47$  ps (Ref. 6). The focal GDD for the time lens is  $D_f = -8.44$  ps<sup>2</sup>. The temporal phase imparted by the time lens was included exactly using Eq. (5). The dispersion for these simulations is assumed to be ideal, and all coefficients beyond  $\beta_2$  in Eq. (4) are ignored.

Figure 142.22 shows the results for Gaussian input pulses of widths (a) 1.5 ps and (b) 20 ps, with spectral bandwidths of 1.08 nm and 81.4 pm, respectively (all full widths at half maximum). The spectral behavior is quite different for the two pulse widths. It is stressed that even though the pulse spectrum varies considerably with the angle  $\theta$ , the temporal shape of output pulses remains the same for all  $\theta$ .

Figure 142.22(a) obtained for 1.5-ps input pulses shows that the pulse spectrum is narrowest near  $\theta = 0$ . It begins to broaden and shift toward shorter wavelengths as  $\theta$  increases, and the maximum shift of about 1.32 nm occurs for  $\theta = \pi/2$ . After this value, the spectrum shifts toward longer wavelengths, and the spectral width continues to increase until  $\theta = \pi$ , where it reaches its maximum value of 2.23 nm. The spectrum continues to shift toward longer wavelengths until  $\theta$  reaches the value  $3\pi/2$ . Beyond this, the spectrum begins to narrow and recovers its original size at  $\theta = 2\pi$ . Note that the spectral evolution is antisymmetric with respect to  $\theta = \pi$ .

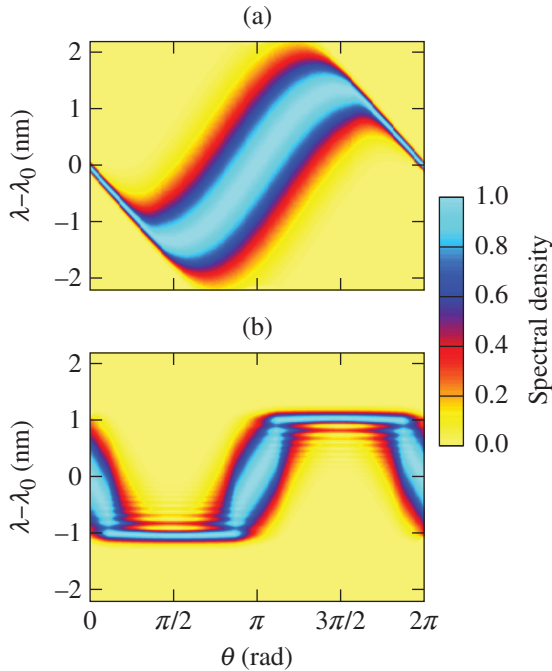
To understand the physical origin of these spectral changes, it is useful to expand  $\phi_m(t)$  in Eq. (5) as a Taylor series around  $t = 0$  as

$$\phi_m(t) = \phi_0 \left\{ \cos\theta - (\omega_m \sin\theta)t - \left[ \frac{\omega_m^2}{2} \cos(\theta) \right] t^2 + \dots \right\}. \quad (6)$$

When there is no phase offset ( $\theta = 0$ ), all odd-order terms vanish in the Taylor expansion. If terms only up to the second order are retained,

$$\phi_m(t) = \phi_0 \left( 1 - \omega_m^2 t^2 / 2 \right). \quad (7)$$

The quadratic term provides a time-dependent parabolic phase shift and fulfills the function of an ideal time lens. The higher-order phase terms in Eq. (6) lead to the temporal equivalent of spatial aberrations and cause distortions in the output pulse shape and spectrum. The time aperture, as defined earlier, is the temporal range over which these higher-order phase terms are small and do not noticeably distort the output of the time lens.<sup>4</sup>



E23823JR

Figure 142.22 Surface plots showing simulated output spectra for different values of  $\theta$  when (a) 1.5-ps and (b) 20-ps Gaussian pulses are sent through a phase modulator acting as a time lens. The color bars show the range of spectral density, normalized to 1 at its peak for each value of  $\theta$ .

The features seen in Fig. 142.22(a) can be understood from Eqs. (2) and (6). It is easy to see that the linear term in the Taylor expansion in Eq. (6) corresponds to a frequency shift in the pulse spectrum by an amount

$$\Delta\omega = \phi_0(\omega_m \sin\theta). \quad (8)$$

This shift is maximum when  $\theta = \pi/2$  and has the value  $\Delta\nu = \phi_0\omega_m/2\pi$ . For values of  $\phi_0 = 30$  rad and  $\omega_m/2\pi = 10$  GHz, this gives a maximum shift of 300 GHz or 1.11 nm at  $\lambda = 1053$  nm—a value that is close but not identical to the numerical value of 1.32 nm in Fig. 142.22(a). The source of this difference will be discussed later. It is important to note that the frequency shift is the same regardless of the central wavelength of the input pulse. Therefore, a phase modulator with the same parameters operating at a longer wavelength would produce a larger wavelength shift. For example, a phase modulator at 1550 nm with the same parameters would produce a wavelength shift of about 2.4 nm.

In addition to the linear phase term, the parabolic phase term changes with  $\theta$  as  $\phi_2 = -\phi_0\omega_m^2 \cos(\theta)$ . This dependence changes the focal GDD of the time lens as  $D_f(\theta) = -[\phi_0\omega_m^2 \cos(\theta)]^{-1}$ . The minimum focal GDD occurs at  $\theta = 0$  and increases in magnitude for other phase offsets. Additionally, the sign of the focal GDD is inverted between  $\theta = \pi/2$  and  $\theta = 3\pi/2$ . This situation is analogous to changing from a convex to a concave lens. Changes in the bandwidth of the output spectrum seen in Fig. 142.22(a) result from this  $\theta$  dependence of the focal GDD.

Figure 142.23 compares the output and input spectra of 1.5-ps pulses for three specific values of  $\theta$ . In Fig. 142.23(a), the

width of the output spectrum is only 0.136 nm, i.e., the output spectrum is narrowed by a factor of nearly 8 when compared to the input spectrum. This spectral compression is the temporal analog of the collimation of an optical beam realized with a lens and may be useful for applications requiring a narrow-bandwidth source. Just as in the spatial case, where angular divergence is reduced by expanding the size of the optical beam, spectral compression is accomplished at the expense of a broader pulse. The dispersive medium broadens the pulse while chirping it simultaneously, and the modulator is used to cancel the chirp and produce a transform-limited pulse. For this reason, the spectrum is compressed by the same factor by which the pulse broadens in the time domain.

Figure 142.23(b), drawn for  $\theta = \pi/2$ , shows that the spectrum is shifted toward shorter wavelengths by 1.32 nm without a significant change in the spectral width. Such wavelength shifts do not require the Fourier-lens configuration and have been used for spectral shearing interferometry by passing a pulse directly through a modulator.<sup>13</sup> In our case, the spectral shift reaches a maximum at  $\theta = \pi/2$  and  $\theta = 3\pi/2$  as predicted by the theory, where the peak of the pulse coincides with the maximum slope of the time-dependent phase. Deformation of the spectral shape in Fig. 142.23(b) is caused by the cubic term in Eq. (6). This term is also responsible for the larger 1.32-nm shift compared to that predicted by the linear term. Indeed, if the simulations are repeated and only kept up to the quadratic terms of Eq. (6), the input and output spectra become identical except for a spectral shift whose magnitude of 1.11 nm coincides with the theoretical estimate presented earlier.

Figure 142.23(c) shows that the spectral shift disappears for  $\theta = \pi$ . This feature is easily understood from Eq. (6), showing

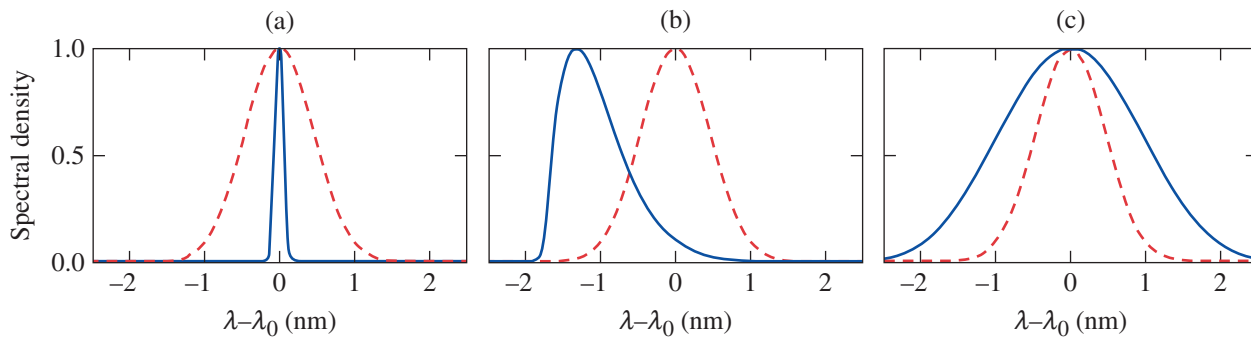


Figure 142.23

Comparison of input (dashed) and output (solid) spectra for a 1.5-ps input pulse at clock phases (a)  $\theta = 0$ , (b)  $\theta = \pi/2$ , and (c)  $\theta = \pi$ .

that both the linear and cubic terms vanish for this value of  $\theta$ . Finally, the spectral broadening seen in Fig. 142.23(c) originates from the sign change of the quadratic term in Eq. (6) for  $\theta = \pi$ . In effect, the modulator is now acting analogous to a concave lens that increases the angular spread of a beam incident on it.

The 2.23-nm spectral bandwidth, occurring at  $\theta = \pi$ , indicates broadening by a factor of about 2. Unlike spectral broadening from effects like self-phase modulation, the spectrum broadened by a time lens maintains its initial shape, as is apparent in Fig. 142.23(c). Slight distortions in the spectral wings have their origin in the fourth-order term in Eq. (6).

The results of Fig. 142.22(b) show that for the 20-ps input pulse, the pulse experiences negligible broadening when passing through the dispersive medium. However, the pulse is already longer than the aperture of the time lens. This results in a behavior that is qualitatively different from that seen in Fig. 142.22(a) for the shorter 1.5-ps pulse. More specifically, the spectrum is wider at  $\theta = 0$  and becomes narrowest at  $\theta = \pi/2$ , reaching a minimum bandwidth of 0.158 nm. The spectrum then broadens again near  $\theta = \pi$ , where the time lens once again acts like a concave lens and reaches a bandwidth of 1.58 nm. The behavior at  $\theta = 0$  and  $\theta = \pi$  is analogous to a highly collimated optical beam incident on either a convex lens or a concave lens, respectively. For a highly collimated beam, the beam shape does not change with propagation. The angular spread of the beam is affected, however, by the lens: both convex and concave lenses expand it.

## Experimental Results

A schematic of the experimental setup is shown in Fig. 142.24. A mode-locked laser<sup>14</sup> producing 150-fs pulses at 1053 nm, with a 38-MHz repetition rate, was used as a source of optical pulses. The time lens was implemented using an electro-optic phase modulator. A high-efficiency lithium niobate phase modulator<sup>15</sup> designed to operate at a wavelength of 800 nm but usable at 1053 nm was used. The 10-GHz clock signal used to drive the phase modulator was produced with phase locking.<sup>16</sup> A fast photodiode created an electronic signal of the laser pulse train, and a 76-MHz bandpass filter produced a synchronization signal at the second harmonic of the 38-MHz laser repetition rate. This 76-MHz signal matches the resonant frequency of a commercially available phase-locked dielectric resonator oscillator (PDRO), and it was locked to one of the harmonics of the 76-MHz signal around 10 GHz. The 10-GHz output was sent through a “trombone” phase shifter controlled with a translation stage driven by a stepper motor. Using an oscilloscope,

each step of the motor was found to produce a 42-fs delay in the 10-GHz clock signal, corresponding to 2.63 mrad of clock phase shift. The shifted signal was amplified by a 33-dBm microwave amplifier and used to drive the phase modulator. This setup produced a peak phase shift of  $\phi_0 = 16$  rad, a value lower than the 30 rad used in numerical simulations. For this reason, the range of spectral bandwidths and spectral shifts is reduced compared to the simulations. The time lens has a time aperture of  $\sim 15.9$  ps, a resolution time of  $\delta t = 2.8$  ps, and a focal GDD of  $D_f = -15.8$  ps<sup>2</sup>.

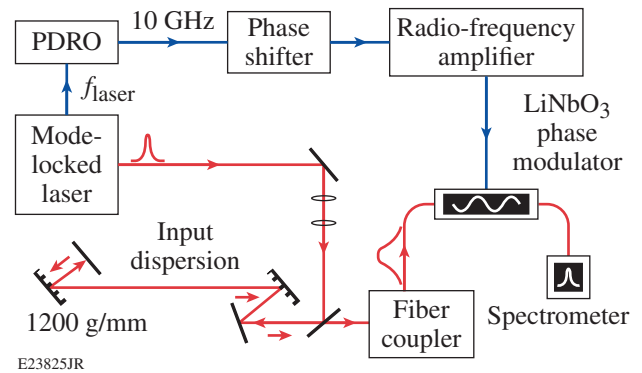


Figure 142.24

Experimental setup for a time-to-frequency converter using a phase modulator as a time lens. PDRO: phase-locked dielectric resonator oscillator.

The time lens was used in the Fourier-lens configuration, and a grating pair was used as a dispersive delay line. The delay line was created using two 1200-lines/mm reflective diffraction gratings separated by 80 cm with an incident angle of  $25.3^\circ$  to produce a GDD that matched  $D_f = -15.8$  ps<sup>2</sup> of our time lens. The chirped and broadened pulse was then sent through the phase modulator. For different clock phases, the pulse spectrum was recorded using an optical spectrum analyzer.<sup>17</sup>

Two different filters were applied to the laser signal to broaden the 150-fs pulses. A slit filter was used between the parallel gratings to create a spectral width of 0.407 nm, corresponding to Gaussian pulses of  $\sim 4$ -ps duration. In addition, a volume Bragg grating with a spectral width of 0.108 nm produced longer pulses of  $\sim 19$ -ps duration, assuming transform-limited pulses.

The experimentally recorded spectra are shown in Fig. 142.25. Comparing the short-pulse cases of Fig. 142.25(a) with Fig. 142.22(a), it is seen that the two cases agree qualita-

tively. In particular, the experimental spectra follow an identical progression as  $\theta$  advances through the phase-modulation cycle. As predicted by theory in the previous section, the experimental spectrum is narrowest at  $\theta = 0$ , reaches maximum spectral shift at  $\theta = \pi/2$  and  $\theta = 3\pi/2$ , and exhibits the largest spectral broadening at  $\theta = \pi$ .

Figure 142.26 compares [(a)–(c)] the experimentally recorded and [(d)–(f)] theoretically predicted output spectra for the same three values of  $\theta$  in the case of 4-ps input pulses. The numerical simulations used the experimentally recorded input spectrum (shown by a red dashed line for comparison) to obtain the temporal profile, assuming that pulses were transform limited. The agreement between the theory and experiment is quite good in all cases.

In agreement with the numerical simulations presented in the previous section, spectral compression at  $\theta = 0$  in Figs. 142.26(a) and 142.26(d) is observed. The width of the output spectrum is 0.18 nm, indicating that the pulse spectrum is compressed by a factor of about 2, which is considerably smaller than the factor of 8 observed in Fig. 142.23(a). The reduced compression factor is caused by the smaller spectral width of 4-ps input pulses and 16-rad maximum phase shift of the modulator used in our experiment. For the same reason, the spectral shift of 0.68 nm seen in Fig. 142.26(b) for  $\theta = \pi/2$  is also smaller compared to that seen in Fig. 142.23(b). The spectrum in Fig. 142.26(b) also has a small bump near  $\lambda = \lambda_0$  that is not present in Fig. 142.26(e). This bump arises from the polarization dependence of our phase modulator. More specifically, the modulator produces a significantly smaller

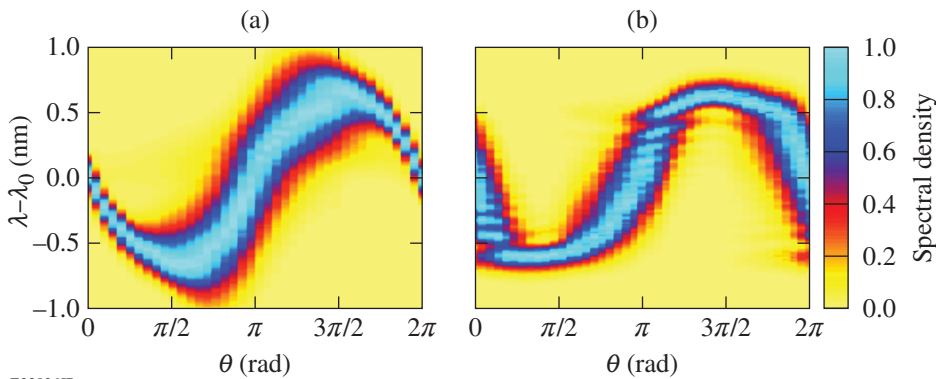


Figure 142.25

Surface plots showing experimental output spectra for different values of  $\theta$  when input pulses were filtered to produce (a) 0.407- and (b) 0.107-nm-wide input spectra. The color bars show the range of spectral density, normalized to 1 at its peak for each value of  $\theta$ .

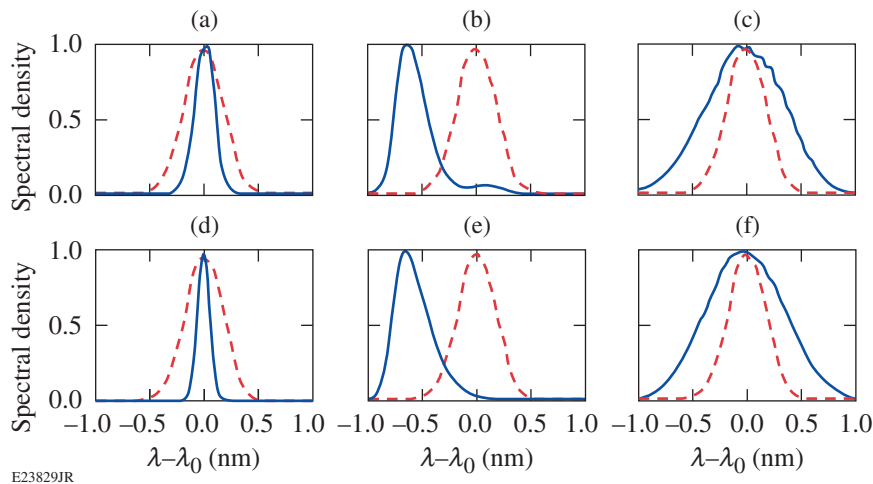


Figure 142.26

Comparison of [(a)–(c)] experimental and [(d)–(f)] simulated output spectra (solid blue line) for [(a),(d)]  $\theta = 0$ , [(b),(e)]  $\theta = \pi/2$ , and [(c),(f)]  $\theta = \pi$ . The input spectrum is shown by the dashed red line.

value of  $\phi_0$  along the slow axis compared to the fast axis. A small mismatch between the pulse's polarization direction and the slow axis of the phase modulator produces the bump in the spectrum seen in Fig. 142.26(b). Because our theory does not include polarization effects, this bump is not reproduced in Fig. 142.26(e).

As seen in Figs. 142.26(c) and 142.26(f), the pulse spectrum has a bandwidth of 0.86 nm when  $\theta = \pi$ , i.e., it has been broadened by a factor of 2.1, while the shape of the input spectrum is nearly preserved. Some distortion of the spectral shape is observed because the pulse is chirped in time during the input dispersion, causing wavelengths farther away from the central wavelength to move toward the wings of the pulse. Since pulse wings experience aberrations from higher-order phase terms in the time lens, small distortions appear in the shape of the spectrum. It is emphasized, however, that a suitably designed time lens can broaden considerably the spectrum of a pulse without significantly distorting its shape. In this respect, a time lens is superior to the use of self-phase modulation, which invariably distorts the spectrum while broadening it (and also requires high pulse energies).

### Conclusion

Spectral narrowing, broadening, and shifts have been demonstrated for picosecond pulses using a lithium niobate electro-optic phase modulator acting as a time lens. These spectral effects depend on the maximum phase shift that can be imposed by the modulator. In the numerical simulations presented, the pulse spectrum was compressed by a factor of 8 for a 30-rad phase shift. Experimentally, spectral shifts over a 1.35-nm range and spectral narrowing and broadening by a factor of 2 were demonstrated using a lithium niobate phase modulator with a maximum phase shift of 16 rad at a 10-GHz modulation frequency. More-dramatic narrowing, broadening, and shifts could be achieved by cascading multiple phase modulators to produce higher phase amplitudes and shorter focal GDD's. This work shows that a phase modulator can be used to tune the central frequency and the spectral bandwidth of picosecond pulses emitted by mode-locked lasers.

### ACKNOWLEDGMENT

B. Plansinis was supported by a Horton Fellowship. This material is based upon work supported by the Department of Energy National Nuclear Security Administration under Award Number DE-NA0001944, the University of Rochester, and the New York State Energy Research and Development Authority. The support of DOE does not constitute an endorsement by DOE of the views expressed in this article.

### REFERENCES

1. P. Tourniois, C. R. Acad. Sci. **258**, 3839 (1964).
2. S. A. Akhmanov, A. P. Sukhorukov, and A. S. Chirkin, Sov. Phys. JETP **28**, 748 (1969).
3. B. H. Kolner and M. Nazarathy, Opt. Lett. **14**, 630 (1989).
4. B. H. Kolner, IEEE J. Quantum Electron. **30**, 1951 (1994).
5. C. V. Bennett and B. Kolner, IEEE J. Quantum Electron. **36**, 430 (2000).
6. R. Salem, M. A. Foster, and A. L. Gaeta, Adv. Opt. Photon. **5**, 274 (2013).
7. M. Fridman *et al.*, Nature **481**, 62 (2012).
8. D. H. Broaddus *et al.*, Opt. Express **18**, 14,262 (2010).
9. A. Pasquazi *et al.*, IEEE J. Sel. Top. Quantum Electron. **18**, 629 (2012).
10. A. A. Godil, B. A. Auld, and D. M. Bloom, Appl. Phys. Lett. **62**, 1047 (1993).
11. B. H. Kolner, Appl. Phys. Lett. **52**, 1122 (1988).
12. G. P. Agrawal, *Nonlinear Fiber Optics*, 5th ed. (Elsevier, Amsterdam, 2013).
13. C. Dorrer and J. Bromage, Opt. Lett. **35** 1353 (2010).
14. High Q Laser Production GmbH, model femtoTRAIN IC-1053-400 fsYb, see <http://www.spectra-physics.com/products/ultrafast-lasers/femtotrain> (25 February 2015).
15. EOSpace, Inc., Redmond, WA 98052; see <http://www.eospace.com> (25 February 2015).
16. I. Kang, C. Dorrer, and F. Quochi, Opt. Lett. **28**, 2264 (2003).
17. Yokogawa Electric Corporation, Optical Spectrum Analyzer, Model AQ6317b, see <http://tmi.yokogawa.com/discontinued-products/ando/ando/810804100-aq6317b-optical-spectrum-analyzer/> (26 February 2015).

# Surface-Texture Evolution of Different Chemical-Vapor-Deposited Zinc Sulfide Flats Polished with Various Magnetorheological Fluids

## Introduction

Zinc sulfide (ZnS) is an infrared (IR) optical material widely used for applications such as IR windows, domes, and optical lenses.<sup>1</sup> It is industrially produced by the chemical-vapor-deposition (CVD) technique to reach a dense, milky yellow–orange color, with ~70% transmission in the mid-long-wave IR region.<sup>1</sup> Its inner structure consists of cone-like structures that grow larger as deposition takes place, up to a thickness of a few centimeters.<sup>2,3</sup> These cone-like structures manifest on the top of the deposited surface as “pebbles”<sup>2</sup> or “hillocks”<sup>4</sup> and are often called “alligator skin.”<sup>5</sup>

The importance of good surface finishing of an optical component is well understood. The lack of good finishing results in the scattering and absorption of light, leading to low optical performance.<sup>1,6</sup> Polishing out the pebble structure from a CVD ZnS substrate to a relatively smooth [ $<3$ -nm root mean square (rms)] surface is quite challenging, especially for an undestructive polishing process<sup>7</sup> (that leaves no plastic deformation and does not destroy the crystallographic array of the top finished layer), such as the magnetorheological finishing (MRF) technique.

MRF is a deterministic, sub-aperture polishing process that is capable of polishing flats, spheres, and aspheric shapes.<sup>8</sup> It uses a magnetorheological (MR) fluid composed of micron-size carbonyl iron (CI) powder, water, stabilizing additives, and abrasives (like ceria or nanodiamonds). When exposed to a magnetic field, the fluid stiffens as the CI particles align with the magnetic field, and functions as a polishing pad with a layer of nonmagnetic abrasive particles on the top layer. This fluid is kept at a relatively high pH (10 or higher) to suppress corrosion of the iron particles. By suppressing corrosion, a conventional MR fluid can last more than three weeks.

Kozhinova *et al.*<sup>2</sup> and Hallock *et al.*<sup>9</sup> demonstrated an improvement in surface artifacts on CVD ZnS and zinc selenide (ZnSe), respectively, during MRF by using acidic (pH ~4.5) MR fluids and soft CI particles; however, the MR fluids used in their work did not provide consistent and repeatable results. The two

main challenges they faced were (a) a material-removal-rate performance that varied among CVD ZnS substrates manufactured by different vendors (0.5 to 1.5  $\mu\text{m}/\text{min}$ ) and (b) rapid corrosion of the CI particles in the MR fluid.

There is no consensus of deposition parameters for CVD ZnS.<sup>4,10</sup> Different manufacturers select different deposition conditions (such as deposition temperature, pressure, and vapor velocity). Therefore, it is reasonable to assume that physical properties of the final product, such as color, average grain size, and crystallographic orientation volume fraction, are different among vendors and might lead to variations in polishing results among different parts during MRF.

In 2008 a novel zirconia sol-gel coating process to protect CI particles from corrosion was invented at the University of Rochester.<sup>11</sup> These coated particles were successfully mixed into a MR fluid at pH 8 to perform a MRF experiment on several optical substrates.<sup>12</sup> In 2013 (Ref. 13) we reported on a MRF experiment using MR fluids based on the same zirconia-coated CI (Zr-CI) particles at pH levels of 4, 5, and 6 as in Fig. 142.27. In that experiment we used single-crystal

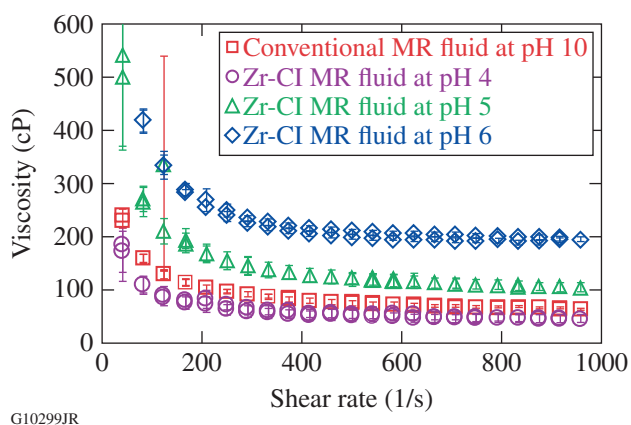


Figure 142.27 Viscosity versus shear-rate plot for conventional MR fluid at pH 10 (squares) and zirconia-coated-CI (Zr-CI) MR fluids at pH 4 (circles), pH 5 (triangles), and 6 pH (diamonds).

ZnS planes to investigate the role of material-removal-rate anisotropy of polycrystalline (pc) CVD ZnS during MRF. The results showed a relatively uniform removal rate ( $0.06 \mu\text{m}/\text{min}$ ) for single-crystal planes when using MR fluid at pH 4. The conclusions presented here predicted an improvement in surface artifacts (the emergence of pebbles on the surface) when using this type of fluid for MRF polishing of a CVD ZnS substrate.

Here the authors present the surface-texture evolution of several differently grown CVD ZnS substrates that were MRF polished with four MR fluids at pH levels of 10, 6, 5, and 4. The goal was twofold: to check (1) if a decrease in MR fluid pH improves the surface artifacts of a CVD ZnS surface during MRF polishing; and (2) if MR fluid pH is capable of dealing with part-to-part variations in the surface texture among CVD ZnS materials deposited by different vendors.

## Experimental

### 1. Polycrystalline CVD ZnS Substrates

Four CVD ZnS substrates were purchased from four different vendors: one is an elemental CVD ZnS substrate purchased from China; the other three are forward-looking-infrared (FLIR) CVD ZnS substrates purchased from China and the U.S. The difference between the two types is the chemical reaction of the precursor gases (for more information, refer to Refs. 1 and 6). We will refer to them as substrates A (FLIR, U.S.), B (FLIR, U.S.), C (FLIR, China), and D (elemental, China). Each sample measured 40 mm in diameter and 5 mm in thickness. The samples were pre-polished in-house on pitch with diamond abrasives (as described in Ref. 2) to a peak-to-valley (p-v) flatness of  $1\lambda$  to  $2\lambda$  and an areal roughness of less than 27-nm p-v and 2-nm rms.

### 2. X-Ray Diffraction

To determine the relative portion of crystallite orientations within the samples, an x-ray diffraction (XRD) analysis was performed using a general-purpose x-ray diffractometer (Philips X'Pert, MPD system). Cu  $K_{\alpha 1}$  radiation ( $\lambda_{\text{Cu}} = 1.5418 \text{ \AA}$ ) was used to produce an x-ray diffraction pattern in a  $2\theta$  angle range of

$10^\circ$  to  $70^\circ$  with step intervals of  $2\theta = 0.03^\circ$ . The diffraction data were analyzed using X'Pert High Score software. The reference database for cubic ZnS was taken from the Joint Committee for Powder Diffraction Standards (JCPDS) filed by the International Centre for Diffraction Data, Newtown Square, PA. We used JCPDS files 65-0309, 65-5476, and 65-1691.

### 3. MRF Spotting Experiment

MRF spotting experiments were performed on a research platform referred to as the "spot-taking machine" (STM). It has features similar to a conventional MRF machine; however, it is free to move only in the vertical  $z$  direction. Consequently, it is capable of performing only single spots on the surface. The MR fluids used here were a conventional diamond fluid (D11) at pH 10, purchased from QED Technologies<sup>14</sup> and Zr-CI-based<sup>11</sup> MR fluids at pH levels of  $\sim 4$ ,  $\sim 5$ , and 6, developed in our laboratory. The initial fluid composition of the Zr-CI fluid, before the addition of any acid, is given in Table 142.V. For the experiment with the conventional fluid, each CVD ZnS substrate was spotted once for 60 s. For the experiment with the Zr-CI fluids, each substrate was spotted once at pH  $6.00 \pm 0.0$ , once at pH  $5.12 \pm 0.0$ , and once at pH  $4.22 \pm 0.1$ . Each spot lasted 10 min as a result of the lower removal rate of 0.06 to  $0.16 \mu\text{m}/\text{min}$  ( $0.06 \mu\text{m}/\text{min}$  at pH 4 and  $0.16 \mu\text{m}/\text{min}$  at pH 6). The Zr-CI MR fluid was first loaded on the STM at pH  $6.00 \pm 0.0$ . After spotting the substrates, the fluid pH was lowered to 5.12 using  $\sim 4$  ml of 8-M nitric acid for another round of spotting, which was followed by an additional reduction in pH to 4.22 using  $\sim 5$  ml of 8-M nitric acid. During the spotting experiment at pH 4.22, additional acid was continuously added to maintain the fluid pH level at  $\sim 4.20$ . Because of water evaporation from the MR fluids during the experiment, any addition of acid had a negligible effect on the CI particles' concentration in it. The percentage of fluid moisture when the experiment was over was 20.42%, less than 1-wt% difference from what it was at the beginning. The MR fluids at pH 4.22 will be referred to as pH 4, at 5.12 as pH 5, and at 6.00 as pH 6. The machine settings were a ribbon height of 1.4 to 1.6 mm; a penetration depth of 0.2 mm; a wheel speed of 200 rpm; a pump speed of 110 rpm; and an

Table 142.V: Initial Zr-CI MR fluid composition before adjusting pH with 8-M nitric acid. The fluid pH is  $\sim 6.0$ .

Material	$\rho$ (g/ml <sup>3</sup> )	Volume (ml)	$M$ (g)	Volume (%)	wt%
Zr-CI powder	6.72	384.80	2583.93	38.60	80.67
Polyethylenimine (PEI) solution	1.10	69.68	76.65	6.99	2.39
H <sub>2</sub> O	1.00	542.36	542.36	54.41	16.93
Total	—	996.84	3202.94	100.00	99.99

electric current of 15 Å. When the experiment was finished, each substrate had four spots on its surface, one at each pH. During the experiment, special attention was paid to removing at least 0.5 μm at the deepest point of removal. This was based on the observations of Kozhinova *et al.*,<sup>2</sup> which stated that pebbles start to appear on pre-polished surfaces of CVD ZnS once a minimum of 0.5 μm of material has been removed with MRF.

#### 4. MR Fluid Rheology

MR fluid off-line viscosity was measured using a Brookfield cone/plate rheometer.<sup>15</sup> At each pH, ~0.5 ml of fluid was extracted directly from the mixing vessel of the STM and placed on the viscometer plate. The fluid went through a time test in which the shear rate went from 0 1/s to 200 1/s for 30 s and then went back down to 0 1/s for another 30 s. This helped to minimize the transient behavior of the fluid. Following the time test, we measured the viscosity of the fluid as a function of shear rate from 40 to 1000 1/s. All measurements were repeated three times.

#### 5. Metrology

To evaluate the emergence of pebbles on the surface inside the spots, we used a Zygo NewView5000 white-light interferometer with a 1× Mirau objective and a 0.8× zoom.<sup>16</sup> The low magnification provides a large field of view that is more suitable for observing submillimeter features, such as pebbles. The spots were masked along the inner edge, and a cylinder shape was removed from the remaining masked surface. The areal rms roughness of the masked area was recorded and plotted along with ten manually drawn lineout profiles in the direction of the MRF ribbon. A power spectral density (PSD) was also analyzed in the *x* direction using the “average X PSD” function in the accompanying software MetroPro. To do that,

a rectangular area (2 mm × 1 mm) was masked around the depth of deepest penetration (ddp) of each spot. This analysis also provided information about the degree of waviness of the spotted surfaces.

### Results

#### 1. X-Ray Diffraction of CVD ZnS Substrates

Table 142.VI shows the XRD results of the relative intensity of crystallite orientation within the samples. For all samples, the peaks were normalized to the highest peak; i.e., for samples A, C, and D, the intensity peaks were normalized to the (111) peak, whereas for sample B, the peaks were normalized to the (311) peak. From Table 142.VI it is seen that the relative intensity rating is different among the four samples. For example, sample A's XRD results show that the (111) plane has the highest relative intensity score followed by plane (200) and then plane (311). For sample B, the ranking from high to low for the first three peaks is (311) followed by (111) and (200). This inconsistency in the order of diffracting planes is also the case for samples C and D.

#### 2. MR Fluids' Off-Line Viscosity and Material-Removal Rate

Figure 142.27 shows the off-line viscosity of all fluids as a function of shear rate. The viscosity of the Zr-CI fluid is pH dependent. It decreases as pH decreases, although the CI particle concentration has not changed (80 to 81 vol %). The fluid's off-line viscosities at ~800 (1/s)—a shear rate corresponding to that experienced by an MR fluid when ejected from the STM nozzle<sup>12</sup>—are ~60 cP for the conventional MR fluid and ~194, ~109, and ~47 cP for pH 6, 5, and 4, respectively, for the Zr-CI MR fluids. The MR fluid at pH 4 has the lowest viscosity of all fluids.

Table 142.VI: Relative intensity of CVD ZnS substrates from four vendors with respect to diffraction angle ( $2\theta$ ) and crystallographic plane. The shaded cells represent the highest peak that was used to normalize the rest of the data. FLIR: forward-looking infrared.

Approximate diffraction angle $2\theta$ (°)	Diffracting planes at $2\theta$	Relative intensity within sample (%)			
		FLIR			Elemental
		Sample A JCPDS 65-0309	Sample B JCPDS 65-5476	Sample C JCPDS 65-1691	Sample D JCPDS 65-5476
28.5	111	100	70.2	100	100
33.1	200	84.3	43.8	48.0	2.14
47.5	220	25.3	15.5	23.9	22.2
56.3	311	69.3	100	59.8	13.4
59.1	222	2.1	0.9	1.6	1.7
69.5	400	48.4	28.5	33.1	1.2

Table 142.VII presents the material peak-removal rates (pr-r's) of the different fluids. The material removal rate of the Zr-CI MR fluid is significantly lower than that of the conventional MR fluid. This is expected because our MR fluids had no added abrasives, in contrast to the conventional MR fluid. However, prr results for CVD ZnS at pH 6 are similar to what were previously published by Shafrir *et al.*<sup>12</sup> when working with this type of Zr-CI particles in their MR fluid at pH 8. The Zr-CI fluid at pH 4 has the lowest prr of 0.06  $\mu\text{m}/\text{min}$ . Note that the Zr-CI MR fluid has no additive abrasives in it besides

Table 142.VII: Peak removal rate in  $\mu\text{m}/\text{min}$  of the different MR fluids and their pH level.

MR fluid type	MR fluid pH	Peak removal rate ( $\mu\text{m}/\text{min}$ )
Conventional fluid (with diamond abrasives)	10	3.50
Zr-CI (without abrasives)	6	0.16
	5	0.10
	4	0.06

possible free nanozirconia particles that are co-generated during the coating process,<sup>11,17</sup> while the conventional MR fluid contains nanodiamond abrasives.

### 3. Surface Texture and Artifacts After MRF Polishing

The surface texture inside the MRF spots is composed mostly of submillimeter features. Figure 142.28 shows the PSD (in a log scale) for CVD ZnS surfaces spotted with a conventional MR fluid at pH 10 and Zr-CI MR fluids at pH 6, 5, and 4. For all (four) vendors, results show that surface texture and waviness are higher at pH 6, somewhat lower at pH 5, but significantly lower at pH 4. When compared with the conventional MR fluid at pH 10, the use of the Zr-CI MR fluid at pH 4 is comparable. For two of the ZnS materials [Figs. 142.28(b) and 142.28(c)], the Zr-CI MR fluid leads to lower PSD than the conventional MR fluid.

The areal rms roughness and the average lineout profiles taken within the spots are presented in Figs. 142.29(a) and 142.29(b), respectively. For all vendors, when polishing with the Zr-CI MR fluids, both areal (a 2-mm  $\times$  4-mm “D”-shaped)

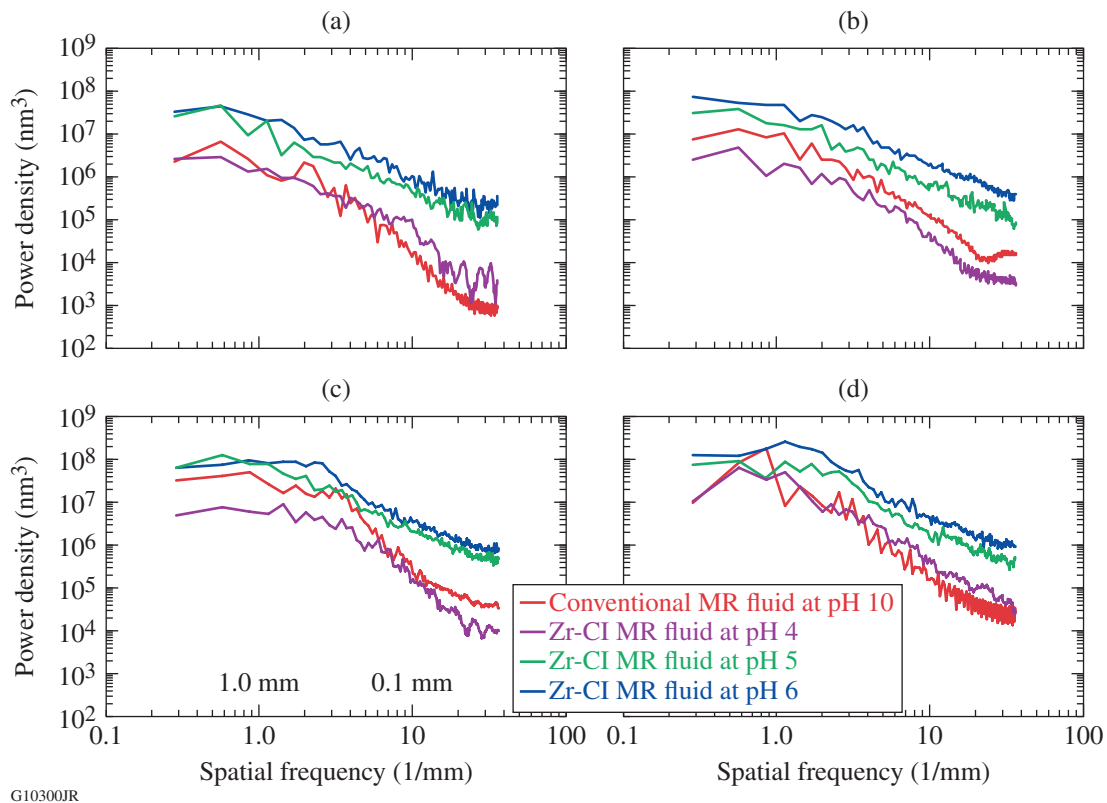
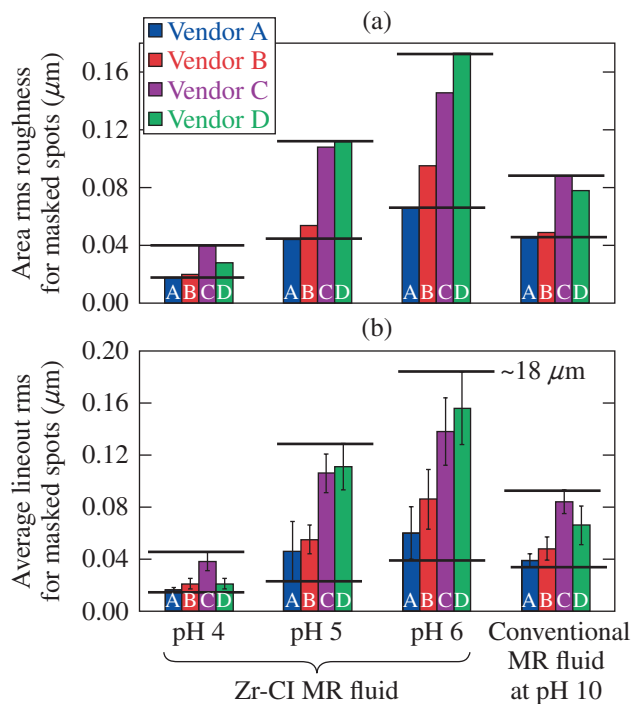


Figure 142.28 Average power spectral density (PSD) along the  $x$  direction for conventional MR fluid (blue), Zr-CI MR fluid at pH 6 (red), pH 5 (green), and pH 4 (purple) for samples A–D, respectively.



G10301JR

Figure 142.29

Macroroughness (rms) versus fluid pH for conventional MR fluid at pH 10 and Zr-CI MR fluid at pH 6, pH 5, and pH 4. (a) Areal rms roughness of a 2-mm  $\times$  4-mm “D”-shaped area; (b) average rms roughness taken from ten lineout profiles (3- to 4-mm-long lines). Horizontal lines are used to guide the eye, identifying the maximum and minimum values.

rms roughness and average lineout profiles (3 to 4 mm long) decrease with a reduction in MR fluid pH and viscosity. Moreover, the Zr-CI MR fluid at pH 4 shows lower rms roughness than the conventional MR fluid. Interestingly, variation in roughness from sample to sample is minimal when polishing with this type of fluid.

It is important to mention that roughness measurements were taken at a low resolution; therefore, it is suitable to relate to the data as it represents surface texture (at length scales 0.05 to 1 mm) rather than surface microroughness, which is not given here.

## Discussion

X-ray diffraction results for the tested substrates show that the portions of the common crystallite orientations within each sample vary from sample to sample. McCloy *et al.*<sup>18</sup> showed that the crystallographic structure and the crystallite orientations of CVD ZnS material vary along the growth direction during deposition. From their powder XRD tests, the portion of the 200 and 400 orientations in the mandrel area is higher than that in the free surface. On the contrary, the portion of the

220 orientation increases as deposition takes place. Therefore, it can be concluded that the sample crystallographic properties depend on the physical location of the cut (top, middle, or mandrel side) and the desired dimensions of the cut (thin or thick). Unless one can control the cut position when purchasing a CVD ZnS substrate, variations in the crystallographic properties are a given fact. In addition, as mentioned in the **Introduction** (p. 110), there is no consensus on deposition settings for CVD ZnS. This likely affects the relative portions of the crystallite orientations within the deposited material and adds to the variations in properties among samples purchased from different manufacturers. It is believed that this nonuniformity in crystallographic properties within the material and among materials manufactured by numerous vendors is the source for anisotropy in the material removal rate during MRF polishing, which leads to surface artifacts of CVD-grown materials, such as ZnS.

In the MRF spotting experiments, the Zr-CI MR fluids' viscosity is observed to be pH dependent. Viscosity significantly decreased with a decrease in pH because the acid increased the zeta potential of the Zr-CI particles and helped disperse the fluid as pH decreased.<sup>13</sup> The drop in viscosity also influenced the prr, which decreased consequently. The material prr of the conventional MR fluid is significantly higher than that of the Zr-CI MR fluids, even though it has relatively low viscosity. Since all fluids have similar CI particles concentration, this was likely a result of the nanodiamond abrasives within the conventional MR fluid.

From the PSD results, the MRF with Zr-CI MR fluid at pH 4 achieved a remarkable improvement in surface texture (lower spatial frequency range) and surface microroughness (higher spatial frequency range) than the fluids at pH 5 and pH 6. This is the case for all four CVD ZnS substrates. The performance of this fluid at pH 4 is slightly better than the conventional MR fluid for substrates manufactured by vendors B and C but comparable for substrates manufactured by vendors A and D. Clearly, a lower value of PSD indicates a surface with a lower texture. Therefore, it can be concluded that the emergence of pebbles on the surface of CVD ZnS substrates can be reduced when using Zr-CI MR fluid at pH 4.

Root-mean-square (rms) data collected from a masked area inside the spots and as multiple lineouts (given in Fig. 142.29) support the results obtained from PSD analysis. Reduction in surface texture is observed as the Zr-CI fluid pH and viscosity drop down. Moreover, from both areal [Fig. 142.29(a)] and lineout [Fig. 142.29(b)] results, the ability of this fluid at

pH 4 to maintain similar performances among all four tested substrates is clearly observed. Therefore, among CVD ZnS substrates deposited by different manufacturers, variations in areal and lineout rms roughness from part to part are minimal when using Zr-CI MR fluid at pH 4.

### Conclusions

It has been demonstrated that variations in the portions of crystallite orientations exist among the CVD ZnS substrates manufactured by different vendors, making it challenging to get a consistent performance during MRF polishing of such differently grown material. The results show that when several CVD ZnS substrates are polished by MRF with a Zr-CI MR fluid at pH 4, both pebble emergence and part-to-part variations in surface texture are minimized. The performance of the Zr-CI MR fluid at pH 4 was better than those of MR fluids with pH levels of 5 and 6. On the other hand, for some ZnS materials, the Zr-CI MR fluid at pH 4 produced diminished features (at a scale length of 0.03 to 1 mm) as compared to the conventional MR fluid. Of course, the Zr-CI MR fluid at low pH has a particularly low material prr, especially at pH 4, which is expected because of the absence of any abrasives. The authors believe that adding some type of abrasive, such as ceria or nanodiamonds, will likely boost the overall prr of the Zr-CI MR fluid and improve its efficiency.

### ACKNOWLEDGMENT

This material is based upon work supported by the Department of Energy National Nuclear Security Administration under Award Number DE-NA0001944, the University of Rochester, and the New York State Energy Research and Development Authority. The support of DOE does not constitute an endorsement by DOE of the views expressed in this article.

### REFERENCES

1. D. C. Harris, *Materials for Infrared Windows and Domes: Properties and Performance*, Tutorial Texts in Optical Engineering (SPIE Optical Engineering Press, Bellingham, WA, 1999), Vol. PM70.
2. I. A. Kozhinova, H. J. Romanofsky, A. Maltsev, S. D. Jacobs, W. I. Kordonski, and S. R. Gorodkin, *Appl. Opt.* **44**, 4671 (2005).
3. T. Zscheckel, W. Wisniewski, and C. Rüssel, *Adv. Funct. Mater.* **22**, 4969 (2012).
4. K. L. Lewis, A. M. Pitt, and J. A. Savage, in *Proceedings of the Ninth International Conference on Chemical Vapor Deposition 1984*, edited by Mc. D. Robinson *et al.* (Electrochemical Society, Pennington, NJ, 1984), pp. 530–545.
5. J. S. McCloy, "Properties and Processing of Chemical Vapor Deposited Zinc Sulfide," Ph.D. thesis, University of Arizona, 2008.
6. Z. Fang *et al.*, *Key Eng. Mater.* **280–283**, 537 (2005).
7. Y. Namba and H. Tsuwa, *CIRP Ann.* **28**, 425 (1979).
8. S. D. Jacobs, S. R. Arrasmith, I. A. Kozhinova, L. L. Gregg, A. B. Shorey, H. J. Romanofsky, D. Golini, W. I. Kordonski, P. Dumas, and S. Hogan, *Am. Ceram. Soc. Bull.* **78**, 42 (1999).
9. B. Hallock *et al.*, in *Frontiers in Optics 2008/Laser Science XXIV/ Plasmonics and Metamaterials/Optical Fabrication and Testing*, OSA Technical Digest (CD) (Optical Society of America, Washington, DC, 2008), Paper OThB2.
10. J. S. Goela and R. L. Taylor, *J. Mater. Sci.* **23**, 4331 (1988).
11. R. Shen, H. Yang, S. N. Shafrir, C. Miao, M. Wang, J. Mici, J. C. Lambropoulos, and S. D. Jacobs, U.S. Patent No. US 8,808,568 B2 (19 August 2014).
12. S. N. Shafrir, H. J. Romanofsky, M. Skarlinski, M. Wang, C. Miao, S. Salzman, T. Chartier, J. Mici, J. C. Lambropoulos, R. Shen, H. Yang, and S. D. Jacobs, *Appl. Opt.* **48**, 6797 (2009).
13. S. Salzman, H. J. Romanofsky, Y. I. Clara, L. J. Giannechini, G. West, J. C. Lambropoulos, and S. D. Jacobs, in *Optifab 2013*, edited by J. L. Bentley and M. Pfaff (SPIE, Bellingham, WA, 2013), Vol. 8884, Paper 888407.
14. Q22, QED Technologies, LLC, Rochester, NY 14607.
15. Brookfield DV-III Cone and Plate Viscometer, Brookfield Engineering Laboratories, Inc., Stoughton, MA 02072.
16. Zygo NewView™ 100 White Light Optical Profiler, areal over 0.25 mm × 0.35 mm with a 20× Mirau objective, no filter, Zygo Corporation, Middlefield, CT 06455.
17. R. Shen, S. N. Shafrir, C. Miao, M. Wang, J. C. Lambropoulos, S. D. Jacobs, and H. Yang, *J. Colloid Interface Sci.* **342**, 49 (2010).
18. J. McCloy, E. Fest, R. Korenstein, and W. H. Poisl, in *Window and Dome Technologies and Materials XII*, edited by R. W. Tustison (SPIE, Bellingham, WA, 2011), Vol. 8016, Paper 80160I.



---

## Publications and Conference Presentations

---

### Publications

---

- R. Arpaia, M. Ejrnaes, L. Parlato, F. Tafuri, R. Cristiano, D. Golubev, R. Sobolewski, T. Bauch, F. Lombardi, and G. P. Pepe, “High-Temperature Superconducting Nanowires for Photon Detection,” *Physica C* **509**, 16 (2015).
- R. L. Berger, L. J. Suter, L. Divol, R. A. London, T. Chapman, D. H. Froula, N. B. Meezan, P. Neumayer, and S. H. Glenzer, “Beyond the Gain Exponent: Effect of Damping, Scale Length, and Speckle Length on Stimulated Scatter,” *Phys. Rev. E* **91**, 031103(R) (2015).
- A. Casner, L. Masse, B. Delorme, D. Martinez, G. Huser, D. Galmiche, S. Liberatore, I. Igumenshchev, M. Olazabal-Loumé, Ph. Nicolai, J. Breil, D. T. Michel, D. Froula, W. Seka, G. Riazuelo, S. Fujioka, A. Sunahara, M. Grech, C. Chicanne, M. Theobald, N. Borisenko, A. Orekhov, V. T. Tikhonchuk, B. Remington, V. N. Goncharov, and V. A. Smalyuk, “Progress in Indirect and Direct-Drive Planar Experiments on Hydrodynamic Instabilities at the Ablation Front,” *Phys. Plasmas*, **21**, 122702 (2014).
- R. Epstein, V. N. Goncharov, F. J. Marshall, R. Betti, R. Nora, A. R. Christopherson, I. E. Golovkin, and J. J. MacFarlane, “X-Ray Continuum as a Measure of Pressure and Fuel–Shell Mix in Compressed Isobaric Hydrogen Implosion Cores,” *Phys. Plasmas* **22**, 022707 (2015).
- G. Fiksel, A. Agliata, D. Barnak, G. Brent, P.-Y. Chang, L. Folsbee, G. Gates, D. Hasset, D. Lonobile, J. Magoon, D. Mastrosimone, M. J. Shoup III, and R. Betti, “Note: Experimental Platform for Magnetized High-Energy-Density Plasma Studies at the Omega Laser Facility,” *Rev. Sci. Instrum.* **86**, 016105 (2015).
- R. K. Follett, D. H. Edgell, R. J. Henchen, S. X. Hu, J. Katz, D. T. Michel, J. F. Myatt, J. Shaw, and D. H. Froula, “Direct Observation of the Two-Plasmon-Decay Common Plasma Wave Using Ultraviolet Thomson Scattering,” *Phys. Rev. E* **91**, 031104(R) (2015).
- C. M. Huntington, F. Fiuza, J. S. Ross, A. B. Zylstra, R. P. Drake, D. H. Froula, G. Gregori, N. L. Kugland, C. C. Kuranz, M. C. Levy, C. K. Li, J. Meinecke, T. Morita, R. Petrasso, C. Plechaty, B. A. Remington, D. D. Ryutov, Y. Sakawa, A. Spitkovsky, H. Takabe, and H.-S. Park, “Observation of Magnetic Field Generation via the Weibel Instability in Interpenetrating Plasma Flows,” *Nat. Phys* **11**, 173 (2015).
- M. Lafon, R. Betti, K. S. Anderson, T. J. B. Collins, R. Epstein, P. W. McKenty, J. F. Myatt, A. Shvydky, and S. Skupsky, “Direct-Drive–Ignition Designs with Mid-Z Ablators,” *Phys. Plasmas* **22**, 032703 (2015).
- K. Mehrotra, J. B. Oliver, and J. C. Lambropoulos, “Nano-Indentation of Single-Layer Optical Oxide Thin Films Grown by Electron-Beam Deposition,” *Appl. Opt.* **54**, 2435 (2015).
- D. T. Michel, A. K. Davis, V. N. Goncharov, T. C. Sangster, S. X. Hu, I. V. Igumenshchev, D. D. Meyerhofer, W. Seka, and D. H. Froula, “Measurements of the Conduction-Zone Length and Mass Ablation Rate in Cryogenic Direct-Drive Implosions on OMEGA,” *Phys. Rev. Lett.* **114**, 155002 (2015).
- D. S. Montgomery, B. J. Albright, D. H. Barnak, P. Y. Chang, J. R. Davies, G. Fiksel, D. H. Froula, J. L. Kline, M. J. MacDonald, A. B. Sefkow, L. Yin, and R. Betti, “Use of External Magnetic Fields in Hohlraum Plasmas to Improve Laser-Coupling,” *Phys. Plasmas* **22**, 010703 (2015).
- R. Nora, W. Theobald, R. Betti, F. J. Marshall, D. T. Michel, W. Seka, B. Yaakobi, M. Lafon, C. Stoeckl, J. Delettrez, A. A. Solodov, A. Casner, C. Reverdin, X. Ribeyre, A. Vallet, J. Peebles, F. N. Beg, and M. S. Wei, “Gigabar Spherical Shock Generation on the OMEGA Laser,” *Phys. Rev. Lett.* **114**, 045001 (2015).
- H. G. Rinderknecht, M. J. Rosenberg, C. K. Li, N. M. Hoffman, G. Kagan, A. B. Zylstra, H. Sio, J. A. Frenje, M. Gatu Johnson,

F. H. Séguin, R. D. Petrasso, P. Amendt, C. Bellei, S. Wilks, J. Delettrez, V. Yu. Glebov, C. Stoeckl, T. C. Sangster, D. D. Meyerhofer, and A. Nikroo, “Ion Thermal Decoupling and Species Separation in Shock-Driven Implosions,” *Phys. Rev. Lett.* **114**, 025001 (2015).

M. J. Rosenberg, C. K. Li, W. Fox, I. Igumenshchev, F. H. Séguin, R. P. J. Town, J. A. Frenje, C. Stoeckl, V. Glebov, and R. D. Petrasso, “A Laboratory Study of Asymmetric Magnetic Reconnection in Strongly Driven Plasmas,” *Nat. Commun.* **6**, 6190 (2015).

F. Weilacher, P. B. Radha, T. J. B. Collins, and J. A. Marozas, “The Effect of Laser Spot Shapes on Polar-Direct-Drive Implosions on the National Ignition Facility,” *Phys. Plasmas* **22**, 032701 (2015).

A. B. Zylstra, J. A. Frenje, F. H. Séguin, D. G. Hicks, E. L. Dewald, H. F. Robey, J. R. Rygg, N. B. Meezan, M. J. Rosenberg, H. G. Rinderknecht, S. Friedrich, R. Bionta, R. Olson, J. Atherton, M. Barrios, P. Bell, R. Benedetti, L. Berzak Hopkins, R. Betti, D. Bradley, D. Callahan, D. Casey, G. Collins, S. Dixit, T. Döppner, D. Edgell, M. J. Edwards, M. Gatun Johnson, S. Glenn, S. Glenzer, G. Grim, S. Hatchett, O. Jones, S. Khan, J. Kilkenny, J. Kline, J. Knauer, A. Kritcher, G. Kyrala, O. Landen, S. LePape, C. K. Li, J. Lindl, T. Ma, A. Mackinnon, A. Macphee, M. J.-E. Manuel, D. Meyerhofer, J. Moody, E. Moses, S. R. Nagel, A. Nikroo, A. Pak, T. Parham, R. D. Petrasso, R. Prasad, J. Ralph, M. Rosen, J. S. Ross, T. C. Sangster, S. Sepke, N. Sinenian, H. W. Sio, B. Spears, P. Springer, R. Tommasini, R. Town, S. Weber, D. Wilson, and R. Zacharias, “The Effect of Shock Dynamics on Compressibility of Ignition-Scale National Ignition Facility Implosions,” *Phys. Plasmas* **21**, 112701 (2014).

### Forthcoming Publications

R. Epstein, S. P. Regan, B. A. Hammel, L. J. Suter, H. A. Scott, M. A. Barrios, D. K. Bradley, D. A. Callahan, C. Cerjan, G. W. Collins, S. N. Dixit, T. Döppner, M. J. Edwards, D. R. Farley, K. B. Fournier, S. Glenn, S. H. Glenzer, I. E. Golovkin, A. Hamza, D. G. Hicks, N. Izumi, O. S. Jones, M. H. Key, J. D. Kilkenny, J. L. Kline, G. A. Kyrala, O. L. Landen, T. Ma, J. J. MacFarlane, A. J. Mackinnon, R. C. Mancini, R. L. McCrory, D. D. Meyerhofer, N. B. Meezan, A. Nikroo, H.-S. Park, P. K. Patel, J. E. Ralph, B. A. Remington, T. C. Sangster, V. A. Smalyuk, P. T. Springer, R. P. J. Town, and J. L. Tucker, “Applications and Results of X-Ray Spectroscopy in Implosion Experiments at the National Ignition Facility,” to be published in *Proceedings of Atomic Processes in Plasmas* (invited).

H. Habara, S. Ivancic, T. Iwawaki, Y. Uematsu, K. A. Tanaka, K. S. Anderson, D. Haberberger, C. Stoeckl, and W. Theobald, “Efficient Propagation of an Ultra-Intense Laser Beam in Dense Plasma,” to be published in *Plasma Physics and Controlled Fusion*.

M. Hohenberger, P. B. Radha, J. F. Myatt, S. LePape, J. A. Marozas, F. J. Marshall, D. T. Michel, S. P. Regan, W. Seka, A. Shvydky, T. C. Sangster, J. W. Bates, R. Betti, T. R. Boehly, M. J. Bonino, D. T. Casey, T. J. B. Collins, R. S. Craxton, J. A. Delettrez, D. H. Edgell, R. Epstein, G. Fiksel,

P. Fitzsimmons, J. A. Frenje, D. H. Froula, V. N. Goncharov, D. R. Harding, D. H. Kalantar, M. Karasik, T. J. Kessler, J. D. Kilkenny, J. P. Knauer, C. Kurz, M. Lafon, K. N. LaFortune, B. J. MacGowan, A. J. Mackinnon, A. G. MacPhee, R. L. McCrory, P. W. McKenty, J. F. Meeker, D. D. Meyerhofer, S. R. Nagel, A. Nikroo, S. Obenschain, R. D. Petrasso, J. E. Ralph, H. G. Rinderknecht, M. J. Rosenberg, A. J. Schmitt, R. J. Wallace, J. Weaver, C. Widmayer, S. Skupsky, A. A. Solodov, C. Stoeckl, B. Yaakobi, and J. D. Zuegel, “Polar-Direct-Drive Experiments at the National Ignition Facility,” to be published in *Physics of Plasmas* (invited).

S. X. Hu, V. N. Goncharov, T. R. Boehly, R. L. McCrory, S. Skupsky, L. A. Collins, J. D. Kress, and B. Militzer, “Impact of First-Principles Properties of Deuterium–Tritium on Inertial Confinement Fusion Target Designs,” to be published in *Physics of Plasmas* (invited).

S. Ivancic, D. Haberberger, H. Habara, T. Iwawaki, K. S. Anderson, R. S. Craxton, D. H. Froula, D. D. Meyerhofer, C. Stoeckl, K. Tanaka, and W. Theobald, “Channeling Multikilojoule High-Intensity Laser Beams in an Inhomogeneous Plasma,” to be published in *Physical Review E*.

D. T. Michel, A. K. Davis, W. J. Armstrong, R. E. Bahr, R. Epstein, V. N. Goncharov, M. Hohenberger, I. V. Igumenshchev, R. K.

Jungquist, D. D. Meyerhofer, P. B. Radha, T. C. Sangster, C. Sorce, and D. H. Froula, “Measurements of the Ablation-Front Trajectory and Low-Mode Nonuniformity in Direct-Drive Implosions Using X-Ray Self-Emission Shadowgraphy,” to be published in *High-Power Laser Science and Engineering*.

P. M. Nilson, L. Gao, I. V. Igumenshev, G. Fiksel, R. Yan, J. R. Davies, D. Martinez, V. A. Smalyuk, M. G. Haines, E. G. Blackman, D. H. Froula, R. Betti, and D. D. Meyerhofer, “Magnetic-Field Generation by the Ablative Nonlinear Rayleigh–Taylor Instability,” to be published in the *Journal of Plasma Physics*.

P. B. Radha, V. N. Goncharov, M. Hohenberger, T. C. Sangster, R. Betti, R. S. Craxton, D. H. Edgell, R. Epstein, D. H. Froula,

J. A. Marozas, F. J. Marshall, R. L. McCrory, P. W. McKenty, D. D. Meyerhofer, D. T. Michel, S. X. Hu, W. Seka, A. Shvydky, S. Skupsky, J. A. Frenje, M. Gatu-Johnson, R. D. Petrasso, T. Ma, S. Le Pape, and A. J. Mackinnon, “Direct-Drive-Implosion Physics: Results from OMEGA and the National Ignition Facility,” to be published in the *Journal of Physics: Conference Series*.

W. Theobald, R. Nora, W. Seka, M. Lafon, K. S. Anderson, M. Hohenberger, F. J. Marshall, D. T. Michel, A. A. Solodov, C. Stoeckl, D. Edgell, B. Yaakobi, A. Casner, C. Reverdin, X. Ribeyre, O. Shvydky, A. Vallet, J. Peebles, F. N. Beg, M. S. Wei, and R. Betti, “Spherical Strong-Shock Generation for Shock-Ignition Inertial Fusion,” to be published in *Physics of Plasmas* (invited).

### Conference Presentations

T. Z. Kosc, J. H. Kelly, E. M. Hill, C. Dorrer, W. Donaldson, and L. J. Waxer, “The Multiple-Pulse Driver Line on the OMEGA Laser,” *Photonics West-LASE*, San Francisco, CA, 7–12 February 2015.

ments on OMEGA and the NIF,” NIF and Jupiter Laser Facility User Group Meeting, Livermore, CA, 8–11 February 2015.

A. K. Davis, D. T. Michel, I. V. Igumenshev, R. S. Craxton, R. Epstein, V. N. Goncharov, M. Hohenberger, S. X. Hu, M. Lafon, D. D. Meyerhofer, P. B. Radha, T. C. Sangster, and D. H. Froula, “Polar Direct-Drive Mass-Ablation-Rate Measure-

ments on OMEGA and the NIF,” NIF and Jupiter Laser Facility User Group Meeting, Livermore, CA, 8–11 February 2015.

Y. Akbas, L. Q. Zhang, Y. Alimi, A. M. Song, I. Iñiguez-de-la-Torre, J. Mateos, T. González, G. Wicks, and R. Sobolewski, “Optically-Active Semiconducting Asymmetric Nano-Channel Diodes,” 5th OASIS Int’l Conf. & Exhibition on Optics and Electro-Optics, Tel Aviv, Israel, 3–4 March 2015.





